

Magnetic shielding using electrical steel panels at extremely low frequencies

by

Xiaojun Di

**A thesis submitted to the Cardiff University in
candidature for the degree of Doctor of Philosophy**

**Wolfson Centre for Magnetism
School of Engineering
Cardiff University
Wales, United Kingdom**

January 2008

UMI Number: U585112

All rights reserved

INFORMATION TO ALL USERS

The quality of this reproduction is dependent upon the quality of the copy submitted.

In the unlikely event that the author did not send a complete manuscript and there are missing pages, these will be noted. Also, if material had to be removed, a note will indicate the deletion.



UMI U585112

Published by ProQuest LLC 2013. Copyright in the Dissertation held by the Author.
Microform Edition © ProQuest LLC.

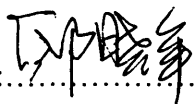
All rights reserved. This work is protected against
unauthorized copying under Title 17, United States Code.



ProQuest LLC
789 East Eisenhower Parkway
P.O. Box 1346
Ann Arbor, MI 48106-1346

Declaration

This work has not previously been accepted in substance for any degree and is not concurrently submitted in candidature for any other higher degree.

Signed: .....(Candidate) Date: 07-31-2008

Statement 1

This thesis is being submitted in partial fulfilment of the requirements for the degree of(insert as appropriate PhD, MPhil, EngD)

Signed: .....(Candidate) Date: 07-31-2008

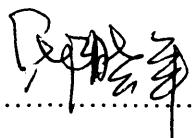
Statement 2

This thesis is the result of my own independent work/investigation, except where otherwise stated. Other sources are acknowledged by explicit references.

Signed: .....(Candidate) Date: 07-31-2008

Statement 3

I hereby give consent for my thesis, if accepted, to be available for photocopying, inter-library loan and for the title and summary to be made available to outside organisations.

Signed: .....(Candidate) Date: 07-31-2008

To my parents and Na

献给我的父亲，母亲和娜娜

ACKNOWLEDGEMENT

I would like to express my gratitude to all those who gave me the opportunity to complete this thesis.

I would like to thank my supervisors, Prof. Tony Moses and Dr. Phil Anderson whose mentoring and encouragement helped me during the three-year's research. The last part of the thesis was completed after I left Cardiff, Most discussions were done over the phone and by emails. They have made every effort to put me on a convenient position.

I am grateful to Dr. Hugh Stanbury, the former director of research at Cogent Power. His assistance on the sample preparations and discussions of the test results has been a great help for me. I also want to thank Prof. Phil Beckley, who offered me not only his technical expertise but also the stimulating suggestions.

I am deeply indebted to my parents, who bore me, raised me, taught me, supported me and loved me.

I owe a very special thanks to my wife, Na, who has given up a lot to support me.

List of Contents

Declarations and statements	0-1
Acknowledgement.....	0-2
Summary.....	0-3
List of contents	0-4
1 INTRODUCTION	1-1
REFERENCES OF CHAPTER 1.	1-4
2 BASIC MAGNETISM RELATED TO MAGNETIC SHIELDING	2-1
2.1 BASIC TERMS.....	2-1
2.2 INDUCED ELECTROMOTIVE FORCE	2-2
2.3 MAGNETIC PARAMETERS OF FERROMAGNETIC MATERIALS.....	2-3
2.4 HYSTERESIS.....	2-5
2.5 DEMAGNETIZATION OF MAGNETIC MATERIALS	2-8
2.6 DEMAGNETIZATING EFFECT	2-9
REFERENCES OF CHAPTER 2.	2-11
3 MAGNETIC SHIELDING THEORY AND MATERIALS	3-1
3.1 INTRODUCTION.....	3-1
3.2 MAGNETIC SHIELDING THEORY	3-1
3.2.1 Magnetic shielding principles at low frequencies.....	3-1
3.2.2 Definition and calculation of the shielding factor.....	3-2
3.2.3 Double-layer shielding	3-10
3.2.4 Eddy current cancellation and skin depth	3-13
3.3 MAGNETIC SHIELDING MATERIALS	3-18
3.3.1 Traditional magnetic shielding material	3-19
3.3.2 Electrical steel for large scale shielding.....	3-20
3.3.3 Characterization of electrical steels	3-23
3.4 SUMMARY	3-27
REFERENCES OF CHAPTER 3	3-28

List of Contents

4	LITERATURE REVIEW	4-1
4.1	THEORETICAL STUDY OF THE SHIELDING EFFECTIVENESS.....	4-1
4.2	MEASURING THE SHIELDING EFFICIENCY	4-17
	REFERENCES OF CHAPTER 4	4-31
5	SYSTEM DEVELOPMENT	5-1
5.1	INTRODUCTION	5-1
5.2	OUTLINE OF THE TEST SETUP AND SHIELDING FACTOR DEFINITION.....	5-2
5.3	SAMPLES.....	5-5
5.4	MAGNETIC FIELD GENERATION.	5-6
5.5	ELECTRICAL STEEL CYLINDER IN THE TEST SETUP	5-10
5.6	MEASURING THE MAGNETIC FIELD	5-15
5.7	SAMPLE DEMAGNETIZATION AND TEST REPEATABILITY.....	5-17
5.8	DC MAGNETIC SHIELDING FACTOR MEASUREMENT	5-20
5.9	MEASUREMENT OF IN-PLANE MAGNETIZATION AT AC FIELD CONDITION.....	5-21
	REFERENCES OF CHAPTER 5	5-22
6	RESULTS AND DISCUSSION.....	6-1
6.1	PANEL THICKNESS.....	6-1
6.2	POWER LOSS GRADE AND THE SHIELDING FACTOR	6-2
6.3	FREQUENCY DEPENDENT SHIELDING FACTORS.....	6-17
6.4	FLUX LEAKAGE OUT OF THE SAMPLE SURFACE AND IN-PLANE MAGNETIZATION	6-26
6.5	DOUBLE-LAYER SHIELDS.....	6-38
6.6	DEGRADATION OF SHIELDING FACTOR BY DRILLED HOLES ON THE STEEL PANEL	6-48
6.7	JOINT BETWEEN THE STEEL PANELS AND THE AIR GAPS BETWEEN LAYERS	6-53
6.8	DISCUSSION OF THE FINITE ELEMENT MODELING	6-55
	REFERENCES OF CHAPTER 6	6-58
7	CONCLUSIONS AND FUTURE WORK	7-1
7.1	CONCLUSIONS	7-1

List of Contents

7.2 RECOMMENDATIONS FOR FUTURE WORK	7-3
REFERENCES OF CHAPTER 7	7-5
LIST OF PUBLICATIONS	8-1

Summary

A new test method and finite element modelling were used to investigate how material properties of electrical steel panels affect their shielding factors. Both experiment and modelling showed an improved DC shielding factor with increasing thickness for the shields of similar magnetic properties. Enhanced shielding by the eddy currents was demonstrated by testing the same steel panel under AC and DC field conditions. Comparing to non-oriented steel panels, a decreasing shielding factor with the frequency from 50 Hz to 400 Hz was found for grain-oriented steels. This was also investigated by measuring magnetizations along rolling and transverse directions within the panels.

It was found that measured shielding factors of double-layer shields with two grain-oriented steel panels could be improved significantly with orthogonally arranged rolling directions. Different shielding factors were found by placing different panel closer to the field source in the test of double-layer shields formed by one grain-oriented and one non-oriented steel panels. Although little shielding effect of aluminium panels are found at 50 Hz, adding the same aluminium panel with single electrical steel shield was dramatically improved the shielding.

The magnetization of shielding sample at AC conditions has been modelled and measured. The magnetization was found very low due to the demagnetizing effect. Therefore, the permeability at very low magnetization range has a large effect on the magnetic shielding factors of the steel panels.

Drilled hole as a defect in the panel and overlap of the panels have been tested with the new test method. Small hole in the panel would not cause the degradation of the overall shielding factor of the shield rooms. Overlap was proved to be an effective way to reduce the flux leakage at the joints between the panels

The difference between the computed and measured shielding factors is addressed by analysing the capability of the solver used in the finite element modelling and the uncertainty of the measured B-H characteristic of the material as the input to the model.

Chapter One

Introduction

Static and power frequency magnetic fields have become of concern due to their disturbances to electronic devices[1]. Apart from instrumental aspects, intensive research is being carried out on biological effects of these fields[2]. Although there has been no proof of the harmful effects to date, the International Commission for Non-Ionizing Radiation Protection (ICNIRP) published guidelines to limit the exposure of people to the magnetic fields at static and extremely low frequencies[3, 4] due to the uncertainty of the current research.

Within this background and along with the development of high power Magnetic Resonance Imaging devices (MRIs), many large-scale magnetically shielded rooms are required to protect staff that operate the machines and maintain the accuracy of the scans. Mumetal, a conventional magnetic shielding material, provides a well-recognized high magnetic shielding efficiency at low frequencies, however the cost of material is high. Compared with Mumetal, electrical steels offer a cheaper and possibly effective alternative, especially when large volume of material is used.

Electrical steels are manufactured mainly for power applications and widely used in transformers and motors. Broad varieties of electrical steels are commercially available to provide a wide range of performance choices and a flexible expense plan for shielding projects. Although the magnetic properties of electrical steels have been studied for years and test methods are well documented[5, 6], there is no appropriate test method available to assess the shielding efficiency of electrical steel panels. The commercially available standard grading system only reflects the power loss and the reference to

these grades for shielding material selection can be flawed[7].

Little research and development work on magnetic shielding at DC and extremely low frequency has been carried out compared to those on electromagnetic shielding at high frequency. Electromagnetic shielding at frequencies higher than 150 kHz is an important factor in electronic products' Electromagnetic Compatibility (EMC). Assessment of the material's high frequency shielding efficiency can be carried out under near field or far field conditions using well established methods [8, 9]. At low frequency, the widely used method of measuring the magnetic shielding efficiency is that of the American Society of Testing Materials (ASTM) [10]. The shielding efficiency is measured by testing a cylindrical sample in a uniform magnetic field generated by a pair of large Helmholtz coils. However, this test setup can not represent the efficiency of electrical steels which are cut into panels of various sizes and installed on the walls, floor and ceiling of shielding rooms.

A new test method is proposed and developed in this research work to characterize the magnetic shielding properties of electrical steel panels. Finite element modelling was used to design, optimize the test setup and help study the magnetic shielding theory.

In summary, the objectives of this research are as follows:

- To design, develop and construct a test system, capable of assessing magnetic shielding factor of electrical steel panels for magnetic fields at DC and extremely low frequencies
- To carry out shielding factor measurements at DC and extremely low frequencies to investigate the contribution of eddy currents to the magnetic shielding factor

- To carry out measurements on single-layer shields of electrical steel panels of various grades, then study how basic magnetic properties affect the shielding factors.
- To carry out the assessment of double-layer shields of grain-oriented steel panels, grain-oriented and non-oriented steel panels, non-oriented steel and aluminium panels.
- To assess the effect of non-uniformity of the shielding panel, such as caused by a drilled hole, different practice of joining panels to produce guidelines for practical work.
- To study the magnetization of the shielding samples using measurements with the in-plane sensing coils and finite element modelling.
- To compare some of the results obtained using this new test method with previous data of samples in similar size by others, such as Okazaki. et. al..

References:

1. Dovan, T.; Owen, R., "*Power frequency magnetic fields and computer VDU interference phenomena*," in International Conference on Bio-electromagnetism. 1998.
2. Ahlbom, A.; Cardis, E.; Grenn, A.; Linet, M.; Savitz, D.; Swerdlow, A., "*Review of the Epidemiologic Literature on EMF and Health*," Environmental Health Perspectives," Volume: 109, Issue: 6, pp. 911-933, 2001.
3. ICNIRP, "*Guidelines for limiting exposure to time-varying electric, magnetic, and electromagnetic fields (Up to 300 GHz)*," International Commission for Non-Ionizing Radiation Protection, 1997.
4. ICNIRP, "*Guidelines on limits of exposure to static magnetic field*," International Commission for Non-Ionizing Radiation Protection, 1993.
5. British Standard, "*BS EN-60404-2: 1998 - Methods of measurement of the magnetic properties of electrical steel sheet and strip by means of an Epstein frame*," British Standard Institute, 1998.
6. British Standard, "*BS EN 10280: 2001- Methods of measurement of the magnetic properties of electrical sheet and strip by means of a single sheet tester*," British Standard Institute, 2001.
7. Di, X.; Moses, A. J.; Anderson, P., "*Assessment of low frequency shielding performance of electrical steel sheets*" in Magnetic Measurement Conference, 2006.
8. Wilson, P.F., "*Techniques for measuring the electromagnetic shielding effectiveness of materials. I. Far-field source simulation*," IEEE Transactions on Electromagnetic Compatibility, Volume: 30, Issue: 3, pp. 242-251, 1988.
9. Wilson, P.F., "*Techniques for measuring the electromagnetic shielding effectiveness of materials. II. Near-field source simulation*," IEEE Transactions on Electromagnetic Compatibility, Volume: 30, Issue: 3, pp. 251-259, 1988.
10. ASTM, *ASTM A698/A698M 02 - "Standard Test Method for Magnetic Shield Efficiency in Attenuating Alternating Magnetic Fields*," American Society of Testing Materials, 2002

Chapter Two

Basic Magnetism Related to Magnetic Shielding

2.1 Basic terms

A magnetic field is caused by a electric current, which can be a result of the movement of electrically charged objects, such as the electric current in a conductor, or the orbits of electron around the atomic nucleus and the spin itself [1]. The response of a medium to the magnetic field is called magnetic flux density or magnetic induction. In the case of free space, the relationship between the flux density, B and the magnetic field strength, H can be expressed as

$$B = \mu_0 \cdot H \quad (2.1)$$

Where B is flux density in Tesla [T], H is magnetic field strength in Ampere per meter [A/m] and μ_0 is the magnetic permeability, also magnetic constant of free space in Henry per meter [H/m]

In magnetic materials without hysteresis, the relation between B and H can be written as

$$B = \mu_r \cdot \mu_0 \cdot H \quad (2.2)$$

Where μ_r is defined as the relative magnetic permeability. Relative permeability μ_r is more often used than material magnetic permeability μ , which is expressed as

$$\mu = \mu_r \cdot \mu_0 \quad (2.3)$$

Chapter 2. Basic Magnetism Related to Magnetic Shielding

Materials can be classified into different categories according to their relative permeability. In general, materials with μ_r slightly greater than unity are paramagnets and the ones with a μ_r slightly less than unity are diamagnets. Ferromagnetic materials form another group of materials whose μ_r is usually much greater than unity and a function of many factors. Table 2.1 presents μ_r of some common paramagnetic, diamagnetic and ferromagnetic materials.

Material	μ_r
Free space	1.000 000 00
Air	1.000 000 37
Al	1.000 02
Cu	0.999 99
96% Fe, 4% Si (non-oriented)	7000*
97% Fe, 3% Si (grain-oriented)	100 000*
50% Co, 50% Fe (Permendur)	5000*
79% Ni, 16 Fe, 5% Mo (Super Malloy)	1 000 000*
97% Fe, 3% Si (monocrystal)	3 800 000*

Table 2.1. The relative permeability μ_r of some paramagnetic, diamagnetic materials and the maximum* relative permeability μ_r of ferromagnetic materials[2].

The B-H curve shows how a material responds to an applied magnetic field [3]. Paramagnetic and diamagnetic materials have linear relationships between the flux density B and the applied field H.

2.2 Induced Electromotive Force (e.m.f)

Magnetic fields changing with time result in an additional force on electric charges, expressed as an electromotive force called the Faraday induced e.m.f.

Chapter 2. Basic Magnetism Related to Magnetic Shielding

Faraday developed a general description of the time-varying events, which produces an induced e.m.f, expressed by equation 2.4. He found that the e.m.f ε induced in any loop only depends on the time rate dt of change of the magnetic flux ϕ surrounded by the circuit.

$$\varepsilon = -\frac{d\phi}{dt} \quad (2.4)$$

The negative sign in Faraday's induction law is explained in Lenz's law as the induced electric current always flows in such a direction to oppose the change producing it.

2.3 Magnetic Parameters of Ferromagnetic Materials

An important magnetic property of ferromagnetic material is the magnetization, M . It describes the response of material to applied magnetic field and has the same units to magnetic field H . The flux density B can be written in terms of M as:

$$B = \mu_0 \cdot H + \mu_0 \cdot M \quad (2.5)$$

In free space, $M = 0$ then,

$$B = \mu_0 \cdot H \quad (2.6)$$

The term $\mu_0 \cdot M$ is called magnetic polarization, J , which is the contribution from material with the same units as the magnetic flux density B . For materials without hysteresis, the case in which material is magnetized is described by its magnetic susceptibility χ (H/m), defined in equation 2.7.

$$\chi = \frac{M}{H} \quad (2.7)$$

Chapter 2. Basic Magnetism Related to Magnetic Shielding

The parameters such as permeability and susceptibility of a material can be obtained from a graph of B against H . This B - H curve is called a magnetization curve. A typical magnetization curve for iron is shown in Fig.2.1. The specimen in this case is initially demagnetized. Four dashed lines corresponding to different values of constant relative permeability μ_r are also shown. It can be seen that relative permeability varies in magnitude according to the value of the magnetic field inside the specimen. Under very low magnetization, initial permeability μ_i represents magnetic property of the material.

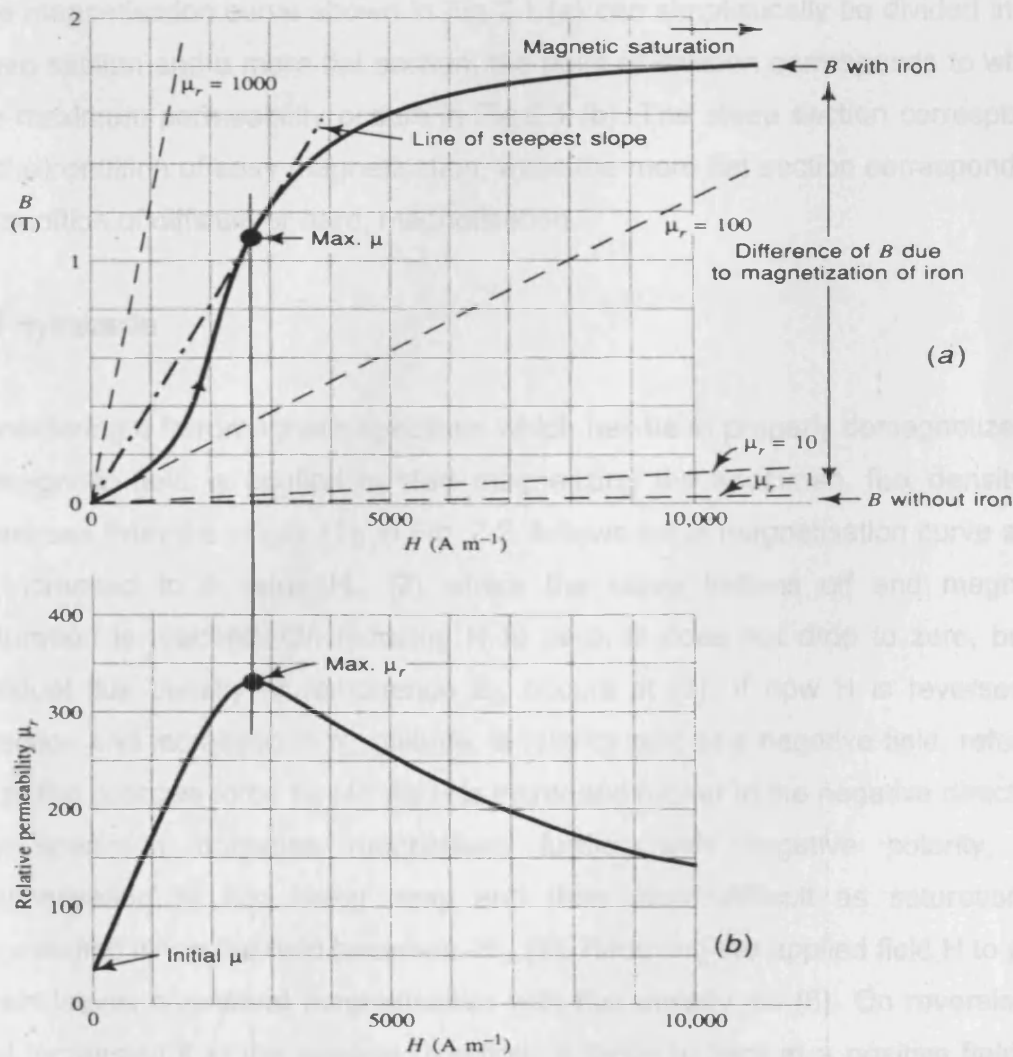


Fig. 2.1. Typical initial magnetization curve of iron and corresponding relationship between relative permeability μ_r and applied field H [4]

The B-H curve shown in Fig .2.1 (b) is a normal-magnetization curve because the material is completely demagnetized before external field H is applied. As H is increased, the value of B rises rapidly at first and then more slowly. At a sufficiently high value of H the curve tends to approach flat. This condition is called magnetic saturation. The magnetization curve starting at the origin has a finite slope defined as the initial permeability μ_i .

The magnetisation curve shown in Fig.2.1 (a) can simplistically be divided into a steep section and a more flat section, the point of division corresponds to where the maximum permeability occurs in Fig.2.1 (b). The steep section corresponds to the condition of easy magnetisation, while the more flat section corresponds to a condition of difficult, or hard, magnetisation.

2.4 Hysteresis

Considering a ferromagnetic specimen which has been properly demagnetized, if a magnetic field is applied to start magnetizing the specimen, flux density B increases from the origin, (1), in Fig. 2.2, follows initial magnetisation curve as H is increased to a value H_m (2) where the curve flattens off and magnetic saturation is reached. On reducing H to zero, B does not drop to zero, but a residual flux density or remanence B_r , occurs at (3). If now H is reversed in direction and increased in magnitude, B falls to zero at a negative field, referred to as the coercive force H_c (4). As H is increased further in the negative direction, the specimen becomes magnetised further with negative polarity, the magnetisation at first being easy and then more difficult as saturation is approached when the field becomes $-H_m$ (5). Reducing the applied field H to zero again leaves a residual magnetisation with flux density $-B_r$ (6). On reversing H and increasing it in the positive direction, B drops to zero at a positive field, or coercive force H_c (7). With a further increase in H the specimen reaches

Chapter 2. Basic Magnetism Related to Magnetic Shielding

saturation with the original polarity. When the field is equal to $+H_m$, the hysteresis loop is completed.

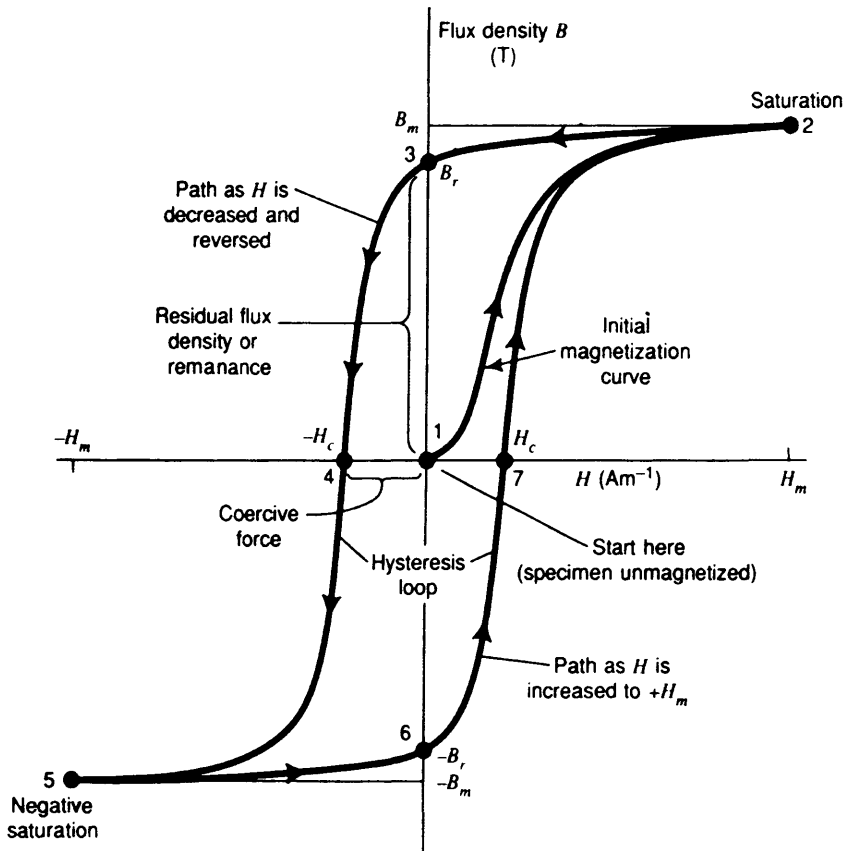


Fig. 2.2. Hysteresis loop showing path of B as H is varied.

The phenomenon, which causes material's magnetic inductance, B to fall behind the change of the external applied magnetic field, H , is called hysteresis, and the loop traced out by magnetization curve is hysteresis loop. If the ferromagnetic specimen is cycled to saturation at both extremes of magnetization curve, the loop is called the saturation, or major, hysteresis loop. The residual flux density B_r , on the saturation loop is called the remanence, and the coercive force H_c on this loop is the coercivity. Thus, the retentivity of a material is the maximum value, which the residual flux density can attain and the coercivity is the maximum value, which coercive force can attain[5].

As shown in Fig. 2.3, the hysteresis loop of soft or easily magnetized magnetic material is narrow and has a small-enclosed area, while the hysteresis loop of a hard magnetic material encloses a greater area[6].

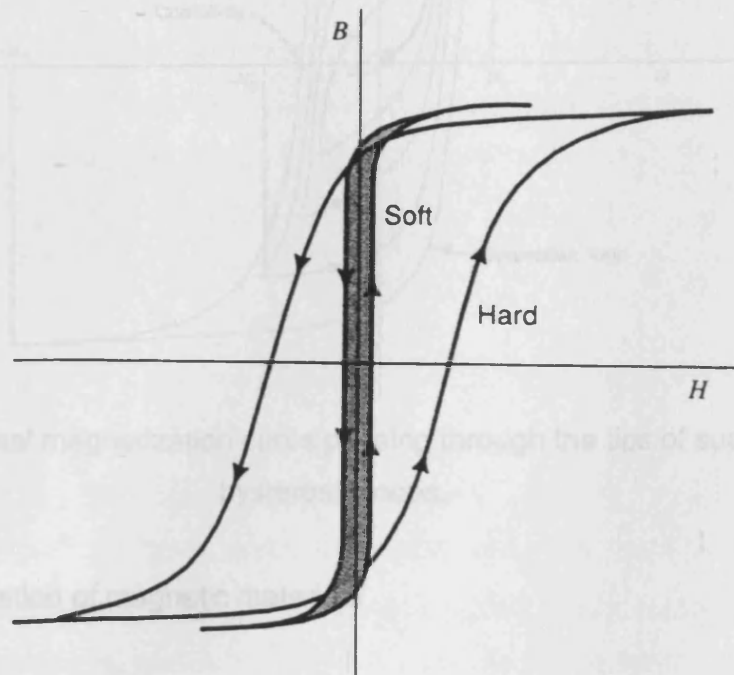


Fig.2.3. Hysteresis loops of soft and hard magnetic materials [6].

The curve passing through the tips of the hysteresis loop, shown in Fig. 2.4, is the normal magnetization curve under conditions of alternating field[7]. This curve is reproducible and the characteristic of a particular type of magnetic material. The normal magnetization curve can also be called as initial magnetization curve, which is defined from the unmagnetised condition[4].

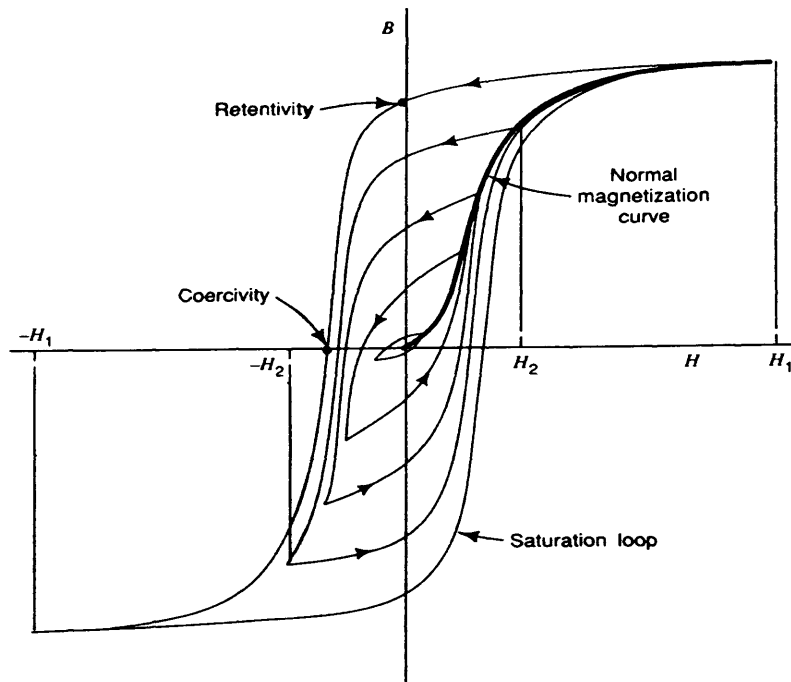


Fig.2.4. Normal magnetization curve passing through the tips of successive hysteresis loops.

2.5 Demagnetization of magnetic materials

In measuring the properties of magnetic materials, demagnetization of the sample is an essential procedure. There are several ways to attempt to achieve zero magnetization of the samples such as by heating the sample above the Curie temperature to break the alignment of magnetic moments within magnetic domains. In general magnetic measurement, the most widely used demagnetization process is by reversals of the applied magnetic field. In this process external magnetic field H is cycled over a sufficient range to saturate the specimen and then cycled over successively smaller ranges obtaining a series of hysteresis loops of decreasing size as in Fig. 2.5. The process is continued until the excursion of H approaches zero, leaving the specimen essentially demagnetized. The starting value of the applied field and frequency of the magnetization reversals of demagnetization process varies due to the individual magnetic properties of different magnetic materials.

2.6 Demagnetizing Effect

The magnetization M and magnetic field H usually act in the opposite directions inside a magnetized material of finite dimensions, due to the presence of magnetic dipole moments. This creates a demagnetizing field H_d , which is present whenever magnetic poles created in a material can be defined. This demagnetizing field caused by the magnetic poles created in the material depends on two factors, the magnetization in the material and the shape of the specimen[5]. The demagnetizing field is proportional to magnetization and can be calculated by:

$$H_d = -N_d M \quad (2.8)$$

Where N_d is a dimensionless demagnetizing factor calculated solely from the sample geometry.

Exact analytical solutions for N_d can only be obtained in the case of spheres and ellipsoids. Approximations and simplifications are often made, but in many cases can give good practical results. Table 2.2 lists the demagnetizing factors for various simple geometries [5].

Geometry	N_d
Closed Toroid	0
Infinitely Long cylinder	0
Cylinder $l/d = 20$	0.00617
Cylinder $l/d = 10$	0.0172
Cylinder $l/d = 8$	0.02
Cylinder $l/d = 5$	0.040
Cylinder $l/d = 1$	0.27
Sphere	0.333

Table 2.2. Demagnetizing factors for various simple geometries [5].

l : length of the cylinder, d : diameter of cylinder

Whenever the direction of induced magnetic dipoles (direction of magnetisation) in the specimen within an applied field has a component normal to the specimen surface, there are demagnetising effects at the surface, which reduce the magnetic contribution of the specimen. The field H_{in} inside the specimen should be corrected from the applied field H_{app} due to the demagnetizing field. This can be done as:

$$H_{in} = H_{app} - N_d M \quad (2.9)$$

Three commonly used specimens of magnetic materials are shown in Fig. 2.5. As demonstrated in Table 2.2, different demagnetizing factors are determined by the geometries. For the specimen shown in Fig. 2.5 (a), the demagnetising effect of the end surfaces perpendicular to the magnetisation is large. In a specimen where the area is smaller relative to the length, as shown in Fig. 2.5 (b), the effect is smaller. Finally, in a toroidal specimen, shown in Fig. 2.5 (c), in which a solenoid winding produces magnetisation everywhere parallel to the surface, there is no demagnetising effect. The demagnetising effect is an important phenomenon in this investigation and is discussed further in Chapter 6.

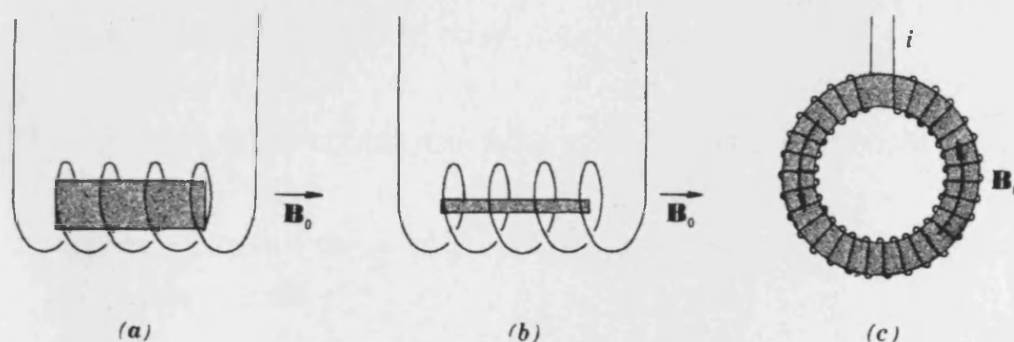


Fig. 2.5. Specimens with different end surface areas

References:

1. Chikazumi, S., *Physics of Ferromagnetism*, Oxford University Press, 1997.
2. Lan, Z., *Physics of Ferromagnetism (in Chinese)*, Chengdu, University of Electronic Technology Press, 1998.
3. Cullity, B. D., *Introduction to Magnetic Materials*, Addison Wesley Longman Publishing Co, 1972.
4. Kraus, J.D., *Electromagnetics*. 4th. ed., McGraw-Hill International, 1992.
5. Jiles, D., *Introduction to magnetism and magnetic Materials*. 2nd. ed. New York, Chapman&Hall, 1997.
6. Heck, C., *Magnetic materials and their application*, London, Academic Press Ltd, 1974.
7. Beckley, P., *Electrical Steels: A Handbook for Producers and Users*. Newport, European Electrical Steels, Orb Works, 2000.

Chapter Three

Magnetic shielding theory and Materials

3.1 Introduction

Magnetic shielding is a process of limiting magnetic flux between two locations. This can be done either by separating them with magnetic shielding materials or generating fields of the same value but at opposite polarization to cancel the incident fields in the shielded region. Active shielding by field cancellation involves magnetic field sensor measuring the field strength and feedback circuitry to control the cancellation field. Compared with active shielding, passive shielding using magnetic shielding materials is more convenient to use, especially for large-scale shields, such as magnetically shielded rooms and chambers.

This chapter firstly presents the basic theories of passive magnetic shielding and introduces magnetic shielding materials in general. Then some specific magnetic properties and characterization methods of electrical steels are covered.

3.2 Magnetic Shielding Theory

3.2.1 Magnetic shielding principles at low frequencies

Shielding materials can limit magnetic fields in the following mechanisms:

1. Magnetic flux can be diverted away from the shielded region by highly permeable materials.
2. If the incident field is time-varying, it can induce e.m.fs that generate eddy currents in the conducting materials. The induced eddy currents generate

fields in the opposite polarity of the incident fields to reduce the absolute field strength in the shielded region.

Which one of these plays the key role in any application is mainly dependent on the frequency of the incident field, which needs to be reduced or eliminated by shielding. In the case of static and power frequency magnetic shielding, flux ducting is dominant[1].

3.2.2 Definition and calculation of the shielding factor

To describe the magnetic shielding capability of the material, its shielding efficiency or shielding factor can be defined as:

$$SF = \frac{H_o}{H_s} \quad (3.1)$$

Where SF is the shielding factor, H_o is the magnetic field strength at a point when the shield is not in place, H_s is the magnetic field strength at the same location when the shield is in place[2].

Shielding factors of magnetic shields with simple geometries can be calculated by either solving Maxwell's equations or modeling with the finite element method. Fig. 3.1 shows a single-shell spherical shield for a uniform static magnetic field H_a . The inner and outer radii of the shield are a and b respectively (thickness $t = b - a$). Assume the magnetic permeability μ of the shielding material is constant and independent of the applied magnetic field. The shielding factor of this sphere can be calculated as:

$$SF = \frac{H_a}{H_s} \quad (3.2)$$

Chapter 3. Magnetic Shielding Theory and Materials

Where H_a is the applied field and H_s is the field strength at the centre of the shielded region.

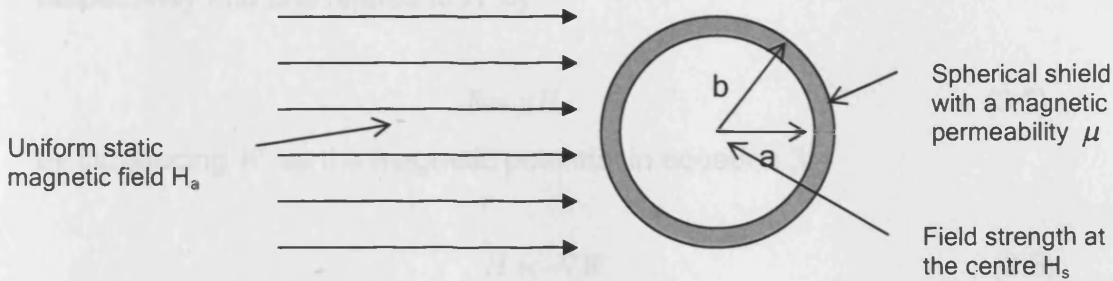


Fig. 3.1 Spherical shield in a uniform static magnetic field

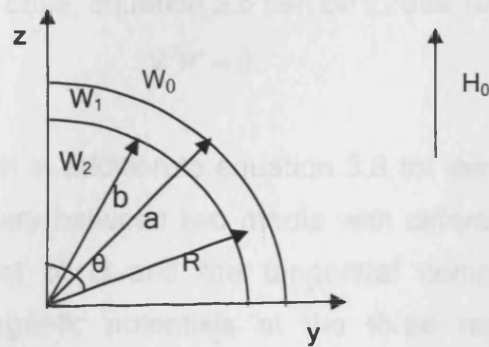


Fig. 3.2. One quarter cross section of a spherical shield, where W_0 , W_1 and W_2 are the magnetic potentials for the regions outside the sphere, the shielding material and the shielded area, H_0 is the external field strength, R_1 and R_2 are the radius to external and internal surface respectively, R and θ are the variables in the spherical system

Applying spherical coordinates to the problem as in shown in Fig. 3.2, according to the fundamental equations of electromagnetism [3], the static magnetic field H and magnetic flux density B satisfies

$$\nabla \times H = 0 \quad (3.3)$$

and

$$\nabla \cdot \mathbf{B} = 0 \quad (3.4)$$

respectively and \mathbf{B} is related to \mathbf{H} by

$$\mathbf{B} = \mu \mathbf{H} \quad (3.5)$$

by introducing W as the magnetic potential in equation 3.4

$$\mathbf{H} = -\nabla W \quad (3.6)$$

and equation 3.4 becomes

$$\nabla \cdot (\mu \nabla W) = 0 \quad (3.7)$$

As μ is constant in this case, equation 3.6 can be further reduced to

$$\nabla^2 W = 0 \quad (3.8)$$

The boundary condition in addition to equation 3.8 for the case as shown in Fig. 3.1 is that at a boundary between two media with different permeabilities, both the normal component of \mathbf{B} and the tangential component of \mathbf{H} must be continuous. The magnetic potentials at the three regions in Fig. 3.2 are respectively given as:

$$\begin{aligned} W_0 &= (-H_0 R + \frac{B_0}{R^2}) \cos \theta & R > a \\ W_1 &= (-H_1 R + \frac{B_1}{R^2}) \cos \theta & a > R > b \\ W_2 &= -H_2 R \cos \theta & b > R \end{aligned} \quad (3.9)$$

where B_0 is the magnetic induction outside the shield, H_1 and H_2 are the magnetic field strengths in the shield and the shielded area, B_1 and B_2 are the magnetic inductions in the shield and the shielded area.

Chapter 3. Magnetic Shielding Theory and Materials

The relative magnetic permeability is unity for the space apart from the spherical magnetic shield. By maintaining the continuity of normal B and tangential H, the boundary conditions at the material interface between the free space and the shield are

$$\begin{aligned} W_0 = W_1, \quad \frac{\delta W_0}{\delta R} &= \mu \frac{\delta W_1}{\delta R} & R = b \\ W_1 = W_2, \quad \frac{\delta W_1}{\delta R} &= \mu \frac{\delta W_2}{\delta R} & R = a \end{aligned} \quad (3.10)$$

From equations 3.9 and 3.10 together

$$\begin{aligned} -H_0 b + \frac{B_0}{b^2} &= -H_1 b + \frac{B_1}{b^2} \\ -H_0 - \frac{2B_0}{b^3} &= \mu \left(-H_1 - \frac{2B_1}{b^3} \right) \end{aligned} \quad (3.11)$$

and

$$\begin{aligned} -H_1 a + \frac{B_1}{a^2} &= -H_2 a \\ \mu \left(-H_1 - \frac{2B_1}{a^2} \right) &= -H_2 \end{aligned} \quad (3.12)$$

Solving equations 3.11 and 3.12, gives

$$\begin{aligned} \begin{pmatrix} -H_0 \\ B_0 \end{pmatrix} &= A_1 \begin{pmatrix} -H_1 \\ B_1 \end{pmatrix} \\ \begin{pmatrix} -H_1 \\ B_1 \end{pmatrix} &= A_2 \begin{pmatrix} -H_2 \\ 0 \end{pmatrix} \end{aligned} \quad (3.13)$$

where A_1 and A_2 denote the following two matrices

$$A_1 = \begin{pmatrix} \frac{\mu+2}{3} & \frac{2(1-\mu)}{3} \frac{1}{b^2} \\ \frac{1-\mu}{3} b^3 & \frac{2\mu+1}{3} \end{pmatrix} \quad (3.14)$$

$$A_2 = \begin{pmatrix} \frac{\mu^{-1}+2}{3} & \frac{2(1-\mu)^{-1}}{3} \frac{1}{a^2} \\ \frac{1-\mu^{-1}}{3} a^3 & \frac{2\mu^{-1}+1}{3} \end{pmatrix} \quad (3.15)$$

From equations 3.13,

$$\begin{pmatrix} -H_0 \\ B_0 \end{pmatrix} = A_1 A_2 \begin{pmatrix} -H_2 \\ 0 \end{pmatrix} \quad (3.16)$$

On calculating $A_1 A_2$, the shielding factor SF can be obtained from equation 3.2 where $H_a = H_e$

$$SF = \frac{H_2}{H_0} = 1 + \frac{2}{9} \frac{(\mu-1)^2}{\mu} \left(1 - \frac{a^3}{b^3}\right) \quad (3.17)$$

Equation 3.17 shows that the shielding factor of this ferromagnetic spherical shield in a uniform field H_a is determined by the material permeability and thickness of the shield, which can be represented in terms of the ratio of inner to outer radius $\frac{a}{b}$. The cases of very thin shield, thin shield and thick shield presented in Fig. 3.3 are with thickness of the shield as 1%, 10% and 20% of the outer radius a . It is obvious that for the same shielding material a thick shield can give a higher shielding factor while higher permeability provides better shielding for the same material.

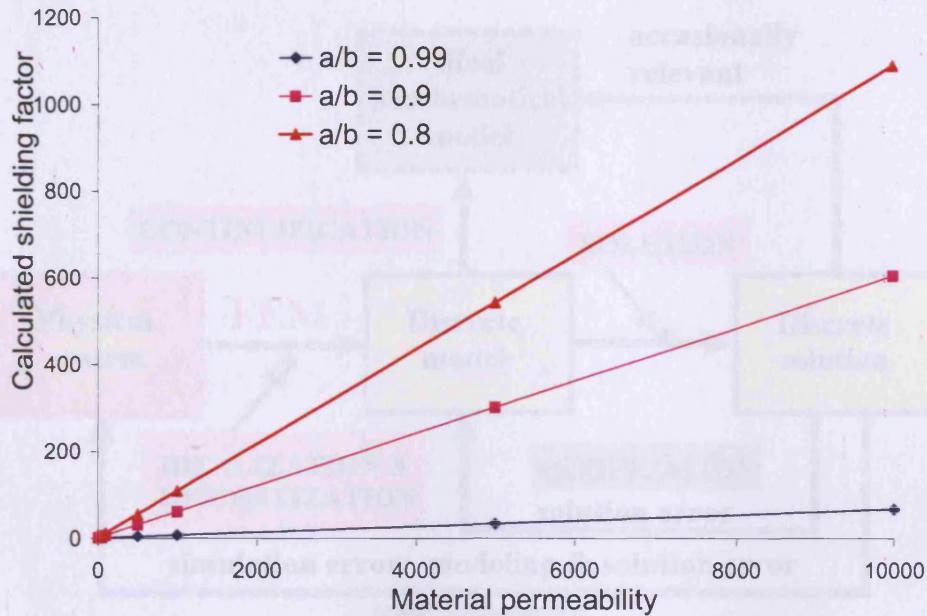


Fig. 3.3 Variation of the calculated shielding factor of spherical shields of different thickness vs. material permeability

Maxwell's equations used above for the calculation of shielding factor can also be solved by the finite element method (FEM). Mathematically, the FEM is used for finding approximate solutions of partial differential equations (PDE) as well as integral equations[4]. The approach is based either on eliminating the differential equations completely or rendering the PDE into equivalent ordinary differential equations, which can be solved using standard techniques such as finite differences. General physical FEM modeling breaks the physical system into a discrete model (which is called meshing). Solutions on the discrete model are computed and then variations and validations will return the results with errors introduced by modeling and solutions. The flow chart in Fig. 3.4 presents the procedures used by FEM software packages in general.

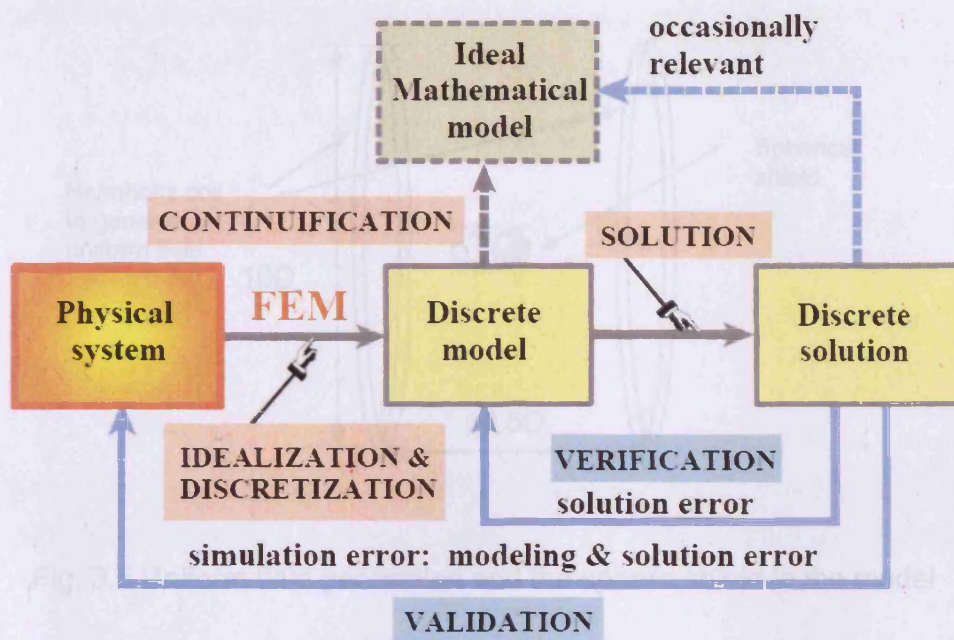


Fig. 3.4 Procedure of FEM software package approaching solutions [5]

The FEM package Opera 2D used in this project is a commercial package from VectorFields Ltd. The same spherical shield in the same conditions as in the case of analytical calculation was studied with Opera 2D.

A pair of Helmholtz coils was constructed in the model to provide a uniform field condition. The diameter of the ferromagnetic spherical shield under study is only 1/10 of the diameter of the Helmholtz coils. This ensures the field uniformity in the central region between the coils where the sphere is placed. The pair of Helmholtz coils and the spherical shield are shown in Fig. 3.5 below,

Fig. 3.5 Magnetic static flux distributions of spheres with same geometry and applied external fields but different permeability from FEM calculation by Opera

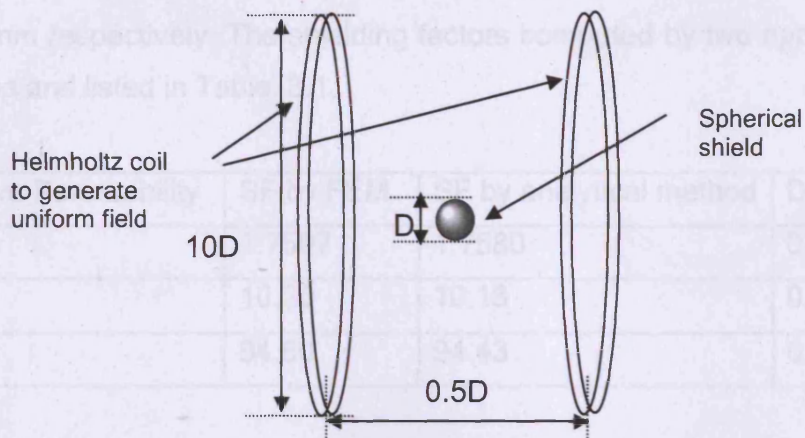


Fig. 3.5 Uniform field generation and the sphere shield in the model

The spherical shields of the same size but with permeabilities 10 and 1000 were modeled. The distribution of flux lines can be seen in Fig. 3.6.

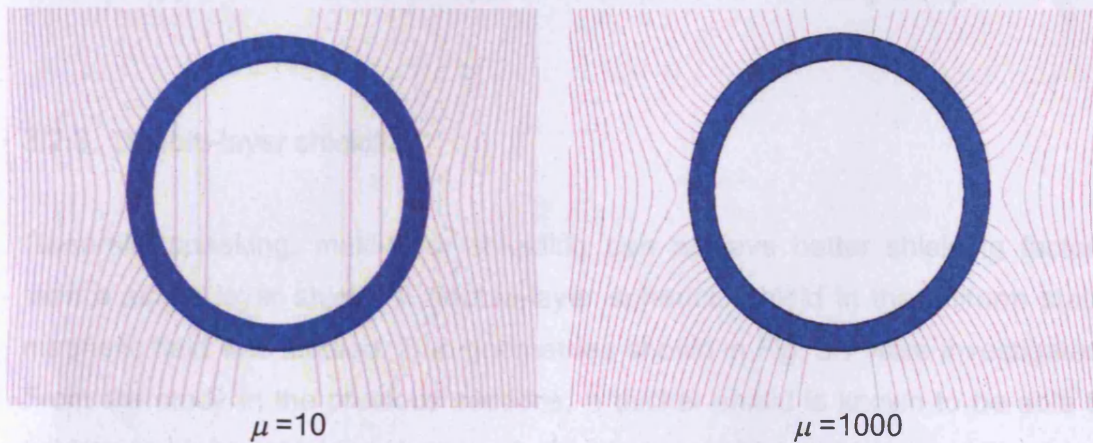


Fig. 3.6 Magneto static flux distributions of spheres with same geometry and applied external fields but different permeability from FEM calculation by Opera

2D

Chapter 3. Magnetic Shielding Theory and Materials

The inner and outer radius a and b of the spherical shield in the model are 10 mm and 12 mm respectively. The shielding factors computed by two approaches are compared and listed in Table. 3.1.

Relative Permeability	SF by FEM	SF by analytical method	Difference
10	1.7597	1.7580	0.10%
100	10.20	10.18	0.20%
1000	94.60	94.43	0.18%

Table. 3.1 Computational and analytical values of SF for a spherical shielding of inner and outer radius 8 mm and 10 mm with different relative permeabilities

It can be seen that the shielding factors obtained by FEM and classical analytical method agree with each other very well in this case. However, the spherical shield is in a simple geometry and the assumed independence of the permeability from the applied field cannot be applied in the practical shielding design.

3.2.3. Double-layer shielding

Generally speaking, multi-layer shielding can achieve better shielding factors than a single layer shield. A double-layer spherical shield in the uniform static magnetic field was studied. Two geometries shown in Fig. 3.7 were investigated. From the study in the previous sections, a thicker shield is known to be able to achieve a higher shielding factor. A double-layer shield which consists of two much thinner layers has good advantages on saving shielding materials if it can achieve a comparable shielding factor to a single thick shield.

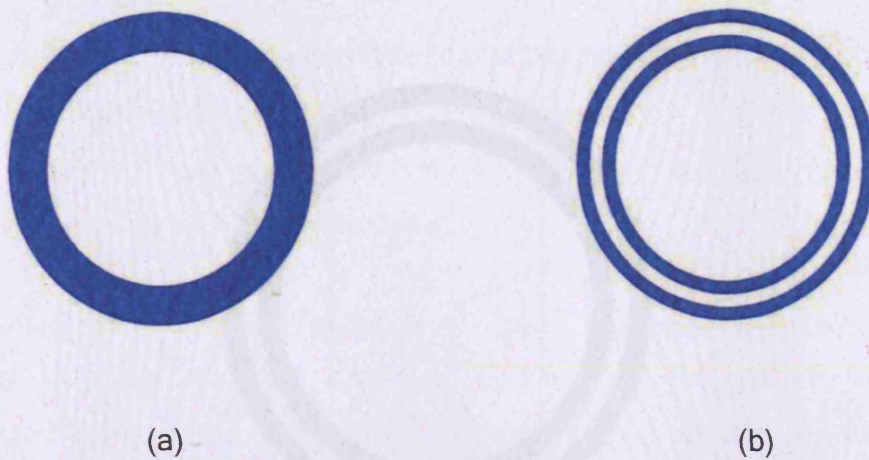


Fig. 3.7. Cross sections of the spherical shields studied in Opera 2D

(a). Single thick 3 mm shield, $\mu_r = 10$, inner and outer radius 9 mm and 12 mm

(b). Double 1 mm thick layers, $\mu_r = 10$, inner and outer radius 9 mm and 12 mm

The total thickness of the shield including the air gap for the double layer shield is the same as the single layer shield. Also the shielded volumes are identical in both cases. Both shields are placed in a uniform field of 200 A/m generated by a pair of Helmholtz coils and the shielding factors at the centre were calculated.

The magneto-static flux distributions of the two shields under the identical applied field conditions are shown in Figs.3.8 and 3.9.

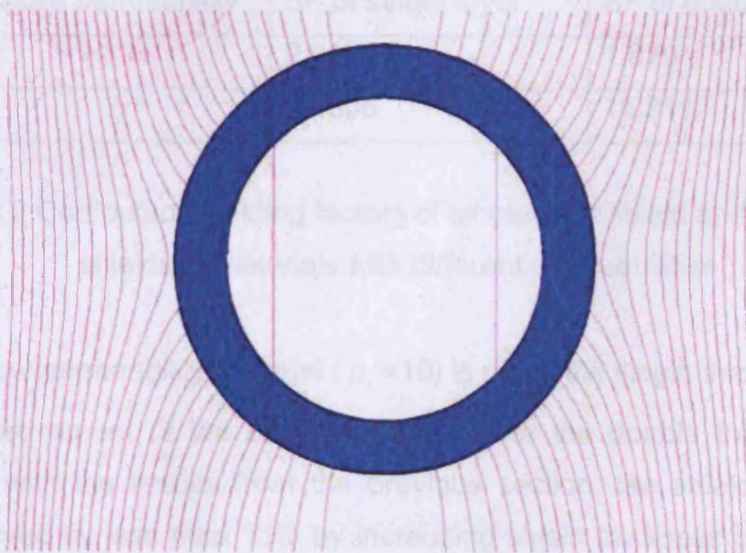


Fig. 3.8 Flux distribution of single 3 mm shield with $\mu_r = 10$

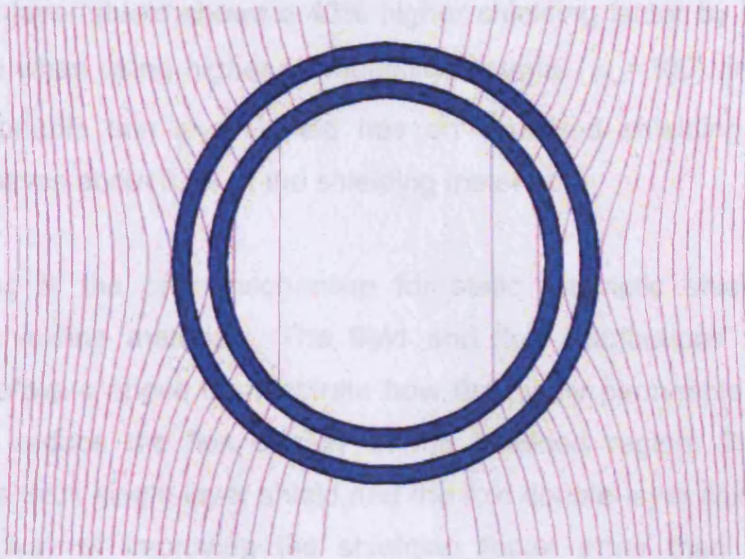


Fig. 3.9 Flux distribution of double 1 mm shield with 1 mm air gap and $\mu_r = 10$

The shielding factors of the shields in these two geometries with material permeability $\mu_r = 10$ and $\mu_r = 100$ are shown in Table. 3.2.

Material relative permeability	SF of single layer	SF of double layer
10	2.043	1.870
100	13.606	18.311

Table. 3.2 Computed shielding factors of single thick shield and double thin shields of materials with different permeabilities

When the low permeability material ($\mu_r = 10$) is used, the single thick shield shows a 10% improvement of the shielding factor over the double thin layer factor. Compared with the results from the previous section, the shielding factor has been improved by less than 15% by increasing shield thickness by 33% (from 2 mm to 3 mm). Simply increasing the thickness of the shield is not an effective way of improving the shielding factor in this case.

The double-layer shield shows a 40% higher shielding factor by introducing a 1 mm air gap when using higher permeability material ($\mu_r=100$). In this particular case, the double thin layer shield has an improved shielding factor, in the meantime saves about 33% of the shielding material.

Flux ducting is the only mechanism for static magnetic shielding with soft magnetic shielding materials. The field and flux distributions from the FEM modeling software above demonstrate how the highly permeable material ducts the flux to reduce the flux density in the shielded region. The comparison between the thick single-layer shield and the thin double-layer shield provides an alternative way of improving the shielding factor other than increasing the thickness of the shield.

3.2.4. Eddy current cancellation and skin depth

According to the Faraday-Lenz law, a time varying magnetic flux generates an e.m.f or voltage, which induce eddy current in an electrically conducting material. This induced current generates magnetic field in the opposite direction to the penetrating field. The eddy current density is dependent on two factors: the frequency of the penetrating field and the material conductivity. Large eddy currents cannot be generated by low frequency magnetic field in conductors such as copper and aluminum. However, sufficient shielding can be achieved by eddy current cancellation in the case of magnetic shielding by super-conducting materials [6].

The skin depth is a measure of the ability of material to resist field penetration. This can be defined as the depth at which the strength of a time varying field attenuates to $\frac{1}{e}$ of its original value inside conducting materials. The skin depth can be calculated from the relative permeability and conductivity of the material

and frequency of the incident field[7]. A simple case, in which field generated by solenoid penetrate into a planar sample, is shown in Fig. 3.10,

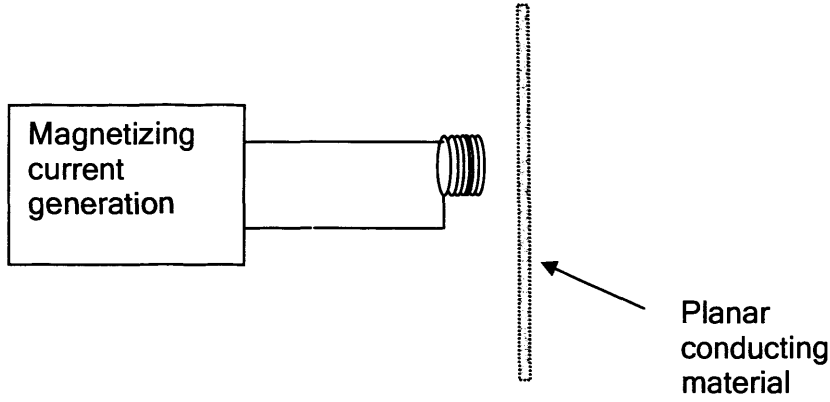


Fig.3.10. Field generated by a solenoid penetrates into a conducting plane

The wave equation for the magnetic field is

$$\nabla^2 H - \epsilon \mu_0 \mu_r \frac{\partial^2 H}{\partial t^2} - \sigma \mu_0 \mu_r \frac{\partial H}{\partial t} = 0 \quad (3.18)$$

where ϵ is material permittivity, σ is material conductivity

and if

$$H = H_0 e^{-i2\pi f t} \quad (3.19)$$

where f is the frequency of the incident magnetic field, then

$$\nabla^2 H + (2\pi f)^2 \epsilon \mu_0 \mu_r H + i2\pi f \sigma \mu_0 \mu_r H = 0 \quad (3.20)$$

with the boundary condition on the surface of the planar medium

$$\nabla^2 H = \frac{\partial^2 H}{\partial z^2} \quad (3.21)$$

so that

$$\frac{\partial^2 H}{\partial z^2} + (2\pi f)^2 \varepsilon \mu_0 \mu_r H + i2\pi f \sigma \mu_0 \mu_r H = 0 \quad (3.22)$$

The general solution of equation is

$$H = H_0 e^{(\alpha + i\beta)z} \quad (3.23)$$

where α and β will be determined in the case of the frequency below the optical range,

$$\beta = \sqrt{\pi f \sigma \mu_0 \mu_r} \quad (3.24)$$

The reciprocal of this term $\frac{1}{\beta}$ is the depth at which the magnetic field strength decays to $\frac{1}{e}$ of its value at the surface. This is the skin depth and a measure of the rate of decay of the time dependent magnetic field as it enters an electrically conducting, magnetically permeable medium.

$$\delta = \sqrt{\frac{1}{\pi f \sigma \mu_0 \mu_r}} \quad (3.25)$$

Material	μ_r (maximum)	σ (Ωm) ⁻¹	f (Hz)	δ (cm)
Iron	1000	10×10^6	10	1.6
			100	0.5
			1000	0.16
Permalloy (Ni-Fe)	1000000	5×10^6	10	0.07
			100	0.02
			1000	0.007
Copper	1	60×10^6	10	20
			100	6.5
			1000	2

Table. 3.3. Skin depth values for penetration of different frequencies of a time-varying field into planar media with assumed frequency independent permeabilities [3]

It can be seen in Table. 3.3. that Permalloy, which has the highest permeability, shows the least skin depth that means it performs the best at stopping field penetration. Although the skin depth is calculated under conditions as field generated from the solenoid penetrating an infinite planar shield, it can be referred to as a general indication of the materials' efficiency to resist the field penetration.

At radio frequencies and higher, non-magnetic conducting materials, such as aluminum and copper offer sufficient shielding efficiency[8]. To achieve enough eddy current cancellation in non-magnetic conducting materials at low frequency, extraordinary high conductivity, which can only be found in superconducting materials, is required. A spherical shield in the same geometry as in previous section 3.2.2, but made of non-magnetic conducting materials is modeled in Opera-2D. Shielding factors, eddy current and flux distributions are calculated.

Chapter 3. Magnetic Shielding Theory and Materials

The spherical shield under study is the same geometry as previous, 10 mm inner radius and 2 mm thick shell. Fig. 3.11 shows the how the flux lines are being pushed away the shielded region by the induced eddy current in a superconducting spherical shield which has the same geometry as the previous cases.

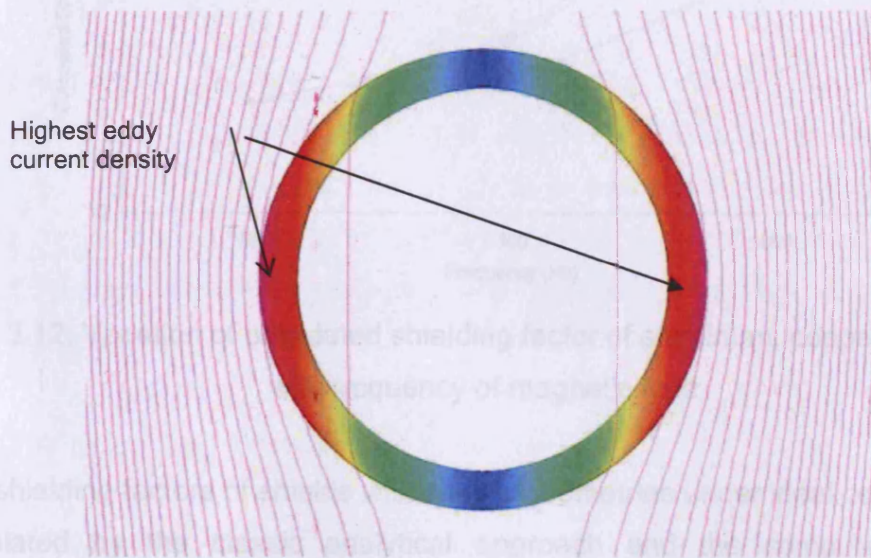


Fig. 3.11 Computed flux distribution and induced eddy current density distribution of the cross section of the highly conducting spherical shield at 50 Hz

Compared with the flux-ducting model in Fig.3.6, the flux lines are almost parallel to the shield surface rather than nearly perpendicular to the surface. The purple and red regions have the highest eddy current density because most flux lines are passing through that region.

The calculated shielding factors are shown in Fig. 3.12 for identical spherical shields made of aluminum, copper and silver whose conductivity are 3.78×10^7 , 5.96×10^7 and 6.30×10^7 siemens respectively. It can be seen that the material with higher conductivity has better shielding performance and it improves with increasing frequency.

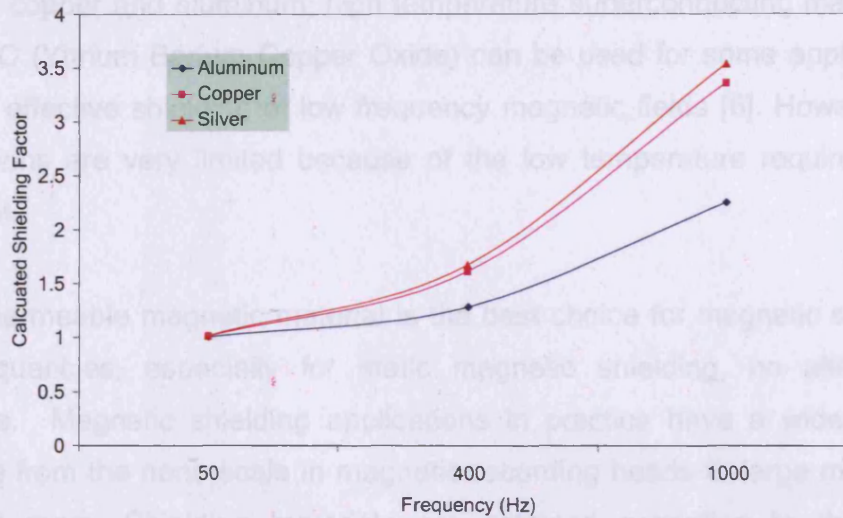


Fig. 3.12, Variation of calculated shielding factor of aluminum, copper and silver with frequency of magnetic field

The shielding factors of shields with simple geometries under ideal conditions are calculated by the classic analytical approach and the computerized FEM approach. The data tables and plots from FEM demonstrate how the flux is ducted by higher permeability materials or resisted by the induced eddy currents in highly conducting materials.

In the case of low frequency magnetic shielding with electrical steels, both flux ducting and eddy current cancellation exist in time varying magnetic shielding. It is more complicated due to the dependence of the relative permeability on the magnetization status of the sample.

3.3 Magnetic shielding materials

Electrical conductivity and magnetic permeability are important properties of shielding materials. At low frequencies such as power frequency, ordinary conducting materials such as copper and aluminum cannot achieve sufficient shielding factor with induced eddy currents.

Chapter 3. Magnetic Shielding Theory and Materials

Besides copper and aluminum, high temperature superconducting material such as YBCO (Yttrium Barium Copper Oxide) can be used for some applications to achieve effective shielding of low frequency magnetic fields [6]. However, these applications are very limited because of the low temperature requirement and high cost.

Highly permeable magnetic material is the best choice for magnetic shielding at low frequencies, especially for static magnetic shielding, no alternative is available. Magnetic shielding applications in practice have a wide range for example from the nano-scale in magnetic recording heads to large magnetically shielded room. Shielding materials are selected according to the material efficiency and cost.

3.3.1 Traditional magnetic shielding materials

The most widely used high permeability magnetic shielding material is Mumetal. Mumetal is the generic name for a nickel based, high-permeability, magnetically "soft" alloy. It includes about 80% nickel and 15% iron, with the balance being copper, molybdenum or chromium, depending on the recipe being used. The important properties of Mumetal are its high initial permeability and resistivity. In some compositions, initial permeabilities are as high as 30000 and the average initial permeability is 15000 - 20000 [9]. Fig. 3.13 shows the permeability of Mumetal of typical composition compared with another high permeability composite Permalloy and two other commonly used alloys, conventional grain-oriented electrical steel and construction steel. It can be seen that Mumetal has the highest permeability at the given flux density.

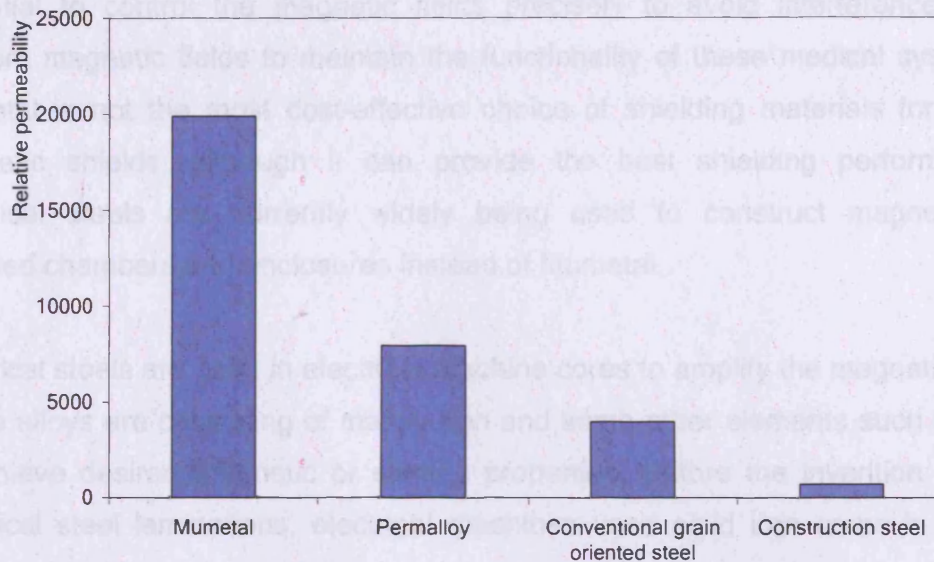


Fig. 3.13. Relative permeabilities of materials, values are approximate and only valid at flux density 0.002 T

Ultra high permeability makes Mumetal a good material for high performance magnetic shielding. Multi-layer shielding constructed by Mumetal is the essential part of accurate magnetic measurements such as biomedical magnetic measurement with SQUIDs (Superconducting Quantum Interference Device) [10]. The sheets of Mumetal can be used for quick fix of shielding problems by simply wrapping the equipment, which needs to be protected.

Mumetal is a shielding material of great importance at the micro-scales. Probably the most widespread use of Mumetal for shielding is presently in magnetic reading heads in magnetic recording systems, in which it is desirable to shield the reading head from stray fields emanating from other regions of the recording medium.

3.3.2 Electrical steel for large-scale shielding

Large-scale magnetic shielding rooms are constructed to protect medical diagnostic systems, such as magnetic resonance imaging machines (MRI). It is

Chapter 3. Magnetic Shielding Theory and Materials

essential to control the magnetic fields precisely to avoid interference from ambient magnetic fields to maintain the functionality of these medical systems. Mumetal is not the most cost-effective choice of shielding materials for large magnetic shields, although it can provide the best shielding performance. Electrical steels are currently widely being used to construct magnetically shielded chambers and enclosures instead of Mumetal.

Electrical steels are used in electrical machine cores to amplify the magnetic flux. These alloys are consisting of mainly iron and some other elements such silicon to achieve desired magnetic or electric properties. Before the invention of the electrical steel laminations, electrical machines used solid iron cores in which heat was generated by eddy currents. To reduce the eddy current loss, silicon was added to increase the resistivity. Also the solid core was replaced by laminations, which is another effective way of reducing the eddy current loss.

There are two main categories of electrical steels namely grain-oriented and non-oriented materials. Grain-oriented steel usually is about 3% silicon and processed to optimize the magnetic permeability along the coil rolling direction. The flux density increases by 30% through the improved permeability at the same applied field, but the saturation is reduced. Grain-oriented electrical steel is mainly adapted to stationary applications where magnetic flux follows the rolling direction, such as in transformer cores. It can be also used for the cores of high efficiency motor and generators.

Non-oriented electrical steel has various silicon contents. Standard grades can be produced with less silicon by improved process technology, for example, M700-65A can be produced with only 0.7% silicon [11]. Non-oriented steels are normally much cheaper than grain-oriented steels and usually targeting the applications where rotational flux is involved such as electric motors and generators.

A hysteresis loop is presented in Fig.3.14 as an example to reveal many important magnetic properties of electrical steels such as permeability, coercivity, saturation and hysteresis loss.

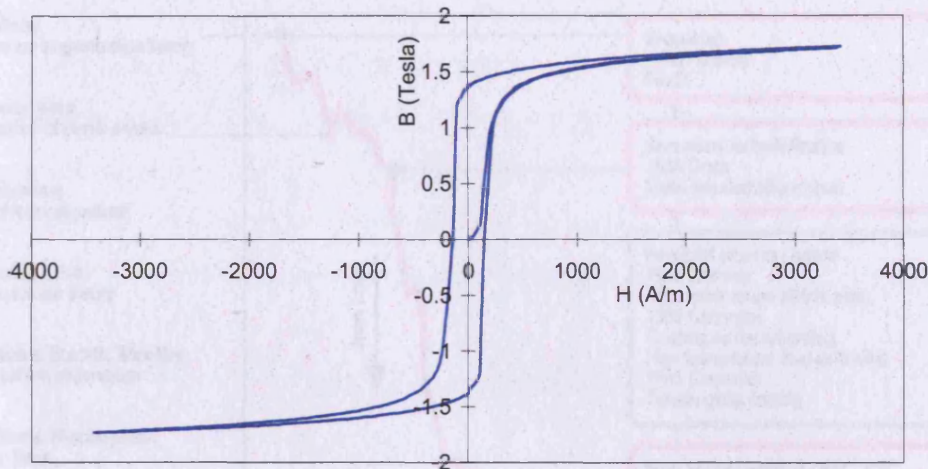


Fig. 3.14. DC hysteresis loop of non-oriented steel strip M800-100A produced with the standard test method[12]

Power loss is the main index for electrical steels as the majority of production is used in power generation, transmission and application where power efficiency is important. The power loss of electrical steel can be analyzed into three components: hysteresis loss, eddy current loss and excess loss. Hysteresis loss is proportional to the enclosed area of the static hysteresis loop. Eddy current loss is caused by the heat effect of the induced eddy current inside the material in the AC applications. The last part is still not fully understood and it is believed that it is due to the domain wall motion and rotation and some other phenomena in micromagnetics [17].

Many technologies have been developed to improve magnetic properties of electrical steel [13]. Domain processing and refinements have been investigated intensively to improve the permeability [13]. The annealing process was also studied to achieve better products. The power loss of electrical steel has been dramatically reduced since it was first produced a hundred years ago. For

example Fig. 3.15 presents the reduction of the power loss in transformers over nearly a hundred years [14].

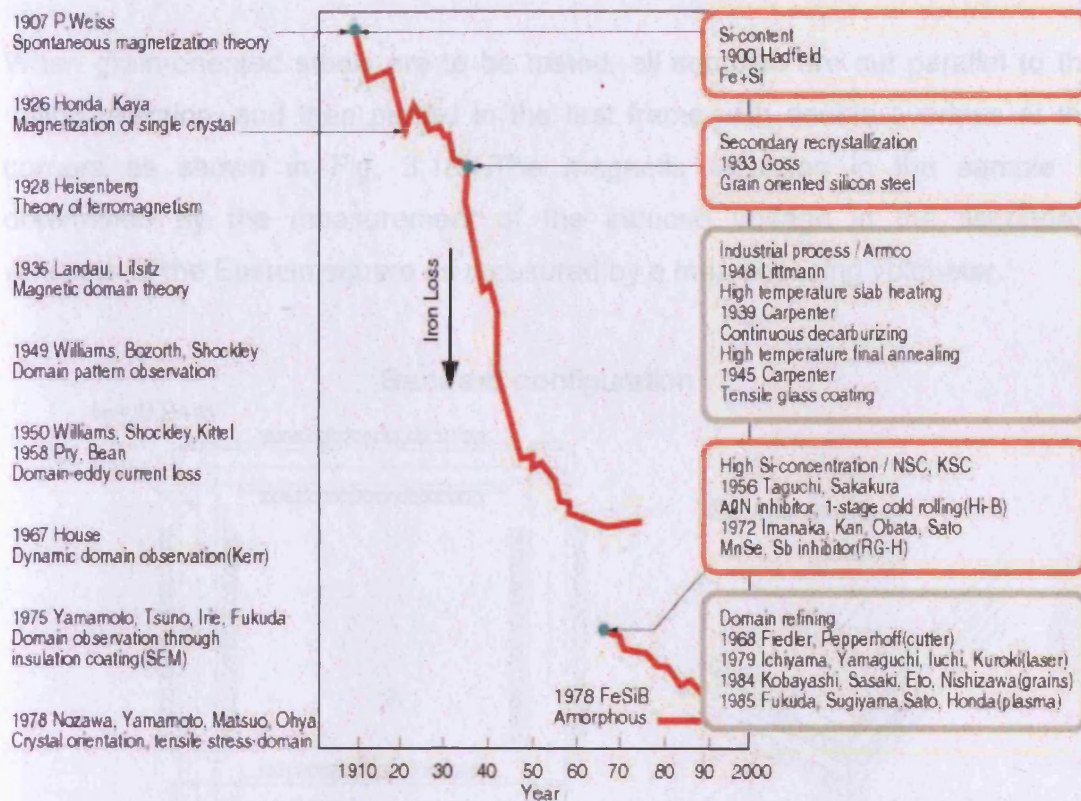


Fig. 3.15 Power loss of the transformer has been reduced over years[14]

3.3.3 Characterization of electrical steels

The magnetic properties of electrical steels have to be measured to help investigate the factors contributing to their magnetic shielding performance. The Epstein frame [15] and single sheet tester [16] are the methods employed to measure the B-H characteristic of the electrical steels samples for magnetic shielding.

The Epstein square method is widely used and recognized as a tool for measuring the specific losses and permeability of electrical steels. Samples

Chapter 3. Magnetic Shielding Theory and Materials

under test have to be cut with care and annealed before being inserted into the Epstein test frame. Typical dimensions of Epstein size samples are 30 mm wide by 305 mm long and usually 24 samples in total are used per test.

When grain-oriented steels are to be tested, all samples are cut parallel to the rolling direction, and then placed in the test frame with double overlaps at the corners as shown in Fig. 3.18. The magnetic induction in the sample is determined by the measurement of the induced voltage in the secondary windings of the Epstein square as measured by a mean sensing voltmeter.

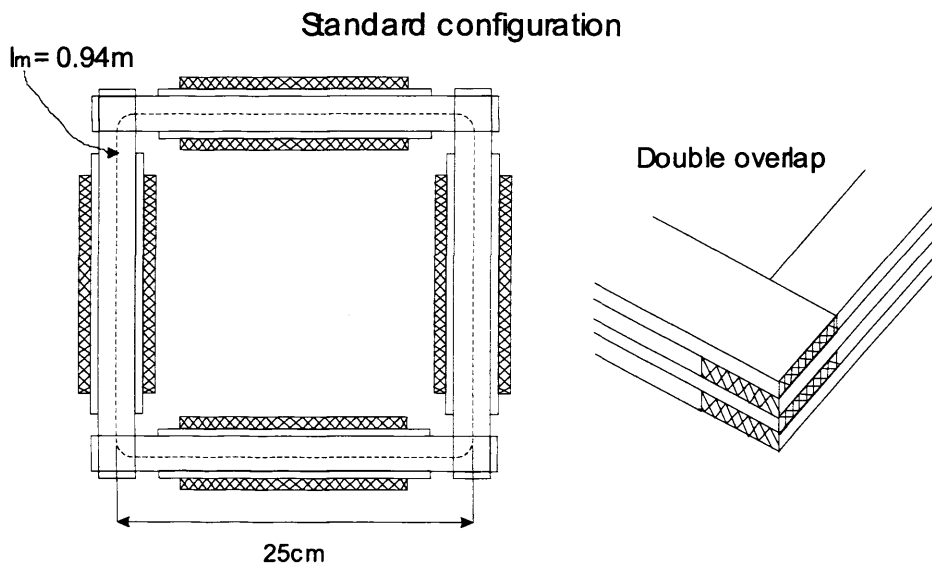


Fig. 3.16 Standard configuration of Epstein Frame test. l_m is the magnetic path length. [15]

The applied magnetic field can be calculated by measuring the magnetizing current in the primary winding. The magnetic induction (flux density), which is calculated by measuring the voltage across secondary winding, can be plotted vs. the variation of applied magnetic field. The B-H characteristic of electrical steel is measured in this way.

The standard test frequency of the Epstein frame is power frequencies (50 Hz or 60 Hz). It can also be used at low frequencies. The measured permeability from Epstein test is affected by the induced eddy current in the cross section of the sample strips. Because the eddy currents are frequency dependent, the measured permeability has a frequency dependency as shown in Fig. 3.17.

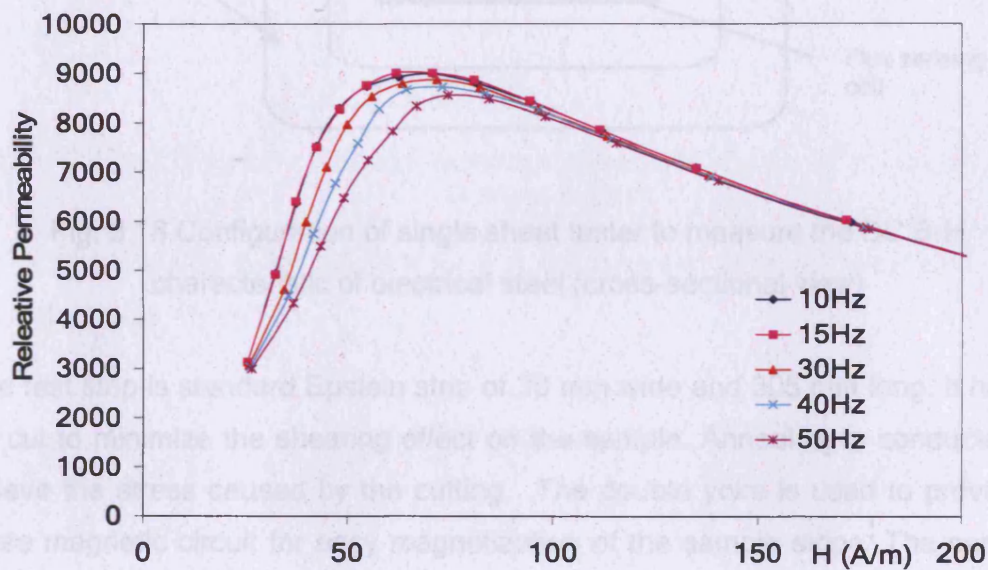


Fig. 3.17 Frequency dependency of the measured permeability using the method of the Epstein frames. The curve at 10Hz is almost on top of 15Hz's.

The B-H characteristic measurement can be carried out at frequency lower than 1 Hz using a single sheet tester to avoid the induced eddy currents. The produced B-H loop can be approximate to the DC property of the sample. The single sheet tester is another test used as a standard to characterize electrical steels[16].

Laboratory configuration is presented as in Fig. 3.18.

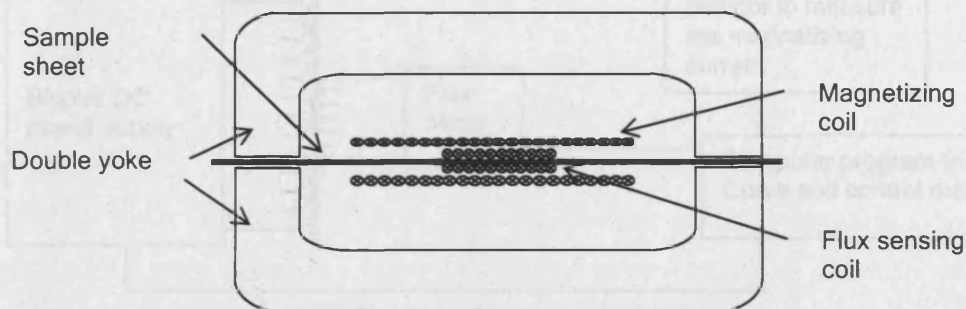


Fig. 3.18 Configuration of single sheet tester to measure the DC B-H characteristic of electrical steel (cross-sectional view)

The test strip is standard Epstein strip of 30 mm wide and 305 mm long. It has to be cut to minimize the shearing effect on the sample. Annealing is conducted to relieve the stress caused by the cutting. The double yoke is used to provide a close magnetic circuit for easy magnetization of the sample stripe. The sensing coil, which is also called B coil, is measuring the magnetic flux in the sample directly rather than calculation from the induced voltage of secondary coil in Epstein frame test. The B coil must be set up close to the sample surface to keep the gap as small as possible to reduce the air flux leakage. The magnetic field strength is calculated from the magnetizing current in the magnetizing solenoid. The block diagram of this method is shown in Fig. 3.19.

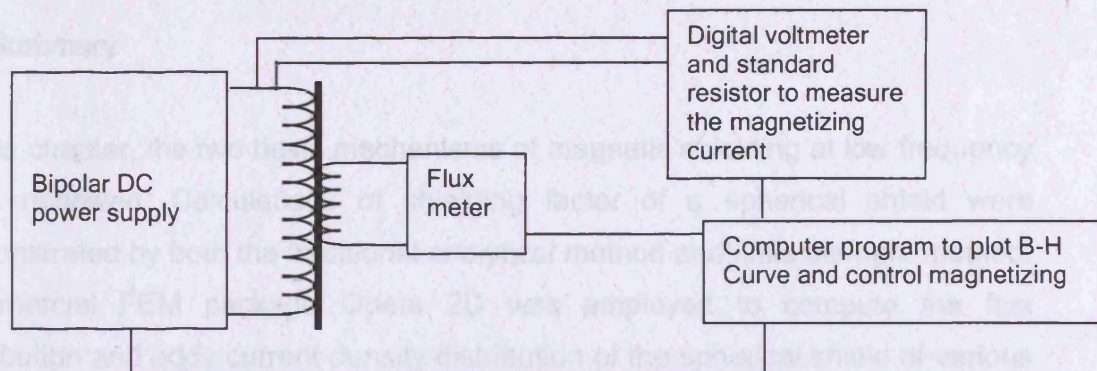


Fig.3.19 Block diagram of the instruments to measure DC B-H loop with a single sheet tester

Fig. 3.20 is the measured DC B-H loop of non-oriented steel M310-50A by using the single sheet tester.

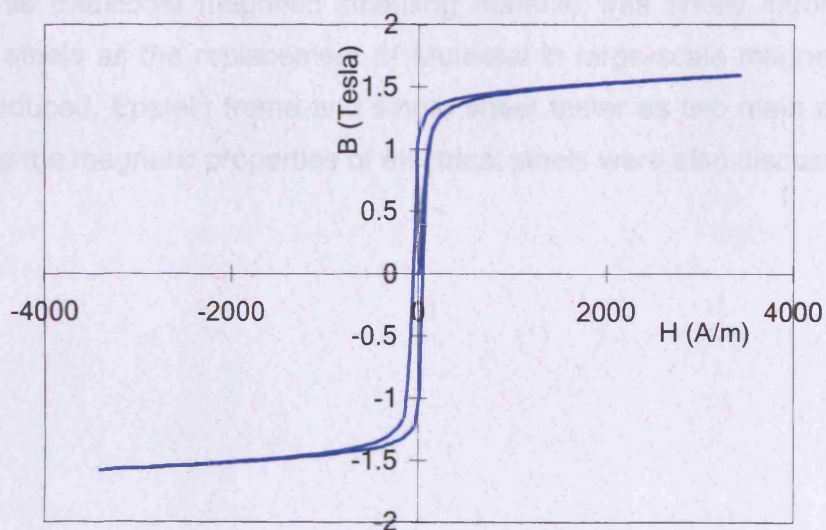


Fig.3.20 Measured DC B-H loop of non-oriented steel M310-50A with the single sheet tester method

3.4 Summary

In this chapter, the two basic mechanisms of magnetic shielding at low frequency were reviewed. Calculations of shielding factor of a spherical shield were demonstrated by both the traditional analytical method and finite element method. Commercial FEM package Opera 2D was employed to compute the flux distribution and eddy current density distribution of the spherical shield of various materials at static and 50 Hz field conditions. These case studies of simple shield in ideal conditions can help us understand the basic theory and lead the way to more complicated shielding problems in chapters 6.

Mumetal as traditional magnetic shielding material was briefly introduced and electrical steels as the replacement of Mumetal in large-scale magnetic shields were introduced. Epstein frame and single sheet tester as two main methods of measuring the magnetic properties of electrical steels were also discussed.

References:

1. Mager, A.J. "*Magnetic Shields*," IEEE Transactions on Magnetics,. Volume: 6, pp. 67-75, 1970.
2. Rikitake, T., *Magnetic and Electromagnetic Shielding*. Tokyo, Springer, 1987.
3. Kraus, J.D., *Electromagnetics*. 4th. ed., McGraw-Hill International, 1992.
4. Silvester, P. P.; Ferrari, R. L., *Finite element for electrical engineers*. Cambridge, Cambridge University Press, 1996.
5. Felippa, C., Course Materials: *Introduction to Finite Element Method*, 2005.
6. Opie, D.B., et al, "*Magnetic shielding by YBCO thick films*," IEEE Transactions on Applied Superconductivity, Volume: 2, Issue: 1, pp.189-192, 1993.
7. Ramo, S.; Whinnery, J. R.; Van Duzer, T., *Fields and waves in communications electronics*, John Wiley and Sons, 1994.

Chapter 3. Magnetic Shielding Theory and Materials

8. Tsaliovich, A., *Electromagnetic shielding handbook for wired and wireless EMC applications*, Springer, 1999.
9. Permeability, Wikipedia,
http://en.wikipedia.org/wiki/Permeability_%28electromagnetism%29#_not_e-hyper
10. Horng, H., "*Bio-magnetic measurements with HTS SQUID Magnetometers in moderated shielding environments*," IEEE Transactions on Applied Superconductivity, Volume: 13, Issue: 2, pp.381-384, 2003.
11. Cogent Power Ltd, *Products Brochure: Non-oriented steels*. Cogent Power Ltd, 2005.
12. British Standard, "*BS EN60404-4, Methods of measurement of d.c. magnetic properties of iron and steel*," British Standard Institute, 1996.
13. Moses, A.J., "*Electrical steels: past present and future developments*," IEE Proceedings A, Science, Measurement and Technology, Volume: 137, Issue: 5, pp. 233-245, 1990.
14. Kan, Y., "*Power loss of electrical steels*" in Nishiyama Memorial Seminar, Iron and Steel Institute of Japan, 1995.
15. British Standard, "*BS EN-60404-2:1998- Methods of measurement of the magnetic properties of electrical steel sheet and strip by means of an Epstein frame*," British Standard Institute. 1998
16. British Standard, "*BS EN 10280:2001-Methods of measurement of the magnetic properties of electrical sheet and strip by means of a single sheet tester*," British Standard Institute. 2001.
17. Moese, A. J., Williams, P. I., Hoshtanar, O. A., "*Real time dynamic domain observation in bulk materials*," Journal of Magnetism and Magnetic Materials, Volume: 304, Issue: 2, pp. 150-154, 2006

Chapter Four

Literature Review

Magnetic fields at static and extremely low frequencies became of concern as disturbances to equipment such as computer display units[1, 2]. Recent research on the potential health effects of magnetic fields at extremely low frequency (DC to 3000 Hz)[3] has lead to published guidelines on limiting the exposure to static and extremely low frequency magnetic fields [4, 5].

Compared with passive magnetic shielding using magnetic materials, previous research work on active shielding concentrated on sensor, cancellation circuits design[6-8] and algorithms for feedback control[9]. Research on passive magnetic shielding has been mainly into two categories:

1. Magnetic shielding theory: Analytical approach to shielding effectiveness of shields of simple geometries under ideal conditions, such as static or quasi-static uniform magnetic fields or fields generated by magnetic dipoles.
2. Experimental assessment of the magnetic shields: Measurement of shielding effectiveness of enclosures, material efficiency and computer aided methods such as finite element modeling design of practical shields of complex geometries.

In this chapter, analytical solutions to shielding factor or the effectiveness of magnetic shields of various shapes at different field conditions are summarized first. Then the studies on the design of shielding enclosures and measurement of material efficiency are reviewed.

4.1 Theoretical Study of the Shielding Effectiveness

Chapter 4. Literature Review

The concept of magnetic shielding can be traced back to the nineteenth century when shielding effectiveness formulae for spherical and cylindrical shells subject to static magnetic field were developed by Rucker and Wills[10, 11]. Magnetic shielding effectiveness can only be calculated precisely for a limited number of very simple shield configurations and field conditions. The constraints of those theoretical calculations are:

1. Concentric shells of spherical or cylindrical symmetry.
2. Shells of constant thickness with no discontinuities.
3. Materials with constant scalar permeability μ .
4. Steady state or moderately low frequency ($< 1\text{MHz}$) sinusoidal magnetic fields that are uniform over the volume of the shielded area.

A set of concentric spherical or cylindrical shields shown as in Fig. 4.1 were studied by Thomas[12].

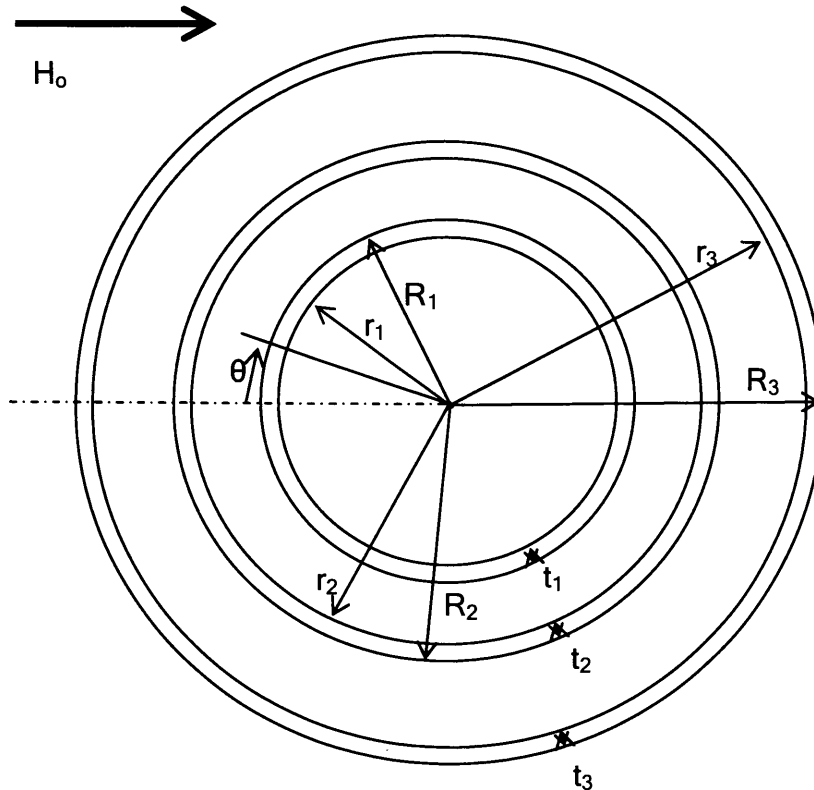


Fig.4.1 The cross section of the concentric multi shell shield system

Chapter 4. Literature Review

Symbol definitions are as following:

S : Shielding factor, the ratio of the uniform ambient dc field H_o to the field H_{in} at the shield centre, with the corresponding induction in the shielding material B_o

S_Δ : Incremental shielding factor, giving the ratio of amplitude of a uniform ac (alternating) field H_Δ superimposed on H_o to the amplitude of the alternating component of the internal field.

μ : DC permeability applying to the conditions of the aforementioned S . It is a function of the induction B_o

μ_Δ : Incremental permeability applying to the conditions of the aforementioned S_Δ and which is dependent on the domain history of the material

ρ : Electrical resistivity of the shield material

v_i : Volume contained by inner surface of shell No. i

V_i : Volume contained by outer surface of shell No. i

R_i : Outer radius of shell No. i

r_i : Inner radius of shell No. i

t_i : Thickness of shell No. i

A_i : Cross section area of outer surface of shell No. i

a_i : Cross section area of inner surface of shell No. i

In the case of the single shell, the DC shielding factor can be calculated with boundary conditions developed from the magnetic potential function[13] :

$$S = \frac{1}{9\mu} \left[(2\mu + 1)(\mu + 2) - 2 \left(\frac{v_1}{V_1} \right) (\mu - 1)^2 \right] \quad (4.1)$$

For the cylindrical shield to the transverse applied field

Chapter 4. Literature Review

$$S = \frac{1}{4\mu} \left[(\mu + 1)^2 - \left(\frac{a_1}{A_1} \right) (\mu - 1)^2 \right] \quad (4.2)$$

If $\mu \gg 1$, these become

$$S = \frac{2}{9} \mu \left(1 - \frac{\nu_1}{V_1} \right) + \frac{1}{9} + \frac{4}{9} \left(1 + \frac{\nu_1}{V_1} \right) \quad (4.3)$$

and

$$S = \frac{1}{4} \mu \left(1 - \frac{a_1}{A} \right) + \frac{1}{2} \left(1 + \frac{a_1}{A_1} \right) \quad (4.4)$$

For a thin shell, equation 4.3 and 4.4 can be further simplified into, for spherical shield

$$S = 1 + \frac{2}{3} \frac{\mu t_1}{R_1} \quad (4.5)$$

and cylindrical shield

$$S = 1 + \frac{1}{2} \frac{\mu t_1}{R_1} \quad (4.6)$$

The error due to the approximation is usually very small, because $\frac{t_1}{R_1}$ is small compared to 1.

The magnetic induction at different positions for the above cases could also be calculated. It can be expressed approximately in terms of polar angle θ for a thin shell of high S , for spherical shield

$$B_1(\theta) = H_0 \left[1 + \frac{3}{2} \frac{R_1}{t_1} \sin \theta \right] \quad (4.7)$$

and cylindrical shield

$$B_1(\theta) = H_0 \left[1 + 2 \frac{R_1}{t_1} \sin \theta \right] \quad (4.8)$$

It can be seen that the induction is dependent on the shell geometry and the position in the shell, but it is independent of permeability as the shielding factor S becomes large compared to unity.

For multiple shells a similar but more complicated boundary value solution is possible. Wills[11] gave the solutions for double shells and the solutions with high

μ and small $\frac{t_i}{R_i}$ are, for double spheres:

$$S = 1 + \frac{2}{3} \frac{\mu_1 t_1}{R_1} + \frac{2}{3} \frac{\mu_2 t_2}{R_2} + \left(\frac{2}{3} \frac{\mu_1 t_1}{R_1} \right) \left(\frac{2}{3} \frac{\mu_2 t_2}{R_2} \right) \left(1 - \frac{V_1}{V_2} \right) \quad (4.9)$$

and for double cylinders:

$$S = 1 + \frac{1}{2} \frac{\mu_1 t_1}{R_1} + \frac{\mu_2 t_2}{R_2} + \left(\frac{1}{2} \frac{\mu_1 t_1}{R_1} \right) \left(\frac{1}{2} \frac{\mu_2 t_2}{R_2} \right) \left(1 - \frac{A_1}{A_2} \right) \quad (4.10)$$

When the two shells are well separated ($V_1/V_2 \ll 1$) and each individual shell has

high $\frac{\mu_i t_i}{R_i}$, the last term dominates, giving further simplification. In this case the

shells are decoupled and their shielding is multiplicative rather than additive, which is the case for small separation ($V_1/V_2 \approx 1$).

In the same way, the total shielding factor for all the shells is

$$S = 1 + S_1 + S_2 + S_3 + \dots + S_N + S_1 \cdot S_2 \left(1 - \frac{V_1}{V_2} \right) \cdot S_3 \left(1 - \frac{V_2}{V_3} \right) \dots S_N \left(1 - \frac{V_{N-1}}{V_N} \right) \quad (4.11)$$

The shielding of a uniform time-varying field can also be analyzed using analytical method. In addition to the flux shunting effect in DC magnetic shielding,

Chapter 4. Literature Review

the induced eddy current cancellation has to be considered. It was concluded by King [14] that the shunting effect dominates at low frequencies, while the induced eddy current cancellation dominates at high frequencies. The solutions of the same shield system as presented in Fig.4.1 under AC conditions are given by Thomas [12] as below, and the shielding effectiveness in this case was shown as an exponential function of the frequency

for spherical shield,

$$S_{\Delta} = \left| \cosh(x + jx) + \left\{ \frac{2}{3} \frac{1}{y + jy} \frac{1}{3} (y + jy) \right\} \sinh(x + jx) \right| \quad (4.12)$$

and cylindrical shield (transverse fields)

$$S_{\Delta} = \left| \cosh(x + jx) + \left\{ \frac{1}{2} \frac{1}{y + jy} + \frac{1}{4} (y + jy) \right\} \sinh(x + jx) \right| \quad (4.13)$$

where x and y are frequency dependent variables below

$$x = 0.505t \sqrt{\frac{\mu_{\Delta} f}{\rho}} \quad (4.14)$$

$$y = 6.05R \sqrt{\frac{f}{\mu_{\Delta} \rho}} \quad (4.15)$$

The major step forward by Thomas[12] is his considerations of how to apply these formula to practical shield design. The following points are summarized:

1. Effects of induction dependent permeability: analytical method cannot solve the shielding problem due to the inability to handle flux dependent permeability.
2. Effect of remnant magnetization.
3. Effect of shielding discontinuities.
4. Effect of non-ideal shapes, which cause a change in shielding factor and a distortion of the internal field.

Chapter 4. Literature Review

To design a practical shielding enclosure, the following information is needed to predict the shielding effectiveness and improve the design:

1. Shielding dimensions and configurations including number of shells, shape and relative orientations of the shells, overall shell dimensions and material thicknesses.
2. Material properties, including: permeability versus induction curves for thickness used, incremental permeability versus biasing induction for the various frequencies and amplitudes of applied alternating fields, electrical resistivity.
3. Shielding fabrication design including location and type of material joints, relative magnetic reluctance of joints, relative electric resistance of joints.
4. Survey of the ambient fields at the shielding location, including approximate map of steady state field and the spectrum of ambient magnetic noise.

Before the theory and design considerations stated above, Schweizer tried adopting the basic formulas on designing a practical system with a set of concentric spherical shells[15]. Later in 1970, the recommended route for magnetic shielding design shown above by Thomas was demonstrated by Patton in designing a shielding room for geomagnetic fields[16]. Another good review of the theoretical work around this time was from Mayer[17] in 1970. He gave a microscopic analysis of the relationship between domain wall motion at different frequencies and the penetration depth of the incident magnetic field.

Although the shielding theory under ideal conditions has been developed into some applications by the researchers above, it was still limited to uniform field conditions. Studies of shielding of non-uniform fields are more valuable for practical works. Shields used for non-uniform fields from different source have been studied. Transmission line theory was first employed by Schelkunoff[18] to investigate the shielding of a non-uniform magnetic field from a dipole source. His

Chapter 4. Literature Review

work was extended by Adams and Mills[19]. Although this theory is only based on an ideal normal incidence to the shield by the incident field, it could be applied for some engineering applications[20].

To study the shielding under non-uniform field condition, shielding effectiveness of the cylindrical shield to magnetic fields from a dipole source was computed by Greifinger et. al in 1980[21]. Measurements with an ELF magnetic dipole source and a Mumetal shield in the shape of a cylindrical shell with one welded endcap were carried out to compare measured shielding factors with the computed results. The geometry and coordinate system used is shown in Fig. 4.2.

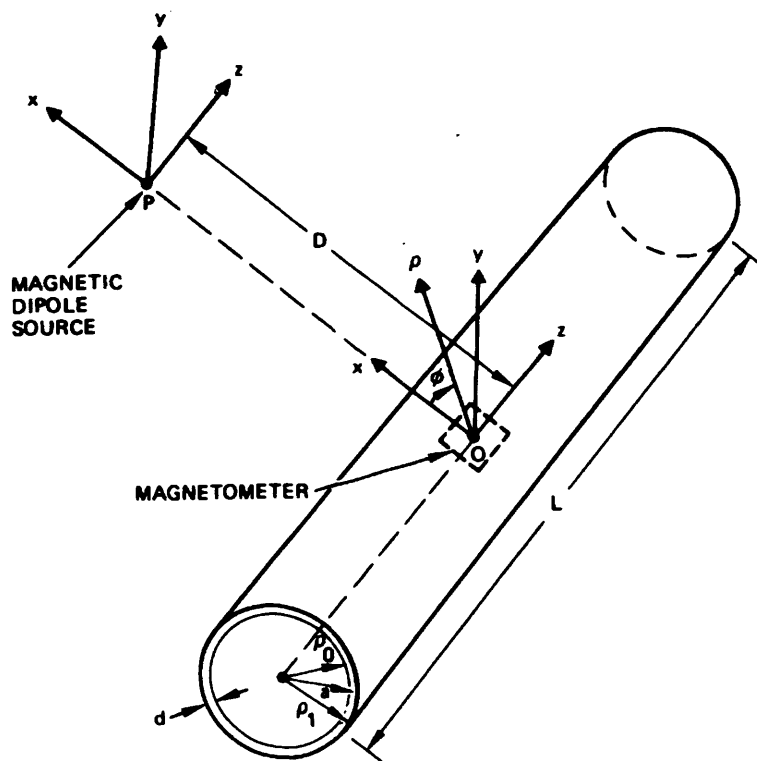


Fig. 4.2. Geometry and coordinate system used in analysis of magnetic shielding against a non-uniform magnetic field from a dipole source, where L is the length of the cylinder, D is the separation distance between the dipole source and the cylinder [21].

The computed shielding effectiveness of the cylinder was demonstrated as a function of separation distance between the dipole and the shield and also dependent on the dipole orientation. As shown in Fig. 4.3, the same cylinder has a better shielding effectiveness when the dipole orientation is parallel to the x-Axis than parallel to the y-Axis. For the dipole orientation parallel to either the x-Axis or y-Axis, the cylinder's shielding effectiveness increases as the dipole moves towards the cylinder. It also can be seen that the shape of the cylinder ($L/a = 5$ or $L/a = \infty$) only makes a small difference as the dipole moves far away from the shield.

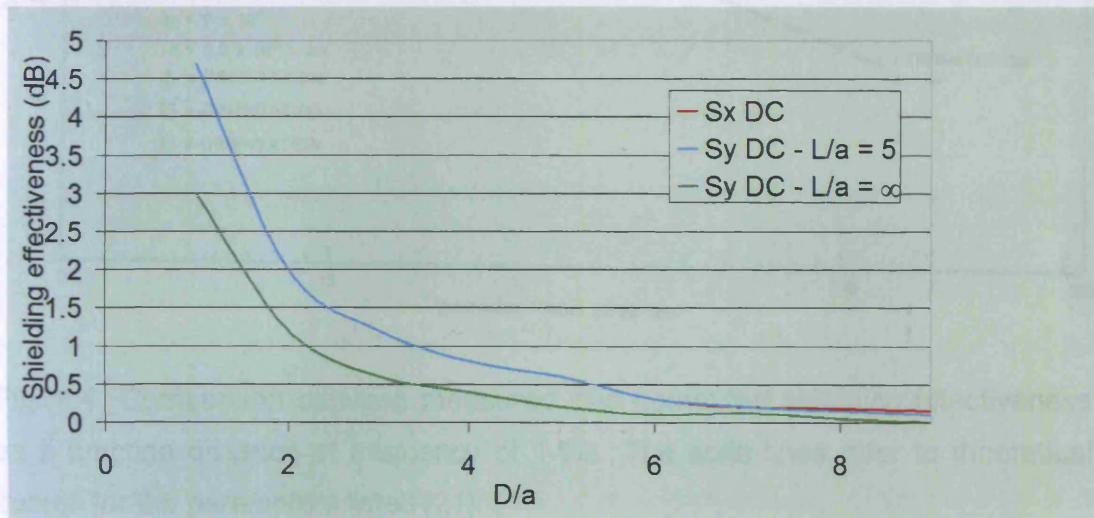


Fig. 4.3. Increase in shielding effectiveness due to non-uniformity of dipole filed

Where S_x DC: DC shielding effectiveness as the dipole parallel to x axis.

S_y DC: DC shielding effectiveness as the dipole parallel to y axis.

a: the diameter of the cylinder. L: the length of the cylinder.

From the summary of the measurements as in Fig. 4.4 and 4.5, the theoretical results have a satisfactory fit to the measurements when $\mu_r = 2.0 \times 10^4$.

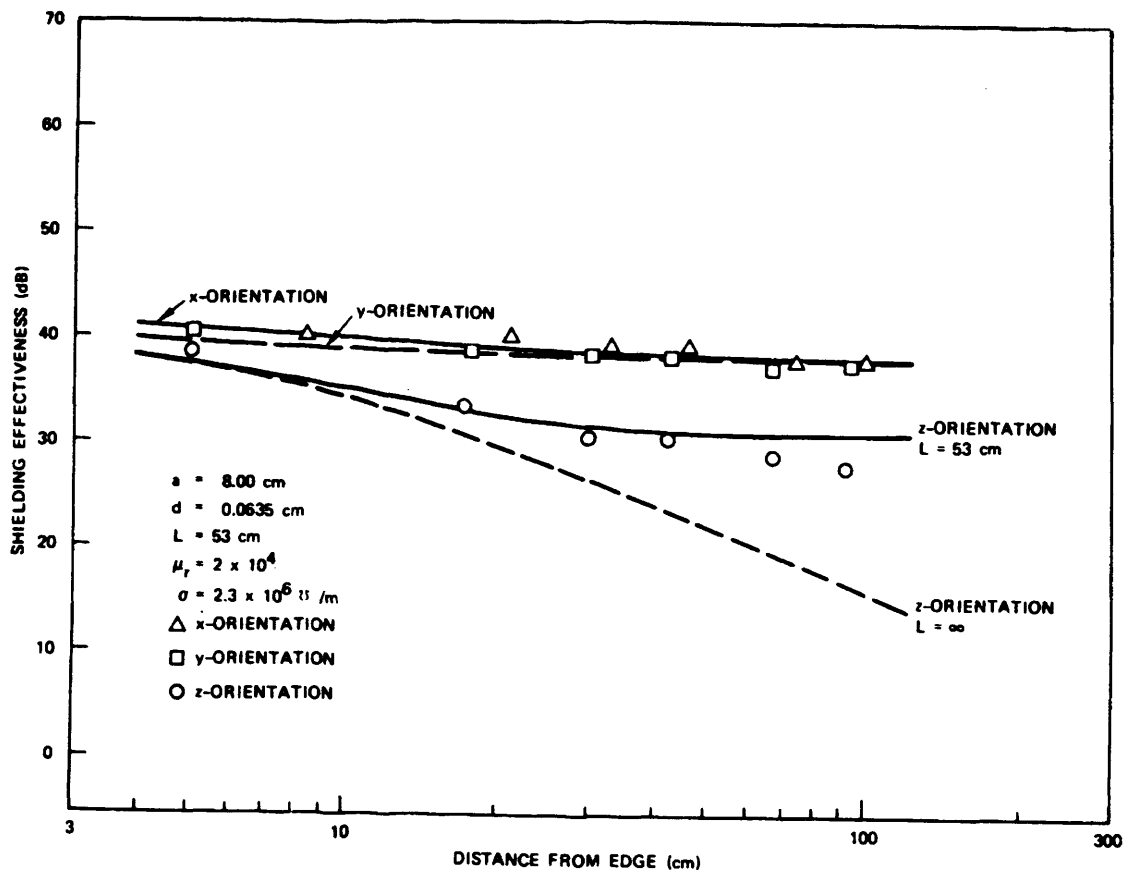


Fig. 4.4. Comparison between measured and computed shielding effectiveness as a function distance at frequency of 1 Hz. The solid lines refer to theoretical curves for the parameters listed [21].

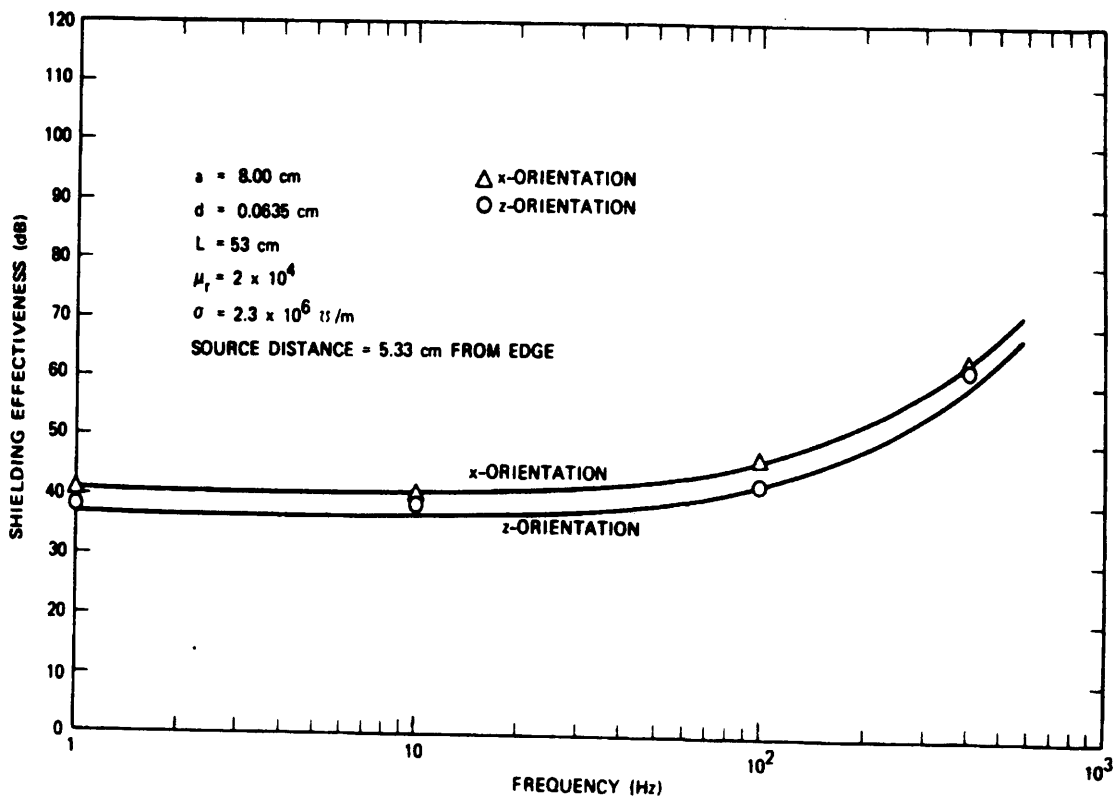


Fig. 4.5. Comparison between measured and computed shielding effectiveness as a function of frequency. The solid lines refer to the theoretical curves for the parameters listed [21].

In 1988, Moser[22] studied low frequency low impedance shielding with two coaxial loops separated by an infinite plate shown as Fig. 4.6.

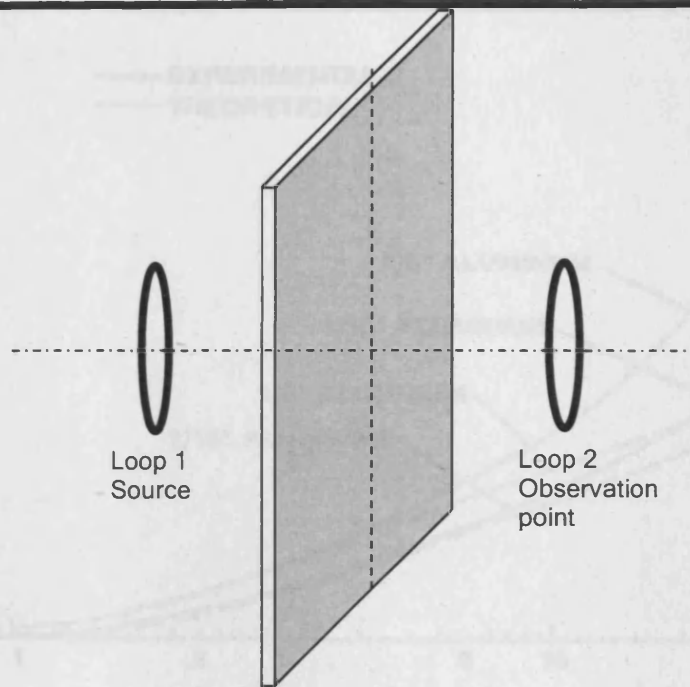


Fig. 4.6. Coaxial loops separated by an infinite plate [22]

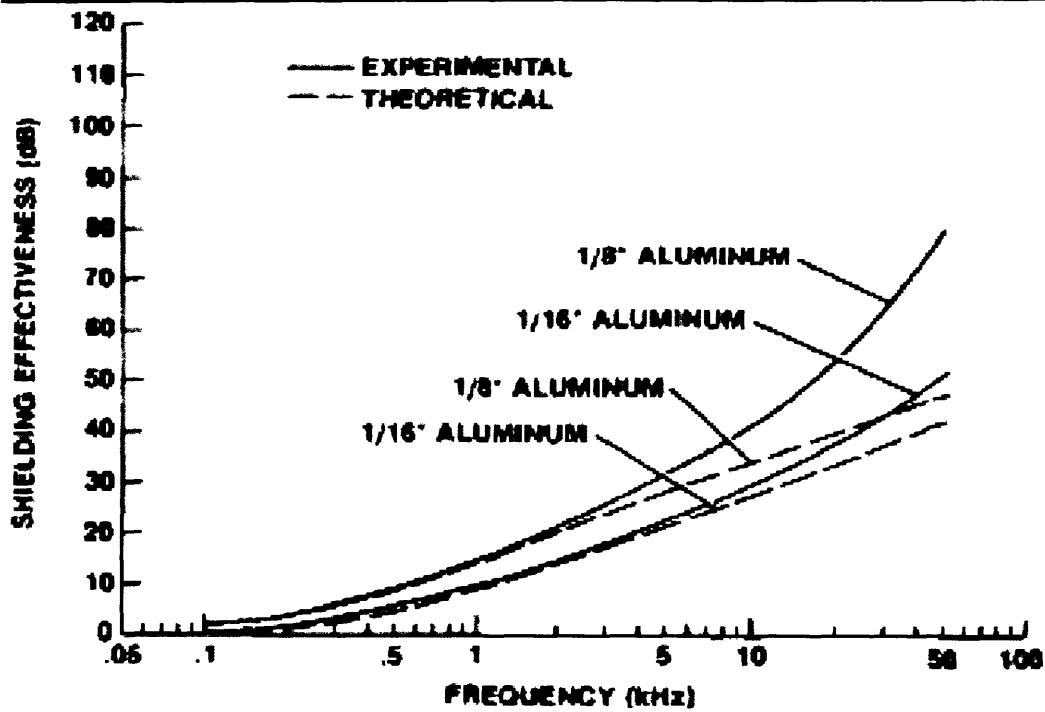
The shielding effectiveness was expressed as

$$S = R + A + B \quad (4.16)$$

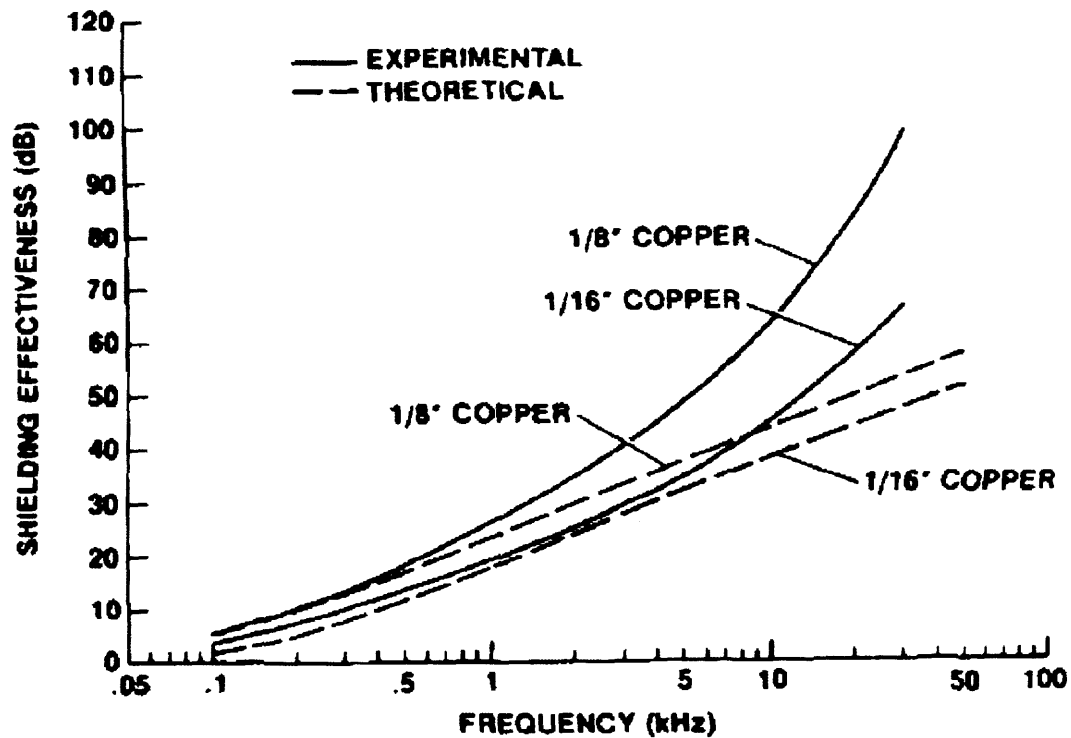
where R is the contribution from reflection loss, A is from material absorption and B is from penetration loss.

The transmission line method was employed to calculate the shielding effectiveness of plates made of aluminum, copper and steel. Theoretical results compared with the measured are shown in Fig. 4.7:

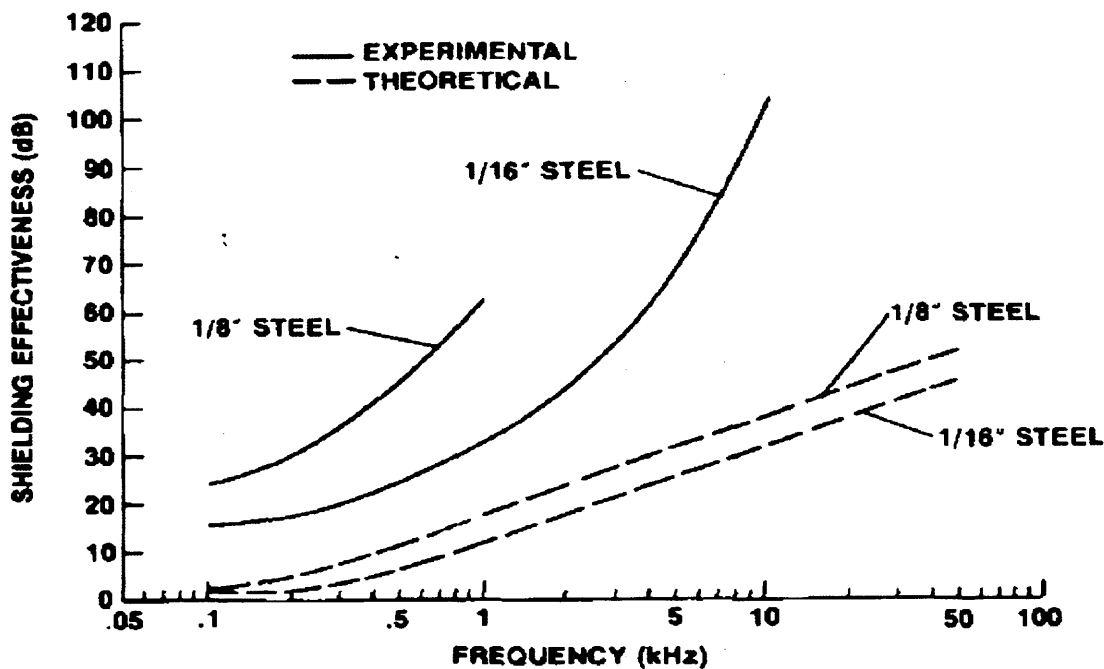
Chapter 4. Literature Review



a). Aluminum



b). Copper



c). Steel

Fig. 4.7. Comparison of shielding effectiveness S for different materials by theoretical calculation and measurements [22].

Along with the development of transmission line theory to calculate shielding effectiveness, the circuit approach was studied by Wheeler[23] in 1958 and then further developed by Miedzinski[24]. The basic electric circuit-like relationships for magnetic field shielding were demonstrated by Miller and Bridges[25]. In 1968, Miller and Bridges reviewed this approach for both electric and magnetic field shielding[26]. Fig. 4.8 shows the calculated shielding effectiveness by the circuit approach of aluminum sphere 45.72 cm (18 inch) radius and 0.16 cm (1/16-inch) thick in a uniform sinusoidal magnetic field.

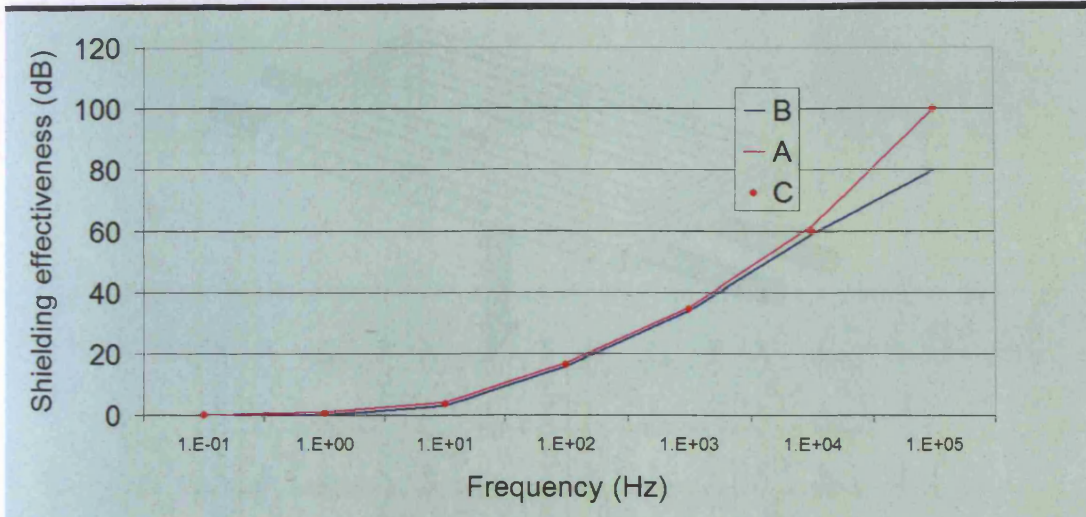


Fig. 4.8. Effective circuit and the calculated shielding effectiveness of aluminum sphere 45.72 cm (18 inch) radius and 0.16 cm (1/16 inch) thick in a sinusoidal uniform magnetic [26].

A: Based on Results from scattering theory

B: Calculated from "Shorted - Turn" analysis

C: Form Assumed from simplified transient analysis

Bridges published another paper in 1988 as a further development of the circuit approach[27]. He demonstrated that the shielding effectiveness of an enclosure at low frequencies can be readily computed using a circuit approach. This technique could include the effects of the shielding material property and also details of the geometry of the enclosure. By working with the circuit analogue, penetration by transient fields can be computed as well. The most recent work on circuit approach of shielding effectiveness was by Frix and Karady in 1997[28]. They created a circuit model of a conducting shield for a pair of power transmission cables as shown in Fig. 4.9 and demonstrated that the circuit approach can provide a rapid numerical estimation of shielding efficiency and power loss in the conducting shields.

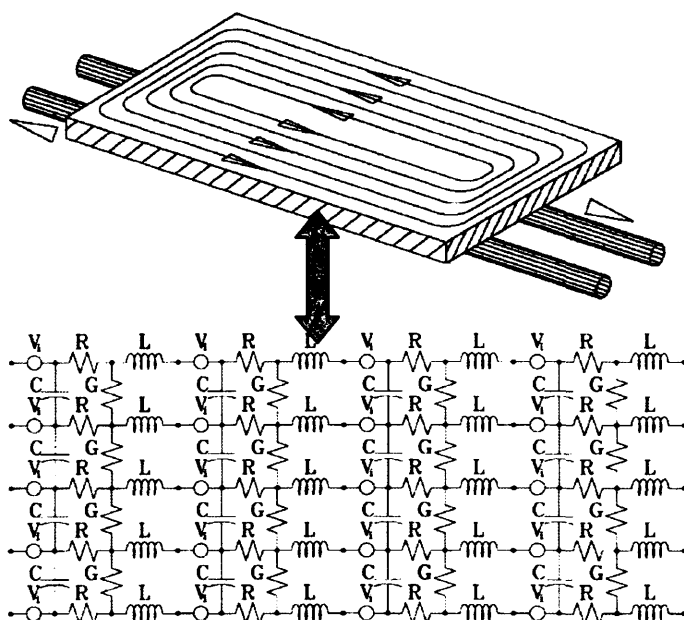


Fig. 4.9. Planar conducting metal shield for a pair of power transmission cables and the circuitry model of the shield [28].

Hoburg studied the analytical solutions of quasi-static magnetic shielding effectiveness of long cylinders and spheres in both uniform and dipole fields[29]. With these specific examples, induced eddy currents and flux shunting mechanisms were studied separately in highly conducting and highly permeable mediums first. Then the simultaneous effect upon shielding by the materials of high permeability and conductivity was investigated. This work paid more attention to material's properties (permeability and conductivity) and also pointed out the effect of flux density dependent permeability on shielding effect [29].

Because of the limitation of analytical solution on the simple geometries and ideal field conditions, Hasselgren and Luomi investigated the geometrical aspects of magnetic shielding at extremely low frequencies with finite element methods in 1995[30]. The finite element method was evaluated by measuring a practical case as shown in Fig.4.10 and the results are in Fig. 4.11.

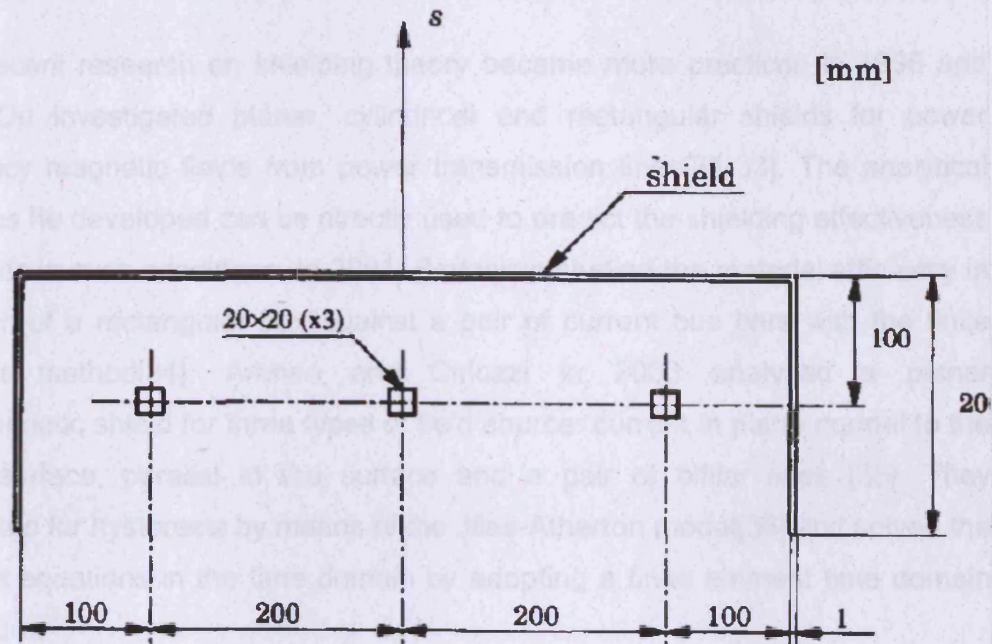


Fig. 4.10. Cross-section of the three bus bars and the shield geometry for a three-sided shield configuration [30].

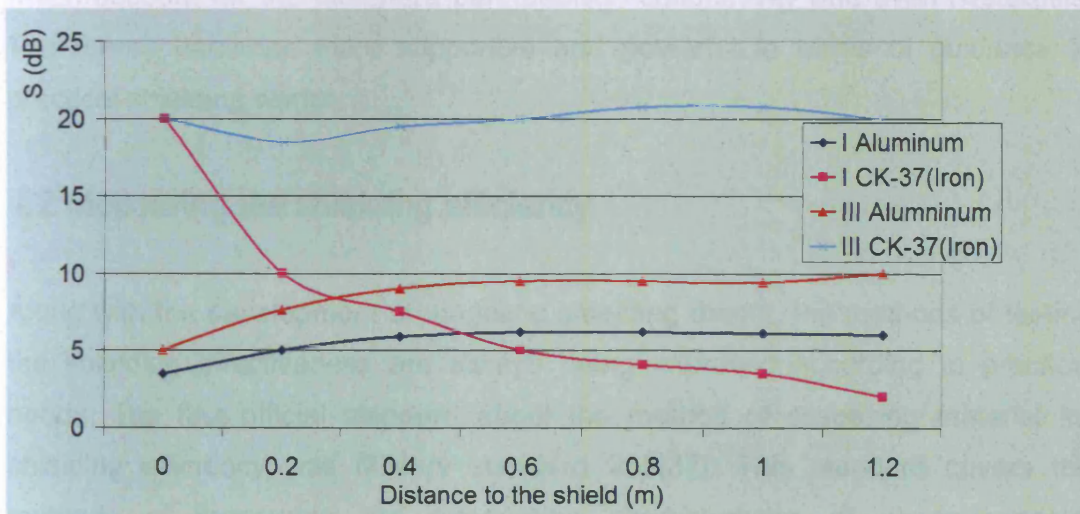


Fig.4.11. Shielding effectiveness S along the symmetry axis above the shields applied on the bus bars. Shield thickness $d = 1$ mm. Measurements are indicated with markers [30].

More recent research on shielding theory became more practical. In 1996 and 1999, Du investigated planar, cylindrical and rectangular shields for power frequency magnetic fields from power transmission lines[31-33]. The analytical solutions he developed can be directly used to predict the shielding effectiveness of shields in such conditions. In 2001, Bottasicio studied the material efficiency in the form of a rectangular box against a pair of current bus bars with the finite element method[34]. Araneo and Celozzi in 2003 analyzed a planar ferromagnetic shield for three types of field source: current in plane normal to the shield surface, parallel to the surface and a pair of bifilar lines [35]. They accounted for hysteresis by means of the Jiles-Atherton model[36] and solved the relevant equations in the time domain by adopting a finite element time domain procedure.

Over a period of 100 years, the magnetic shielding theory has developed from analytical methods of simple geometries under ideal uniform field conditions to various numerical methods for complex geometries at non-ideal field conditions which account for the material's permeability, conductivity and even hysteresis. The theory becomes more supportive and powerful in terms of guidance to practical shielding works.

4.2 Measuring the shielding efficiency

Along with the development of magnetic shielding theory, the methods of testing the shielding effectiveness are always being improved according to practical needs. The first official standard about the method of assessing material for shielding efficiency was Military standard 285[37]. This standard covers the methods of measuring the attenuation characteristics of electromagnetic shielding enclosures used for electronic test purposes over the frequency range 10 kHz to 10,000 MHz. Fig. 4.12 is the defined test setup.

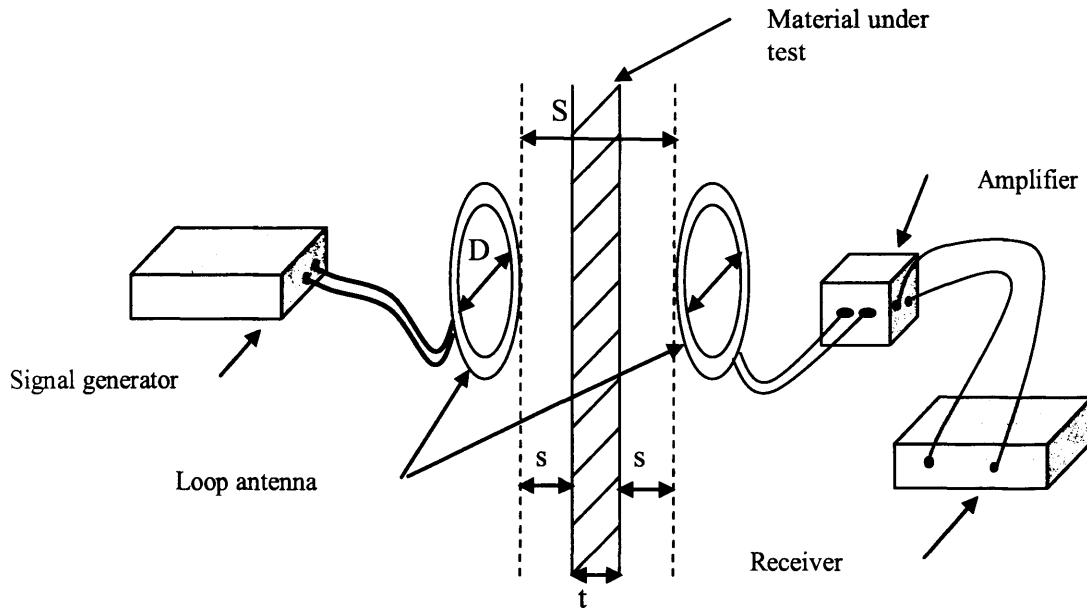


Fig. 4.12. Test setup of MIL-STD-285 to measure magnetic shielding effectiveness of the enclosure

The attenuation is defined as the ratio, expressed in decibels (db) of the received powers on the opposite sides of a shield when the shield is illuminated by electromagnetic radiation. This ratio is also defined as the shielding effectiveness of the electromagnetic enclosures. In the case of magnetic shielding at low frequency, the shielding effectiveness can be expressed as the ratio of the magnetic field strength. Although the lower end of the frequency spectrum covered by MIL-STD-285 is only 10 kHz, the methodology of measuring the insertion loss or attenuation of the shielding material was widely adopted in the practice of measuring shielding effectiveness within the static and extremely low frequency range. The measurement (Fig.4.6) carried out by Moser[22] was an example of extending this method to the 100 Hz region.

In 1985, the IEEE published IEEE STD 299 which introduced another method for measuring the shielding effectiveness of shielding enclosures[38]. The updated version in 1997 can be used to determine the shielding effectiveness of an enclosure with longest linear dimension less than 2 metres. The original

applicable spectrum of this method is from 1 MHz up, but it can be extended down to 50 Hz. Fig. 4.13 is the schematic diagram of this test setup in which the receiver and transmitter have to be the appropriate types for the test frequency bands [38].

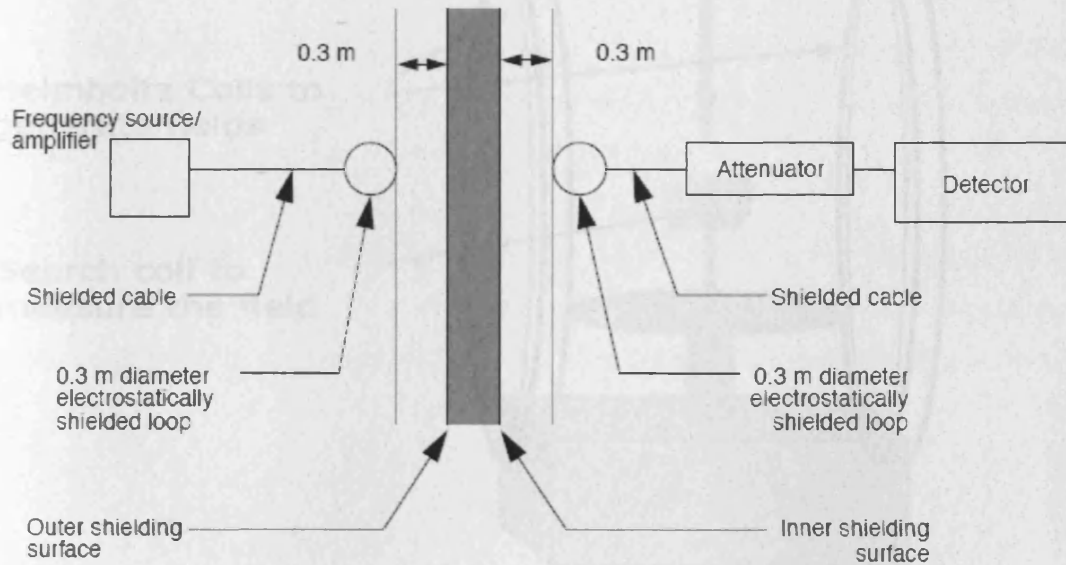


Fig. 4.13. Schematic diagram of IEEE-STD-299 test setup to measure the shielding efficiency of large shielding enclosures [38].

Another important standard test method is ASTM A698/A698M (first published in 1974 and re-approved in 1997) from American Society of Testing Materials (ASTM). This test method provides means for determining the performance quality of a magnetic shield when placed in a magnetic field of alternating polarity (normally 50/ 60 Hz) [40].

In this standard test, a pair of Helmholtz coils is used to establish the desired value of alternating magnetic field strength within suitable uniformity in the defined region between the coils. A sensing coil detects the strength of the field inside the standard coil. The attenuation of the established alternating magnetic

field due to the insertion of a magnetic shield around the point of measurements can be determined in the way as shown in Fig. 4.14.

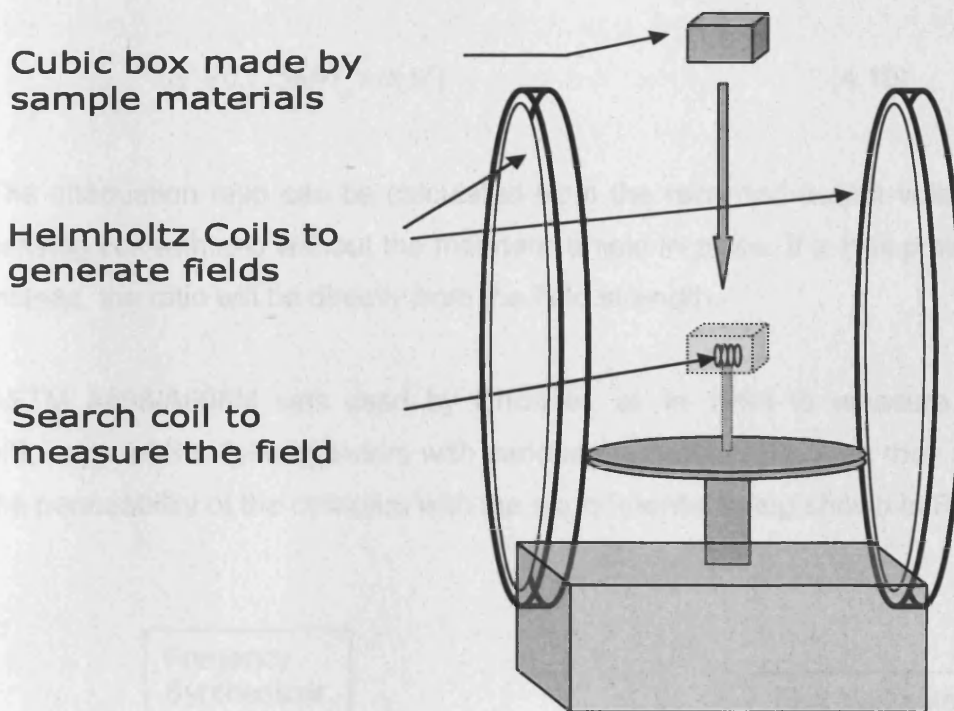


Fig. 4. 14. Setup of ASMT A698/A698M [40].

The connections of the standard coils and sensing coils are as in Fig. 4.15.

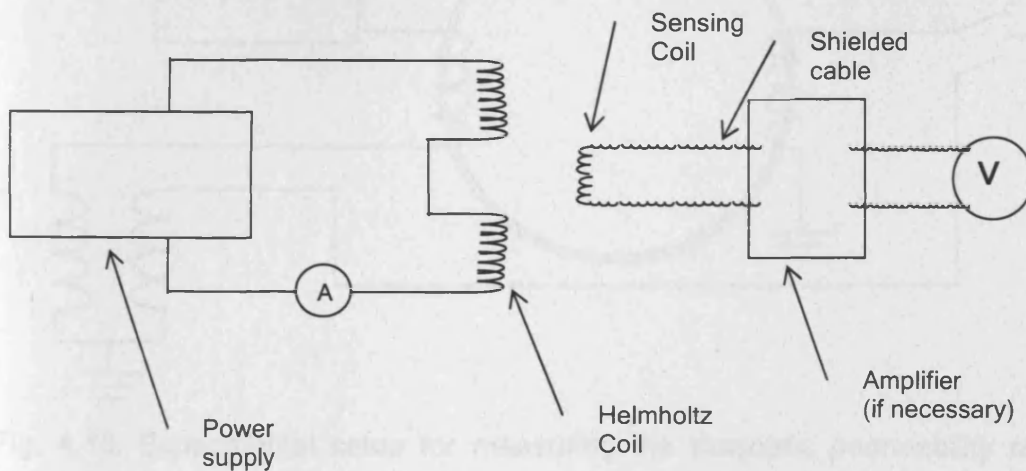


Fig. 4.15. Diagram of the connections for the test [40]

The magnetic field strength in the central test area established by Helmholtz coils shall be calculated as follows:

$$H = 0.7156NI_p / R(SI) \quad (4.16)$$

The attenuation ratio can be calculated from the recorded output voltage of the sensing coil with and without the magnetic shield in place. If a Hall probe is used instead, the ratio will be directly from the field strength.

ASTM A698/A698M was used by Chun et. al. in 1999 to measure shielding efficiency of 3% SiFe cylinders with various diameters [39]. Also they measured the permeability of the cylinders with the experimental setup shown in Fig. 4.16.

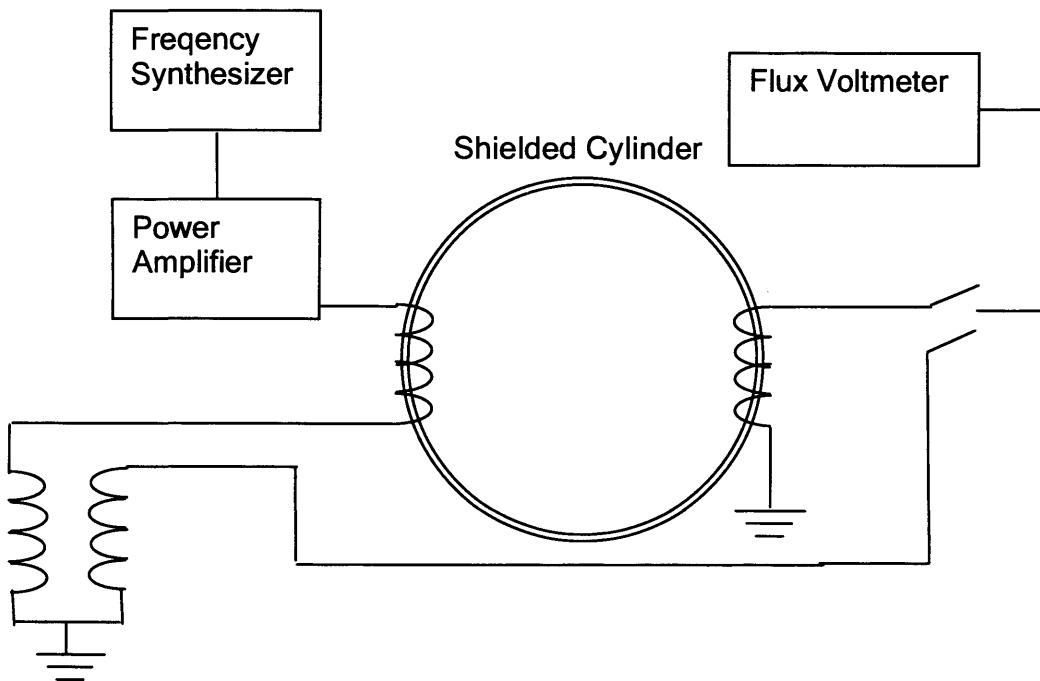
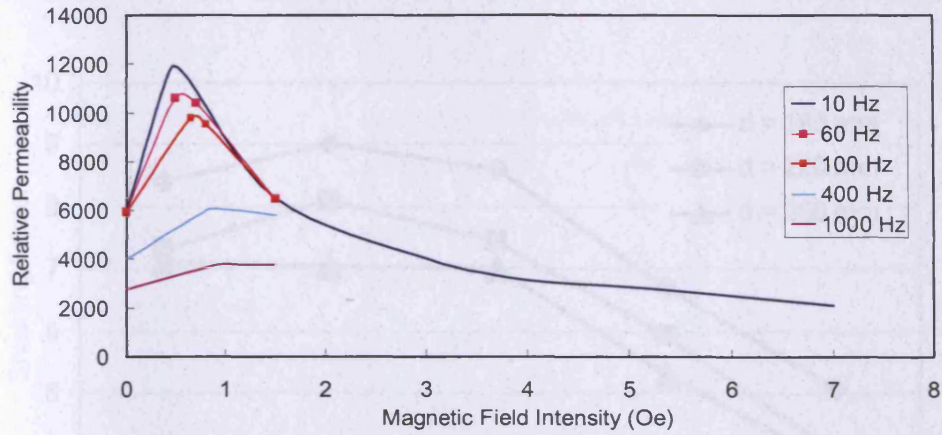


Fig. 4.16. Experimental setup for measuring the magnetic permeability of the cylinder in itself [39]

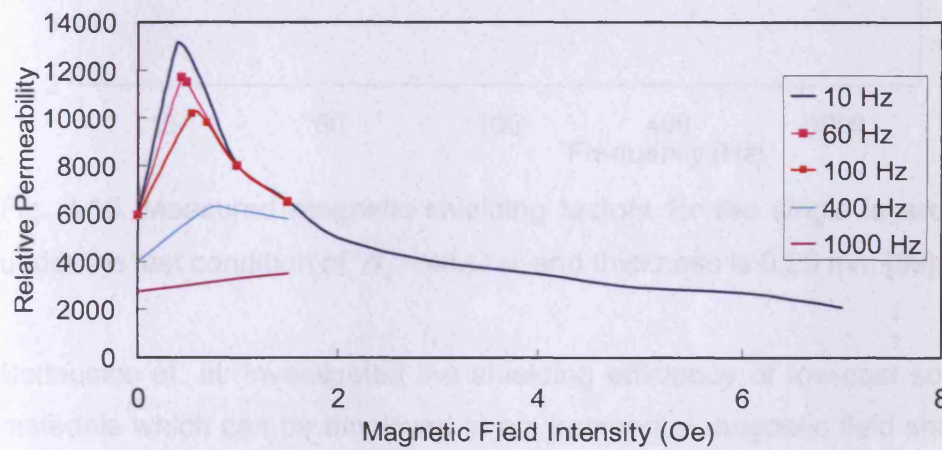
Chapter 4. Literature Review

It can be seen from the measured permeability in Fig. 4.17 that the higher permeability is obtained with the larger diameter and the lower frequency respectively. However, it is difficult to determine the shielding factor only from the permeability data due to different magnetic inductions of the cylinders because of their dimensions. Therefore, although the largest cylinder has the best permeability, the smallest cylinder showed the best measured shielding effectiveness.

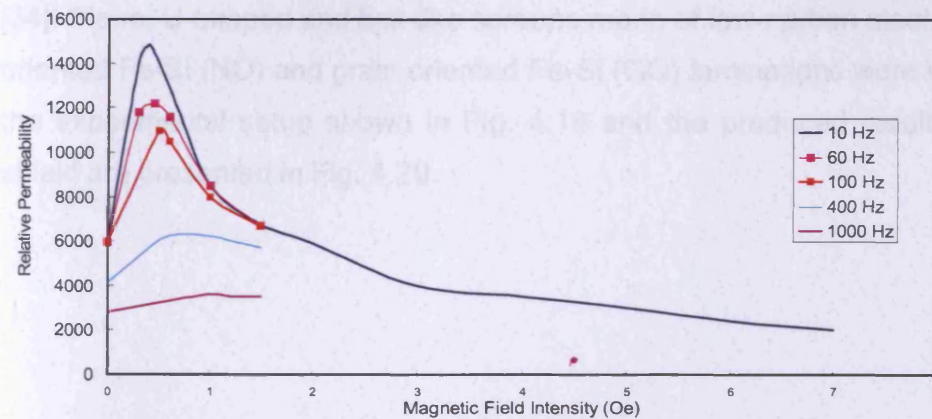
Chapter 4. Literature Review



(a)



(b)



(c)

Fig. 4.17. Magnetic permeability of the cylinders with various diameters
(a) 18 cm, (b) 22 cm, (c) 26 cm [39]

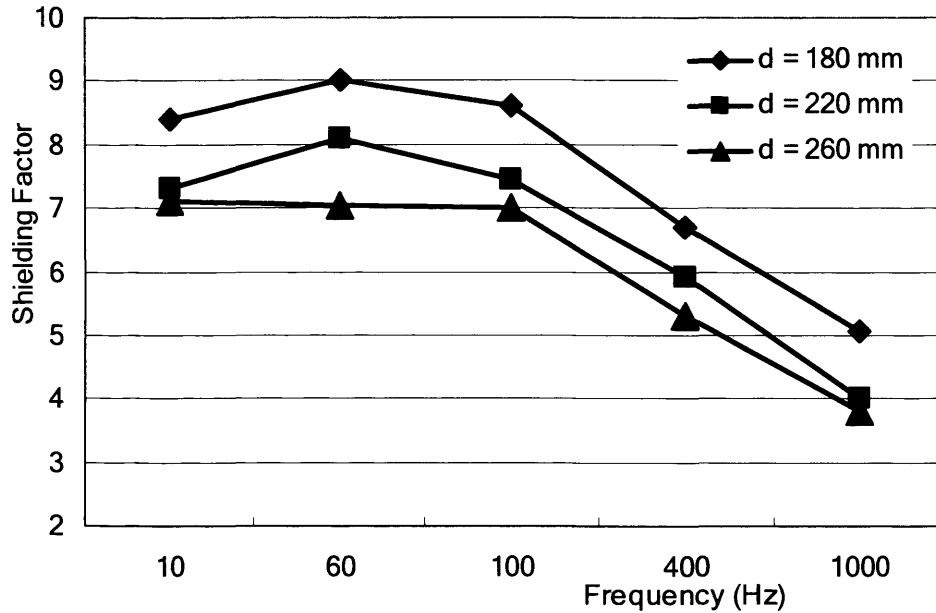
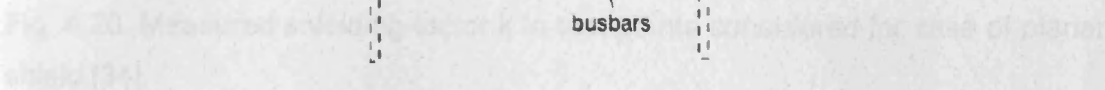


Fig. 4.18. Measured magnetic shielding factors for the single layered cylinders under the test condition of $H_o = 40 A/m$ and thickness is 0.29 mm [39]

Bottausico et. al. investigated the shielding efficiency of low-cost soft magnetic materials which can be employed in environmental magnetic field shielding as a competitive solution to high permeability alloys, such as mumetal and permalloy [34]. Plane, U-shaped and box-like screens made of low-carbon steel (LCS), non-oriented Fe-Si (NO) and grain oriented Fe-Si (GO) laminations were measured in the experimental setup shown in Fig. 4.19 and the produced results for planar shield are presented in Fig. 4.20.



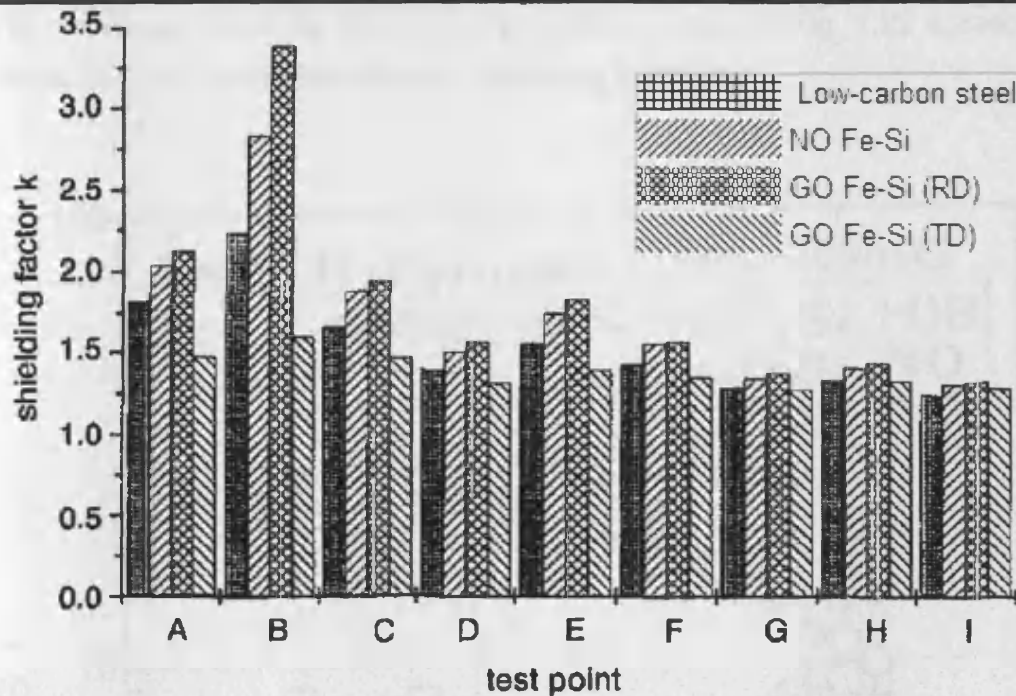


Fig. 4.20. Measured shielding factor k in test points considered for case of planar shield [34].

In 1992, Okazaki and Ueno investigated magnetic shielding effects of cylinders made of 3% Si steels sheets and amorphous ribbons [41]. Three 3% Si steels sheets were selected, 0.3 mm thick oriented, 0.35 mm thick double oriented and 0.5 mm non-oriented. They were formed into cylindrical shields 100 mm in diameter and 200 mm in length. Cylinders of 1- layer and 6 - layers Fe_{80.5}(si, B) 19.5 amorphous ribbon (AM) of 60 mm diameter and 150 mm long were also prepared. The easy axis of magnetization of 0.3 mm oriented steel was set in either the radial or axial direction. In the double oriented cylinder, the easy axis were set to both radial and axial directions. The cylinder with amorphous ribbons had its easy magnetizing axis in the radial direction.

The field was measured by a pick-up coil under a parallel external field, of 0.8 - 24 A/m at 50 - 20 kHz. The shielding factors were measured as the cylinder was setup in the transverse direction to the magnetic field. The measurement results are presented in Fig. 4.21 for the 3% Si steel and Fig. 4.22 for amorphous ribbon.

The measured shielding factor of grain-oriented steel in Fig. 4.22 agreed with Mayer [17] as it decreases with the increasing frequency.

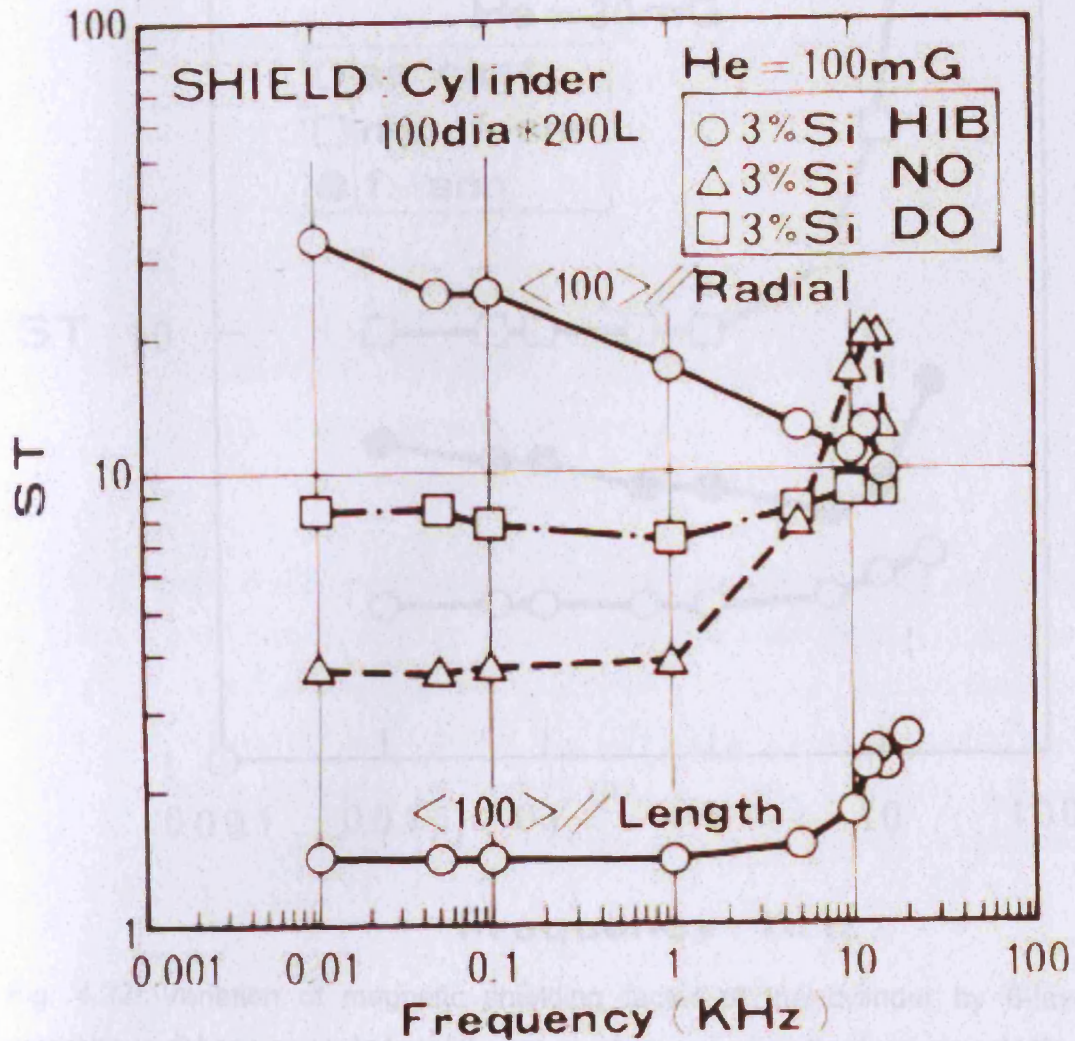


Fig. 4.21. Variations of measured magnetic shielding factors of cylinders made of 3% Si steels against the frequency, HIB: 0.3 mm grain oriented steel, DO: 0.35 mm double oriented steel, NO: 0.5 mm non-oriented steel [41].

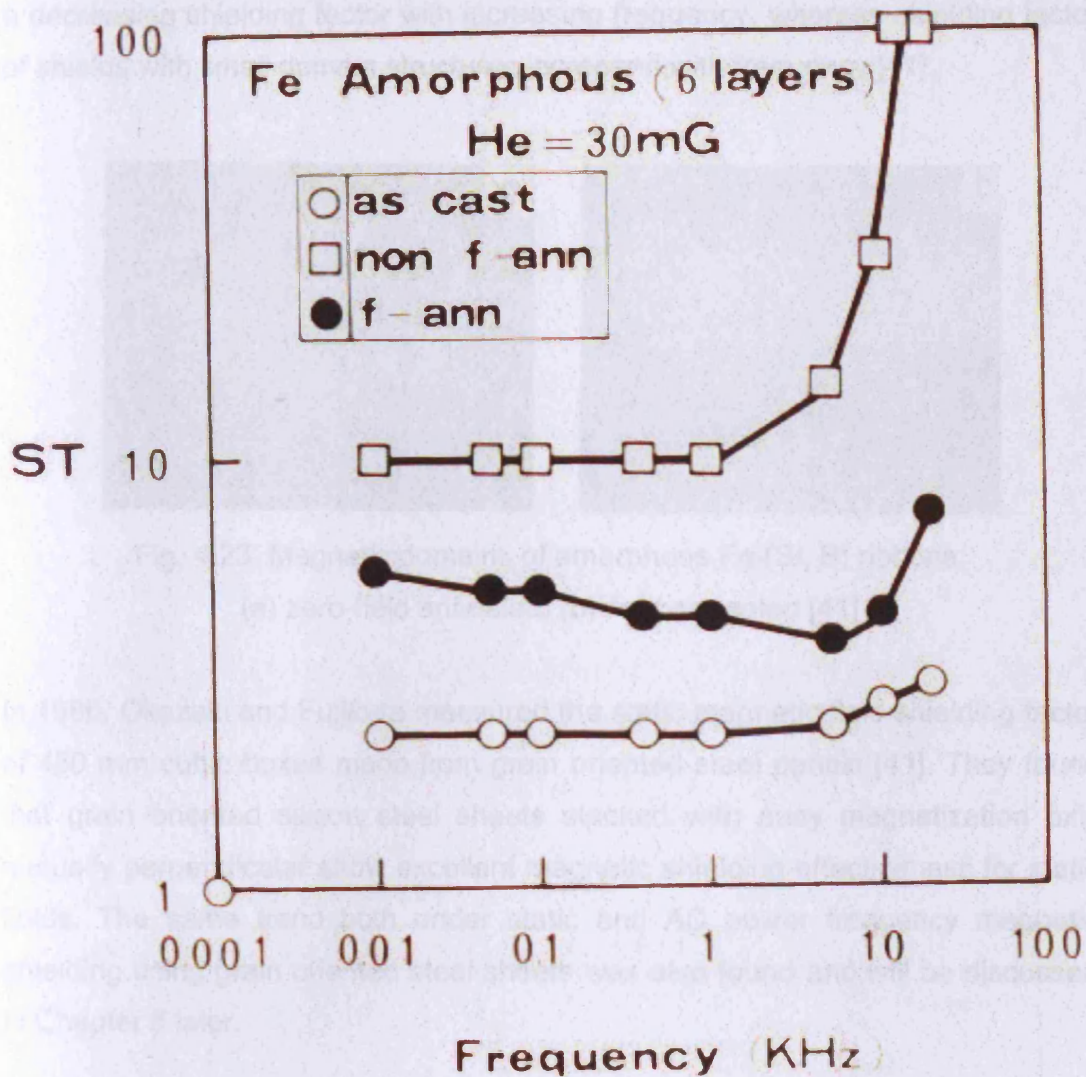


Fig. 4.22. Variation of magnetic shielding factor of the cylinder by 6-layer amorphous ribbons annealed at different conditions against the frequency [41].

Domain observation was also carried out [41]. The HIB and field-annealed amorphous Fe sheets had parallel 180° domains with large spacing of about 0.5 - 1 mm for HIB and 2 - 3 mm for amorphous Fe. The NO and zero-field-annealed amorphous Fe showed small and non-uniaxial 180° domains. Domain structures of the amorphous Fe annealed under different field conditions can be found in Fig. 4.23. To correlate the findings from the domain structure with the shielding

factors, it was found that shields with large and straight 180 degree domains had a decreasing shielding factor with increasing frequency, whereas shielding factor of shields with small domain structures increased with frequency [41].

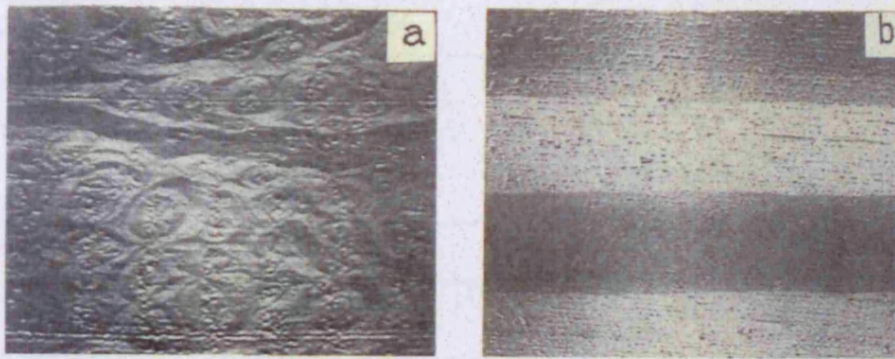


Fig. 4.23. Magnetic domains of amorphous Fe (Si, B) ribbons:
(a) zero-field annealed, (b) field annealed [41]

In 1996, Okazaki and Fujikura measured the static magnetic field shielding factor of 450 mm cubic boxes made from grain oriented steel panels [41]. They found that grain oriented silicon steel sheets stacked with easy magnetization axis mutually perpendicular show excellent magnetic shielding effectiveness for static fields. The same trend both under static and AC power frequency magnetic shielding using grain oriented steel sheets was also found and will be discussed in Chapter 6 later.

In Okazaki's latest work on magnetic shielding in 2005 [41], shielding effectiveness of soft magnetic materials in the form of stacked 450 mm square sheets were measured under AC excitation with a 1.82 m square Merritt-type coil [43]. His material selections included grain oriented, non-oriented electrical steels, 78 Ni Permalloy, amorphous ribbons (Fe or Co based) and non-magnetic metals as listed in Fig. 4.24.

Chapter 4. Literature Review

Table 1 Shielding materials for the experiments

Material	Thickness (mm)	Stack (Sheet)	μ_{\max} (H/m)	Bs (T)	ρ ($\mu\Omega\text{cm}$)	
Grain Oriented Si-steel(GO)	0.35	1-6	0.07	2	48	
Non Oriented Si-steel(NO-H)	0.35	1-6	0.01	2	54	
Non Oriented Si-steel(NO-M)	0.50	1-4	0.007	2	32	
78Ni Permalloy (PC)	1.0, 2.0	1	0.2	0.7	57	
Fe-Si-B amorphous(AM-Fe)	0.025	1-80	0.012	1.5	130	as cast
Co-Ni-Si-B ditto (AM-Co)	0.020	1-100	0.03	0.7	125	as cast
Fe-Si-B flake (AM-F)	Flake	-	-	-	-	flake
Fe-Nb-Cu-Si-B nano(Nano)	0.020	1-4	0.09	1.2	120	annealed
Copper (Cu)	0.5	1-4				
Aluminum(Al)	0.5	1-4				

Fig. 4.24. Materials selection for the magnetic shielding effectiveness test [42]

The variation of the measured shielding effectiveness at 50Hz and 10 μT with the stacked thickness is shown in Fig. 4.25 and also the shielding effectiveness vs. frequency at 10 μT and 1 mm thick in Fig. 4.26.

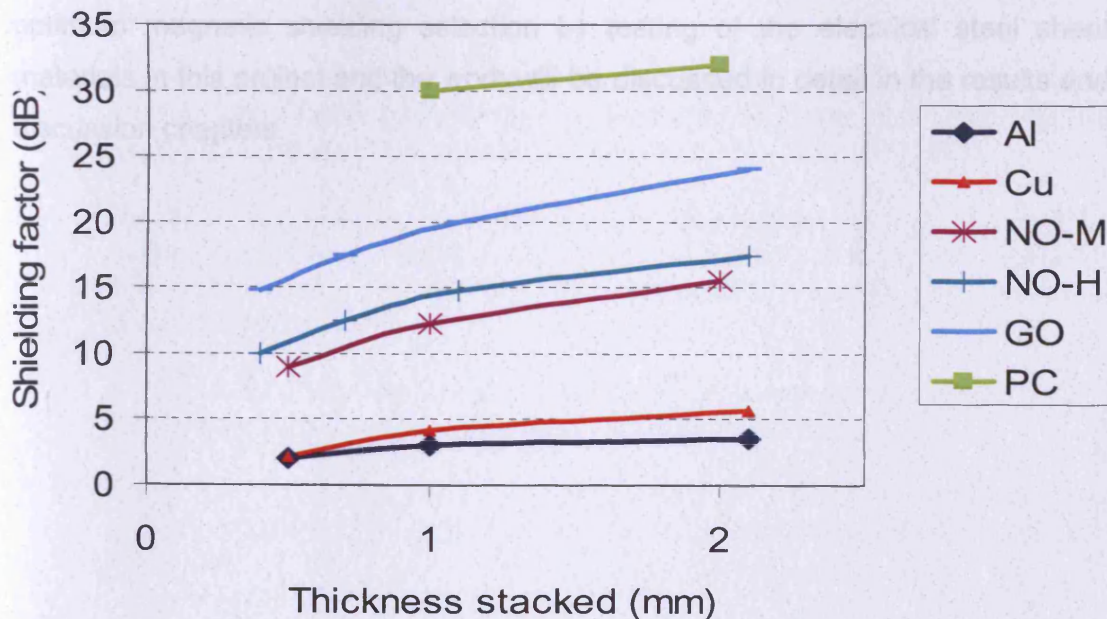


Fig. 4.25. Shielding effectiveness vs. stacked thickness, at 50 Hz, 10 μT [42].

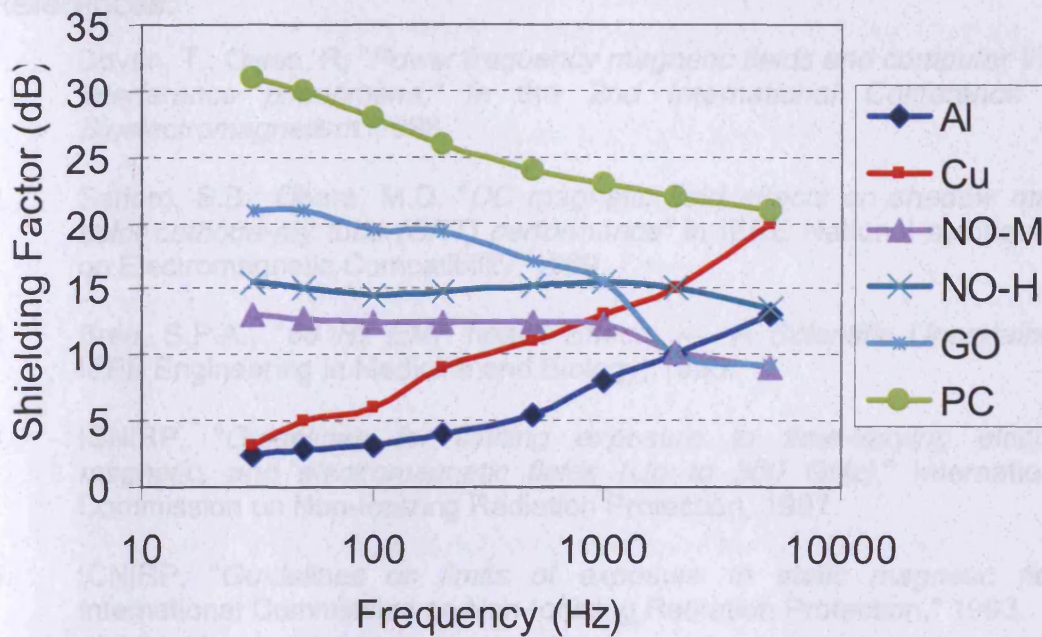


Fig. 4.26. Shielding effectiveness vs. frequency, 10 μ T and 1 mm thickness [42].

The results above are from materials with various magnetic and electrical properties by Okazaki and Fujwara. It clarified optimum selection practice of extremely low frequency magnetic shielding. More effort has been put on the optimum magnetic shielding selection by testing of the electrical steel sheet materials in this project and the work will be discussed in detail in the results and discussion chapters.

References:

1. Dovan, T.; Owen, R. "*Power frequency magnetic fields and computer VDU interference phenomena*," in the *2nd International Conference on Bioelectromagnetism*. 1998.
2. Safford, S.B.; Obara, M.D. "*DC magnetic field effects on shadow mask color cathode-ray tube (CRT) performance*" in IEEE National symposium on Electromagnetic Compatibility, 1989.
3. Bren, S.P.A., "*60 Hz EMF health Effects ---- A Scientific Uncertainty*," IEEE Engineering in Medicine and Biology, 1995.
4. ICNIRP, "*Guidelines for limiting exposure to time-varying electric, magnetic, and electromagnetic fields (Up to 300 GHz)*," International Commission on Non-Ionizing Radiation Protection, 1997.
5. ICNIRP, "*Guidelines on limits of exposure to static magnetic field*," International Commission on Non-Ionizing Radiation Protection," 1993.
6. Buccella, C.; Feliziani, M.; Fuina, V. "*ELF magnetic field mitigation by active shielding*," Proceedings of the IEEE International symposium on Industrial Electronics, 2002.
7. Platzek, D.; Nowak, H.; Giessler, F.; Rother, J.; "*Active shielding to reduce low frequency disturbances in direct current near biomagnetic measurements*," Review of Scientific Instruments, Volume 70, Issue 5, pp.2465-2470, 1999.
8. Buccella, C.; Feliziani, M.; Prudenzi, A.; "*Active shielding design for a MV/LV distribution transformer substation*," in the 3rd International Symposium on Electromagnetic Compatibility. pp. 350-353, 2002.
9. Sergeant, P. L.; Dupre, L. R.; De Wulf, M.; Melkebeek, J. A. A. "*Optimizing active and passive magnetic shields in induction heating by a genetic algorithm*," IEEE Transactions on Magnetics, Volume: 39, Issue: 6, pp.3486-3496, 2003.
10. Rucker, A.W., "*On the magnetic shielding of concentric spherical shells*," Proc. Phys. Soc. London Volume:12, pp.462-501, 1892.
11. Wills, A.P. "*The magnetic shielding effect of trilamellar spherical and cylindrical shells*," Physical Review (series I), Volume: 9, Issue: 4, pp.193-213, 1899.

Chapter 4. Literature Review

12. Thomas, A.K. "*Magnetic shielded enclosure design in the DC and VLF region*," IEEE Transactions on Electromagnetic Compatibility, Volume: 10, Issue: 1, pp. 142-152, 1968.
13. Jackson, J.D. *Classical Electrodynamics*, New York, Wiley, 1962.
14. King, L.V. "*Electromagnetic shielding at Radio frequencies*," Phil. Mag. Volume: 15, pp. 201-223.
15. Schweizer, F. "*Magnetic shielding factors of a system of concentric spherical shells*," Journal of Applied Physics, Volume: 33, pp.1001-1003, 1962.
16. Patton, B.J. "*Room size enclosure for geomagnetic shielding*," IEEE Electromagnetic Compatibility Symp. Rec., pp. 89-96, 1970.
17. Mager, A.J. "*Magnetic Shields*," IEEE Transactions on Magnetics, Volume: 6, pp. 67-75, 1970.
18. Schelkunoff, S.A. *Electromagnetic Waves*. New York, D. Van Nostrand Company, 1943.
19. Adams, W. S. "*Electromagnetic shielding in the near field*," IEEE Electromagnetic Compatibility Symp. Rec. pp. 317-329, 1968.
20. Cowdell, R.B., "*Magnetic shielding made attractive*," IEEE Electromagnetic Compatibility Symp. Rec., pp. 58-67, 1971.
21. Greifinger, C.; Greifinger, P. S.; Hart, L. W. "*Shielding of ELF magnetic-dipole fields by ferromagnetic cylindrical shells*," IEEE Transactions on Electromagnetic Compatibility, Volume: 23, Issue: 1, pp. 2-12, 1981.
22. Moser, J.R., "*Low-frequency Low-impedance Electromagnetic Shielding*," IEEE Transactions on Electromagnetic Compatibility, Volume: 30, Issue: 3, pp. 202-209, 1988.
23. Wheeler, H. "*The spherical coil as inductor, shield, or antenna*," Proc. IRE, pp. 1595-1602, 1958.
24. Miedzinski, J. "*Electromagnetic screening theory and practice*," British Electrical and Allied Research Association, Technical Report. MIT 135, 1959.
25. Miller, D. A.; Bridges, J. E. "*Geometrical effects on shielding effectiveness at low frequencies*," IEEE Transactions on Electromagnetic Compatibility, Volume: 8, Issue: 4, pp. 174-185, 1966.

Chapter 4. Literature Review

-
26. Miller, D. A.; Bridges, J. E. "*Review of circuit approach to calculate shielding Effectiveness*," IEEE Transactions on Electromagnetic Compatibility, Volume: 10, Issue: 1, pp. 52-62, 1968.
 27. Bridges, J. E. "*An update on the circuit approach to calculate shielding effectiveness*," IEEE Transactions on Electromagnetic Compatibility, Volume: 30, Issue: 3, pp.211-221, 1988.
 28. Frix, W. M.; Karady, G. G. "*A circuital approach to estimate the magnetic field reduction of nonferrous metal shields*," IEEE Transactions on Electromagnetic Compatibility, Volume: 39, Issue: 1, pp.24-32, 1997.
 29. Hoburg, J. F. "*Principles of Quasi-static magnetic shielding with cylindrical and spherical shields*," IEEE Transactions on Electromagnetic Compatibility, Volume: 37, Issue: 4, pp.574-579, 1995.
 30. Hasselgren, L.; Luomi, J. "*Geometrical aspects of magnetic shielding at extremely low frequencies*" IEEE Transactions on Electromagnetic Compatibility, Volume: 37, Issue: 3, pp: 409-420, 1995.
 31. Du, Y.; Cheng, T. C.; Farag, A. S. "*Principles of power frequency magnetic field shielding with flat sheets in a source of long conductors*," IEEE Transactions on Electromagnetic Compatibility, Volume: 38, Issue: 3, pp: 450-459, 1996.
 32. Du, Y.; Burnett, J. "*Power-frequency magnetic shielding of heavy-current conductors by rectangular shields*," IEE Proceedings - Generation, Transmission and Distribution, Volume: 146, Issue: 3, pp 223-228, 1999.
 33. Du, Y.; Burnett, J. "*Magnetic shielding principles of linear cylindrical shield at power frequency*." IEEE International Symposium on Electromagnetic Compatibility, pp. 488-493, 1996.
 34. Bottauscio, O.; Chiampi, D.; Chiarabaglio, D.; Fiorillo, F. Rocchino, L.; Zucca, M. "*Role of magnetic materials in power frequency shielding: numerical analysis and experiments*," IEE proceedings - Generation, Transmission and Distribution, Volume: 148, Issue: 2, pp. 104-110, 2001.
 35. Araneo, R.; Celozzi, S. "*Analysis of the shielding performance of ferromagnetic screens*," IEEE Transactions on Magnetics, Volume: 39, Issue: 2, pp. 1046-1052, 2003.
 36. Jiles, D. C.; Atherton, D, L. "*Ferromagnetic Hysteresis*," IEEE Transactions on Magnetics, Volume: 19, pp. 2183-2185, 1983.
-

Chapter 4. Literature Review

-
37. U.S. Government, "*MIL-STD-285, Attenuation measurements for enclosures, electromagnetic shielding, for electronic test purposes, method of.*" U.S. Government, 1954.
 38. IEEE, "*IEEE STD 299 - shielding enclosures, electromagnetic, for electronic test purposes, method for measuring the effectiveness of.*" IEEE, 1985.
 39. Chung, Y.; Woo, B.; Park, D.; "*Shielding factors of grain oriented 3% SiFe cylinders,*" IEEE Transactions on Magnetics, Volume: 35, Issue: 5, pp. 3454-3456, 1999.
 40. ASTM, "*ASTM 698/A698M-02, Standard test method for magnetic shield efficiency in attenuating alternating magnetic fields,*" American Society of Testing Materials, 2002
 41. Okazaki, Y.; Uedo, K., "*Magnetic shielding by soft magnetic materials in alternating magnetic field,*" Journal of Magnetism and Magnetic Materials, Volume: 112, pp. 192-194, 1992.
 42. Okazaki, Y.; Fujirawa, M., "*Magnetic shielding by grain oriented silicon steel composite panels,*" Studies in Applied electromagnetic and mechanics 10: Nonlinear Electromagnetic systems, pp. 644-647, 1996.
 43. Merritt, R.; Purcell, C.; Stroink, G., "*Uniform magnetic field produced by three, four, and five square coils.*" Rev. Sci. Instrum. Vol: 54, pp. 879-882, 1983.

Chapter Five.

System development

5.1 Introduction

Previous test methods[1-3] have been developed to measure the magnetic shielding factors at low frequencies. Different test methods can meet certain requirements. For example, the shielding factor measured by the ASTM A698/A698M [3] is the shielding factor of a component as cylindrical or box-type shields. The new test method developed in this chapter is to provide electrical steel manufacturers with a convenient way to assess magnetic shielding factor of electrical steel panels under static and extremely low frequency magnetic field conditions. The measured shielding factor is representative of the shielding effectiveness of the material.

The following aspects should be taken into account when designing an appropriate test method for shielding factor measurement:

1. It should simulate the right electromagnetic phenomenon to produce meaningful data for practical work.
2. It should be convenient to prepare the test and samples.
3. It should have an acceptable repeatability.

In the following sections the test procedures and definition of shielding factor in the new method are introduced. Different components used for measurements at 50 Hz are presented and discussed. The measurement under DC condition is based on the same procedure but with a DC magnetic field excitation. The difference between DC and 50 Hz measurements is covered later in this chapter.

5.2 Outline of the test setup and Shielding factor definition

This method is based on the measurement of the attenuation or insertion loss by the placement of the shielding material between the transmitter and receiver. The block diagram in Fig. 5.1 presents the basic structure of the setup.

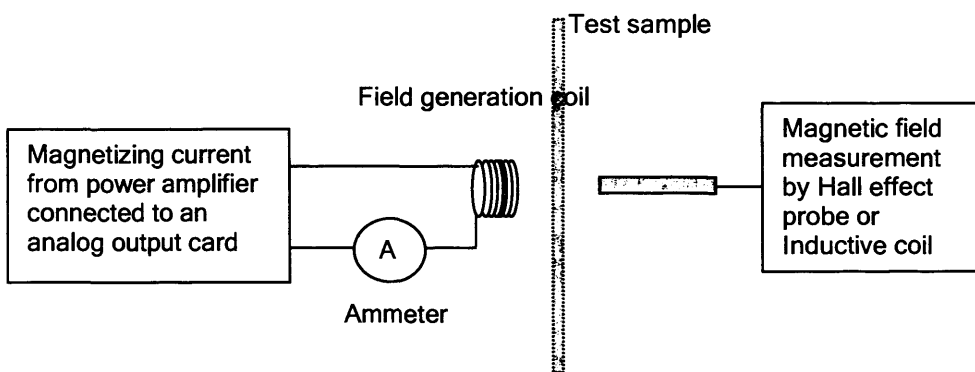


Fig. 5.1. Block diagram of the measurement setup

Fig. 5.2 shows that a 120-turn solenoid is located inside a 450 mm diameter, 300 mm high cylinder of two layers laminated from non-oriented electrical steel sheets. The solenoid is connected to the output of the power amplifier, which is driven by a sinusoidal voltage signal generated from an analog output card. The 500 mm square steel panel can be placed on top of the cylinder to shield the magnetic field generated by the solenoid. The magnetic field strength above the panel and solenoid as shown in Fig. 5.2 can be measured by either a transverse Hall effect probe with a Gaussmeter or an inductive sensing coil in the case of without the panel or the panel in place.

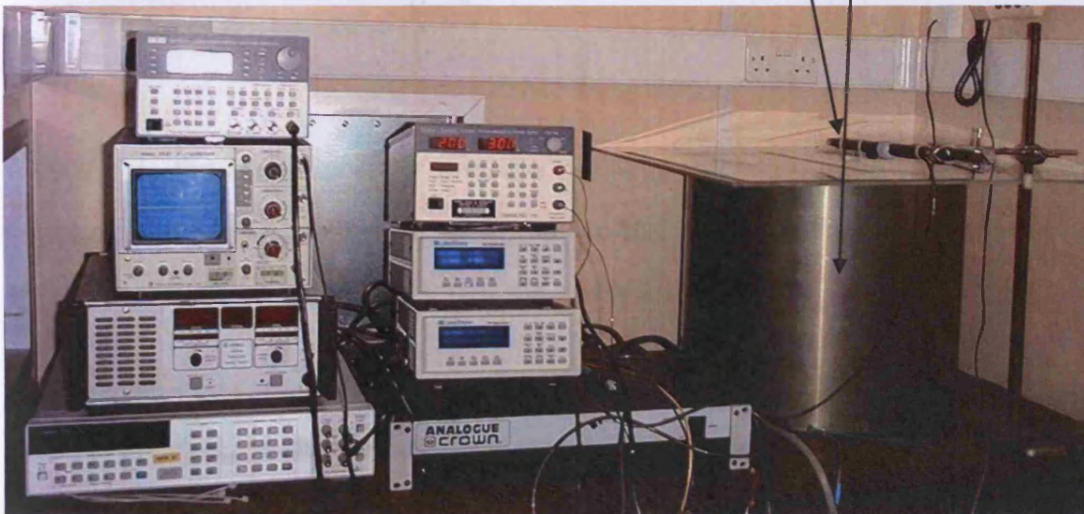
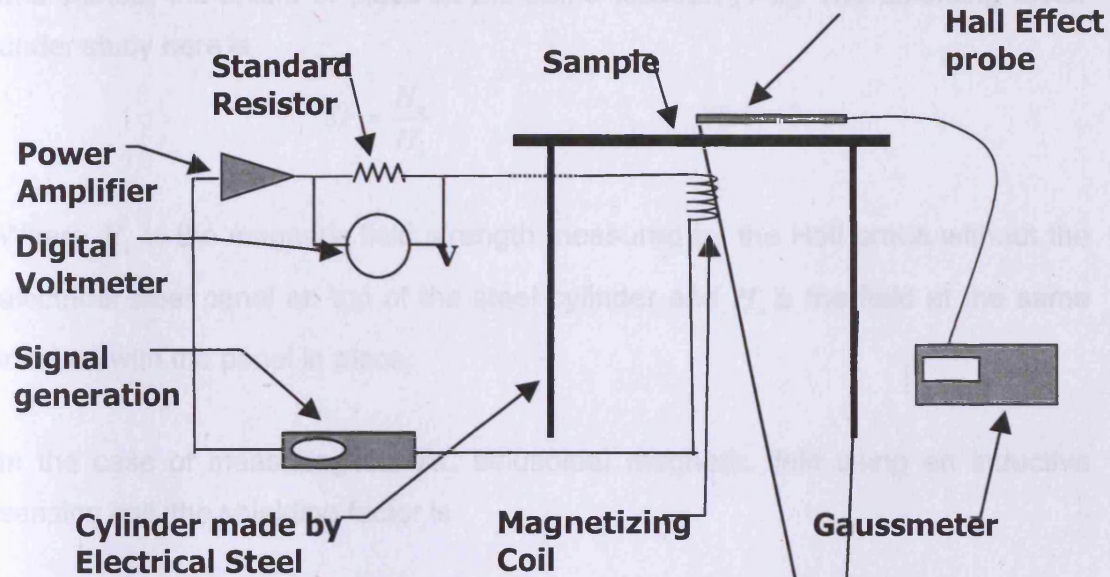


Fig. 5.2. Block diagram and practical laboratory setup

Chapter 5. System Development

The shielding factor or effectiveness is defined as a ratio between the field with and without the shield in place at the same location [1-5]. The shielding factor under study here is

$$SF = \frac{H_o}{H_s} \quad (5.1)$$

Where H_o is the magnetic field strength measured by the Hall probe without the electrical steel panel on top of the steel cylinder and H_s is the field at the same location with the panel in place.

In the case of measuring the AC sinusoidal magnetic field using an inductive sensing coil, the shielding factor is

$$SF = \frac{\int V_o dt}{\int V_s dt} \quad (5.2)$$

Where V_o is the output voltage from the sensing coil without the electrical steel panel on top of the steel cylinder and V_s is the output voltage from the same sensing coil with the panel in place at the same location.

The shielding factor is plotted against the applied magnetic field generated by the magnetizing coil. As the applied field at a specific location is determined by the excitation current for the same coil, the applied field strength at the location marked on Fig. 5.3 can be used to replace the excitation current in the measurement of the shielding factors. The reference location is on the axis of the excitation coil and the cylinder, also at the sample's underside surface, which is the incident surface for magnetic field from the excitation coil. The use of the reference field can provide guidelines for the optimum material selections for particular environment field conditions. The effect of the cylinder on the field pattern is negligible because the diameter of excitation coil is less than 1/10 of the diameter of the cylinder, therefore the Gaussmeter can measure the

reference field during a sweep of the excitation current while the sample is not in place.

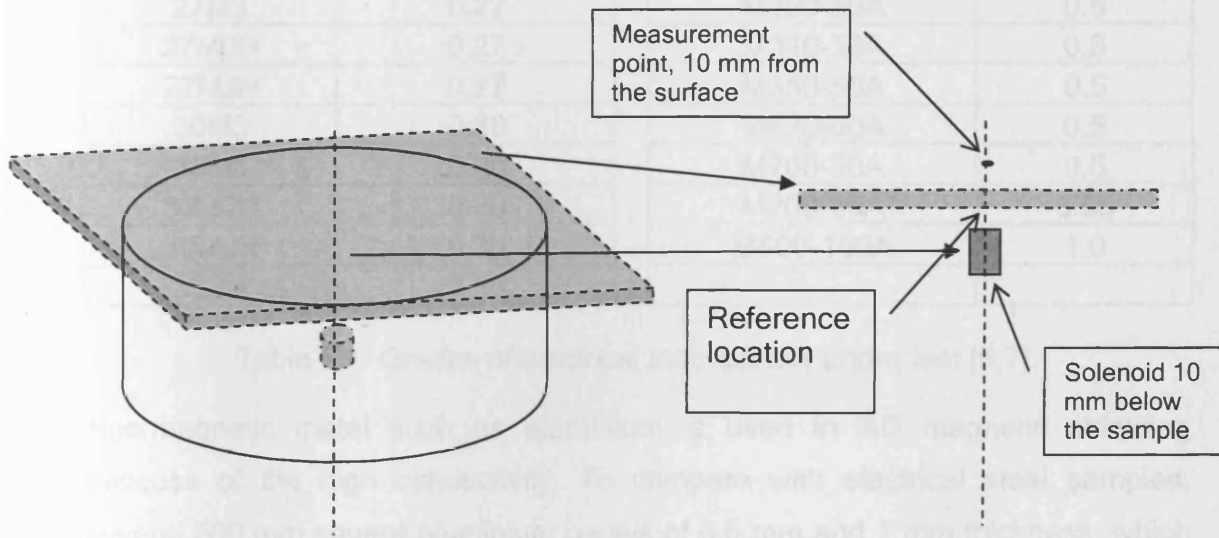


Fig. 5.3. Applied field measured at the reference location when the sample is not in place

5.3. Samples

A variety of grain-oriented and non-oriented electrical steels were tested for the magnetic shielding factor. Samples of two shapes were prepared from the same grade of electrical steel, 500 mm by 500 mm panels to test the shielding factor and 30 mm by 305 mm standard Epstein strip for magnetic characterization.

The grades and thickness of the samples under test are listed as in Table.5.1.

Grain Oriented Grades	Thickness (mm)		Non-Oriented Grades	Thickness (mm)
27M3	0.27		M290-50A	0.5
27M0H	0.27		M310-50A	0.5
27MJH	0.27		M350-50A	0.5
30M3	0.30		M470-50A	0.5
30M4	0.30		M700-50A	0.5
30M0H	0.30		M700-65A	0.65
30MJH	0.30		M800-100A	1.0
35M4	0.35			

Table 5.1. Grades of electrical steel panels under test [6,7].

Non-magnetic metal such as aluminium is used in AC magnetic shielding because of the high conductivity. To compare with electrical steel samples, several 500 mm square aluminium panels of 0.5 mm and 1 mm thickness, which can be stacked into different thickness, were also prepared for AC magnetic shielding factor test.

5.4. Magnetic field generation

A solenoid with dimensions shown in Fig. 5.4 was employed as the excitation coil to generate the magnetic field. The solenoid is small compared to the 500 mm square panel in order to simulate the measurement of an infinite size sample. The small solenoid can also reduce the magnetic coupling between the solenoid and the cylinder, which is discussed later in section 5.4. The soft magnetic core can be used to amplify the generated magnetic flux, however this is not preferred due to the non-linear distortion caused by the non-linear B-H properties of the core material.

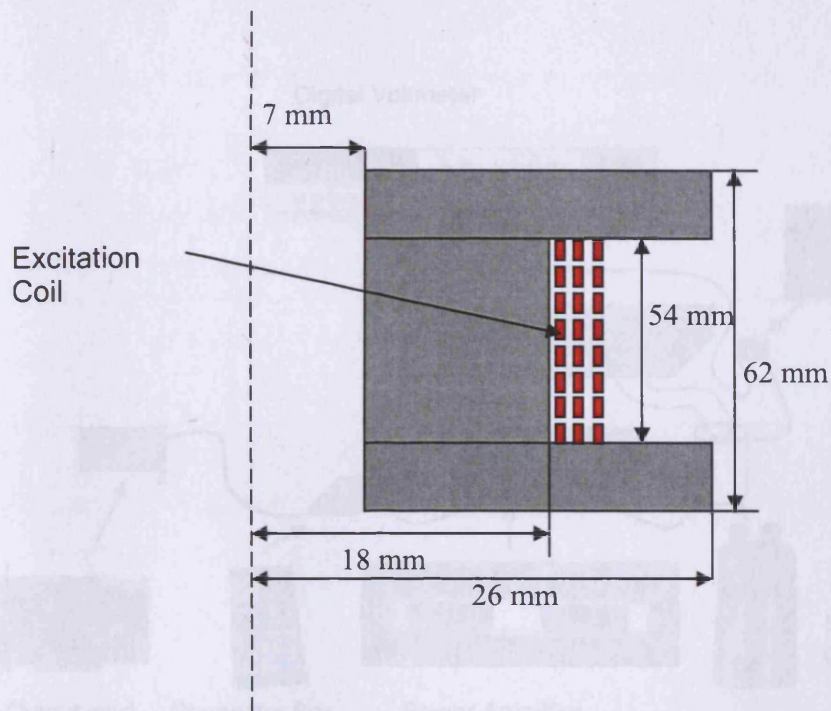


Fig. 5.4. Dimension of the excitation coil (half of the cross-sectional view). 3 layers, 120 turns with 1 mm diameter copper wire. Capable of generating 1800 A/m applied field at the reference location.

The magnetizing circuit, which was used to generate AC magnetic fields, is shown in Fig. 5.5. The sinusoidal voltage signal is generated by the NI PCI-6711 high-speed analog output with an update rate of 1MS/s. The signal was delivered via the NI BNC-2110 connector block to the Pioneer power amplifier. The magnetizing current was monitored by measuring the voltage across a 0.02-ohm standard resistor in series connection in the circuit. Specifications of the instruments used are given in Table 5.2.

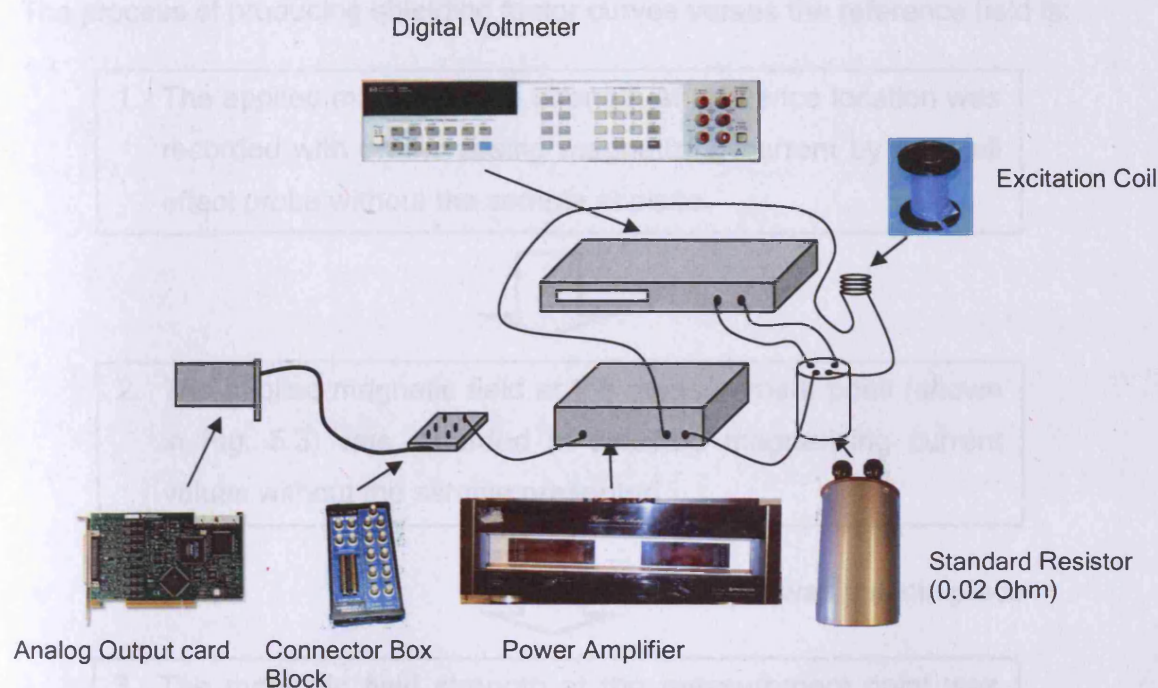


Fig. 5.5. Circuits to generate time varying magnetic fields

Equipment	Model number	Remarks
Analog output card	NI PCI-6711	High speed analog output - 12- bit, 1 MS/s per channel
Connector box block	NI BNC-2110	Shielded enclosure terminal block with BNC connector for analog I/O
Standard resistor	Type RS2	CROPICO Resistance Standard, 0.02 ohm with the current limit of 50 Amp with oil cooling, +/- 0.01%
Voltmeter	HP 3458A	HP digital multimeter, programmable with GPIB, used as Digital voltmeter in the system
Power Amplifier	Pioneer M-90a	Reference stereo power amplifier, working frequency band is between 20 Hz and 20 KHz, 1000 watt, ideal impedance of load is between 4 to 8 ohm

Table 5.2. Specifications of the instruments used in the field generation.

The process of producing shielding factor curves verses the reference field is:

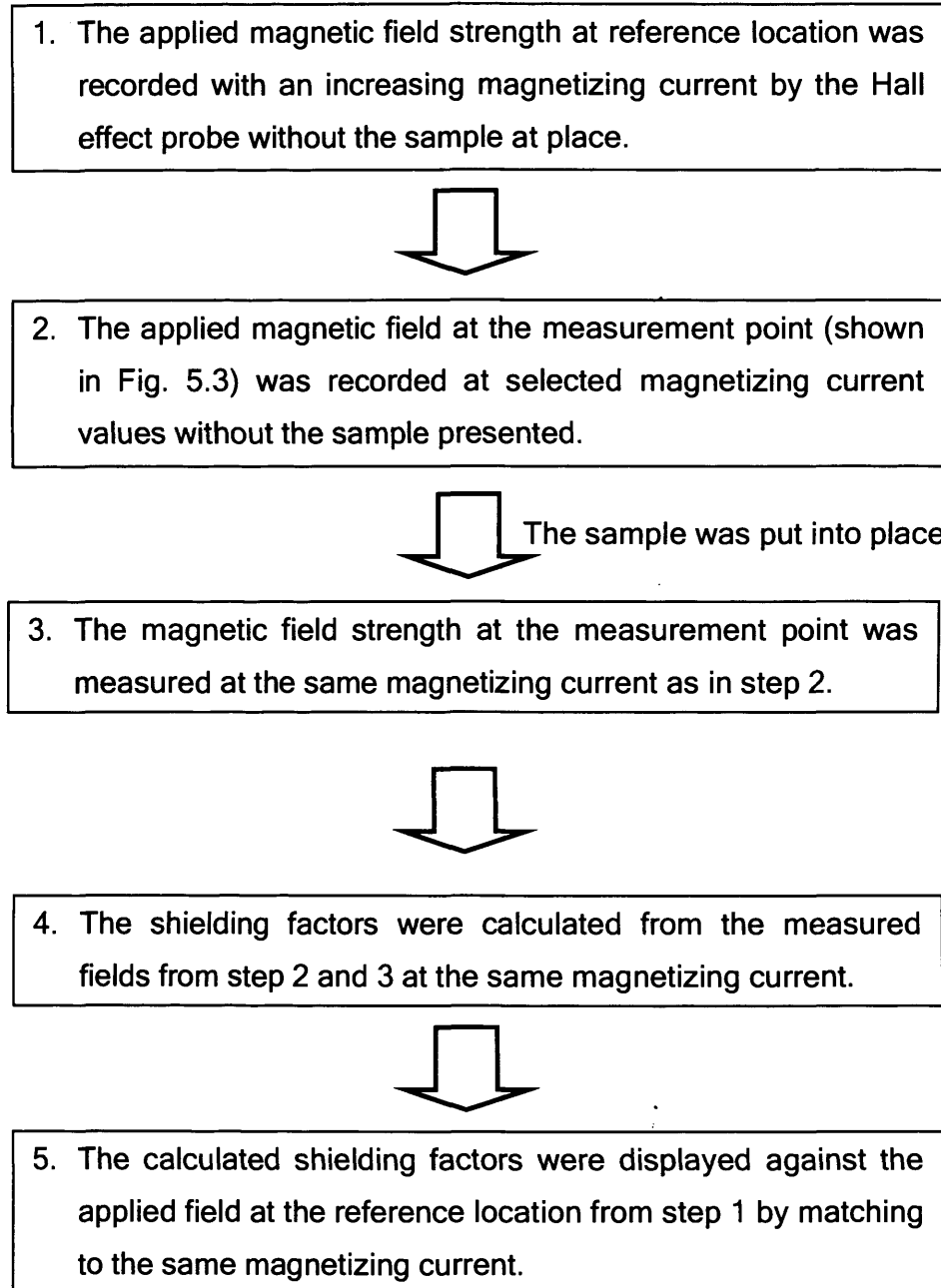


Fig. 5.6. Flowchart of the shielding factor measurement

Chapter 5. System Development

With GPIB[8] support from the instruments, automation of the measurement procedure above was implemented. National Instruments LabVIEW[9], which is a powerful graphical development environment for signal acquisition and measurement analysis, was used to realize the measurement automation. The block diagram in Fig. 5.7 shows how the program works. This is a dynamic procedure, which is automatically controlled in LabVIEW. It starts with zero magnetizing current and then increases the output of PCI-6711 in steps of 1 mv. At each step, the voltmeter measures the voltage, which determines if the current has reached the desired magnetizing level. The LabVIEW program then takes the field reading from the Gaussmeter or the voltmeter. In this way, the measurements of the field strength at steps 1, 2 and 3 are maintained to the same level to provide a possible calculation of the shielding factor at this magnetization level.

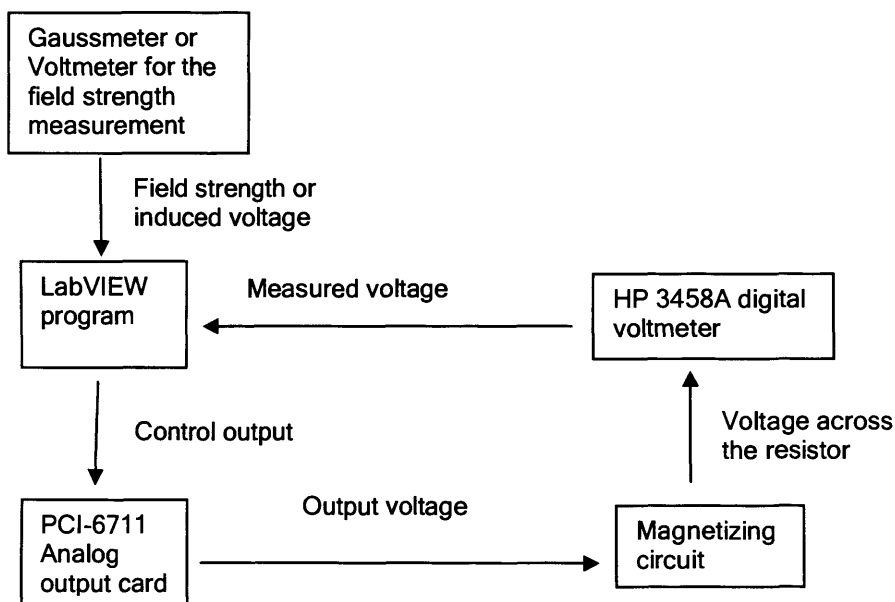


Fig. 5.7. Block diagram of the LabVIEW programmed for measurement automation

5.5. Electrical steel cylinder in the test setup

The flux generated from the solenoid is diverted along the sample, then finally returns to the solenoid, although the 500 by 500 mm sample is much larger than the solenoid, there is still flux leakage from the edge of the sample reaching the other side where the field strength is measured. The shielding factor measures the ability of the sample to divert the flux, therefore the flux leakage from the edge should be eliminated. The cylinder in the system is to simulate a sample of infinite size. The ideal way of material assessment is the test of the material itself by reducing the other factors rather than the material properties.

The electrical steel cylinder in the test system provides a path for the flux, which is ducted by the shield to return to the magnetizing solenoid. The cylinder has a diameter of 450 mm, height of 300 mm and is rolled from 0.5 mm thick non-oriented electrical steel M350-50A. The joint is made by spot welding to minimize the degradation of the magnetic property.

To investigate how different cylinders affect the measured shielding factor, finite element modelling and measurements with cylinders of various sizes and different grades of electrical steels were carried out. Fig. 5.8 shows the model in the commercial FEM package Vectorfields Opera 2D. Only half of the cross section was modelled because of the axis symmetrical geometry.

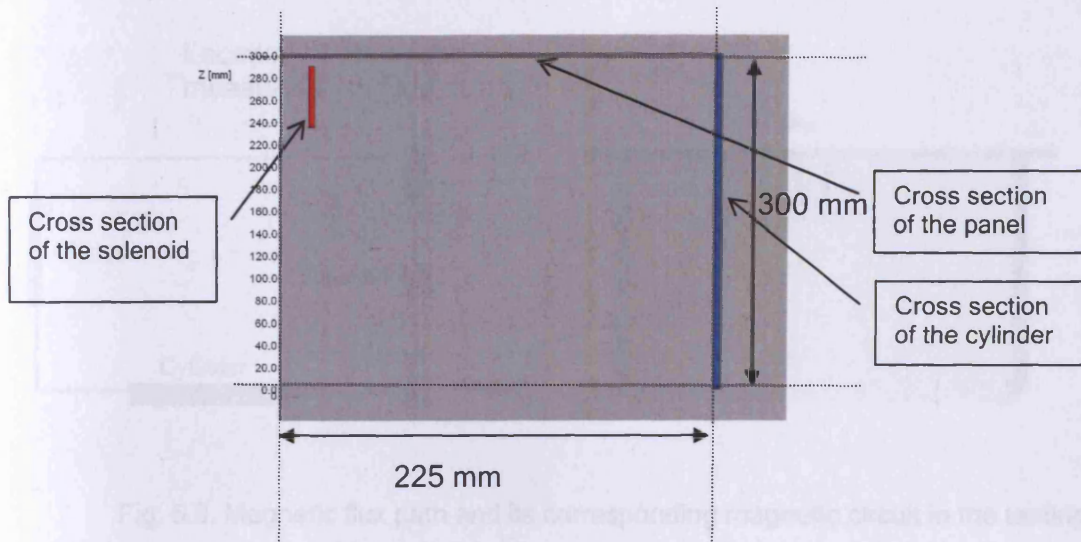


Fig. 5.8. Geometry of the model in Opera 2D (cylinder dimensions: 450 mm diameter, 300 mm high)

Most of the magnetic flux generated from the solenoid goes through the air gap between the solenoid and the sample panel, turns into the panel and is ducted into the cylinder via the joint between the panel and the cylinder, finally it returns at the solenoid after travelling through another air gap between the cylinder and the solenoid. The corresponding magnetic circuit is shown in Fig. 5.9. The magnetic reluctance of the magnetic flux path is almost infinite because of the two air gaps. Compared with the air gaps, the reluctance of the cylinder can be neglected. As the generated magnetic potential is constant at the same magnetizing current in the coil, cylinders of different permeabilities do not make difference to magnetic reluctance of the magnetic circuit.

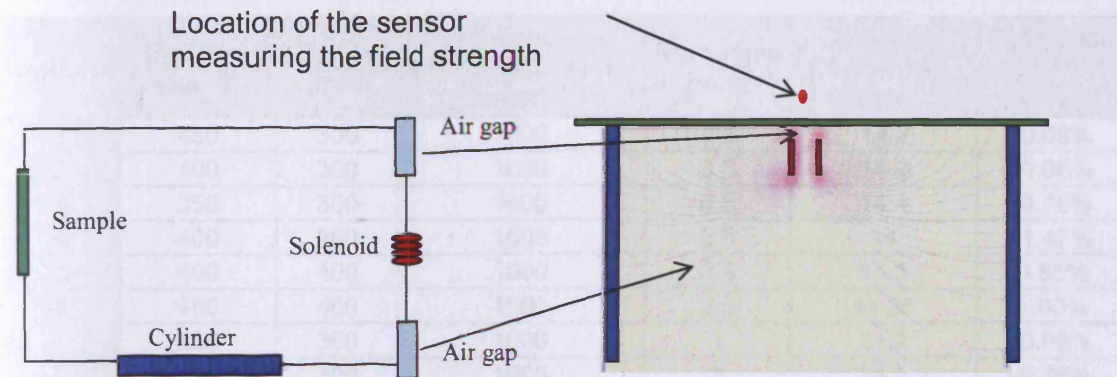


Fig. 5.9. Magnetic flux path and its corresponding magnetic circuit in the testing

Due to the high magnetic reluctance of the flux path and large demagnetizing effect of the sample (which will be discussed in detail in chapter 6), the magnetic materials including the sample and the cylinder are magnetized at less than 0.1 Tesla in which field range initial permeability applies. Cylinders of the same geometry (450 mm diameter and 300 mm high), but different initial permeabilities were modelled. Three cases were compared, one cylinder was made from material with initial relative permeability 500 and the other two with 1000 and 10000. The shielding factors are computed in these cases respectively and from Table. 5.3, it can be seen that cylinders of different relative initial permeabilities do not affect the computed shielding factor in the model. Also, cylinders of different dimensions were modelled and the computed DC shielding factors show that within the range, cylinders of different sizes do not affect the shielding factors.

Fig. 5.10. Three cylinders used for the investigation

These cylinders were made with the dimensions and specification shown in Fig. 5.10. These three cylinders varied in sizes and magnetic properties. The

Cylinder	Diameter (mm)	Height (mm)	Relative Permeability of the material	Thickness (mm)	Computed Shielding factor	Difference to the average
1	450	300	1000	0.5	14.2	-0.06%
2	400	300	1000	0.5	14.2	-0.06%
3	350	300	1000	0.5	14.1	-0.76%
4	400	200	1000	0.5	14	-1.47%
5	400	400	1000	0.5	14.3	0.65%
6	450	400	1000	0.5	14.35	1.00%
7	450	300	1000	1	14.2	-0.06%
8	450	300	1000	2	14.1	-0.76%
9	450	300	1000	3	14.15	-0.41%
10	450	300	500	0.5	14.3	0.65%
11	450	300	5000	0.5	14.3	0.65%
12	450	300	10000	0.5	14.3	0.65%

Table. 5.3. Computed static magnetic shielding factors of the same sample with cylinders of different size and materials

Cylinder	Material	Rolling direction	Number of laminations	Thickness (mm)	Joint	Size (Diameter by Height)
1	0.5mm thick M350-50A	N/A	1	0.5	Spot Welding	450 by 300
2	0.3mm thick 30M3	as shown below	4	1.2	Sticky tape	450 by 300
3	0.3mm thick 30M3	as shown below	10	3	Sticky tape	400 by 300

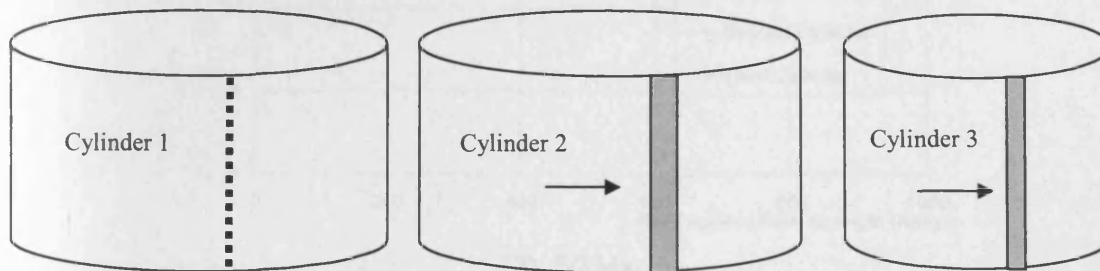
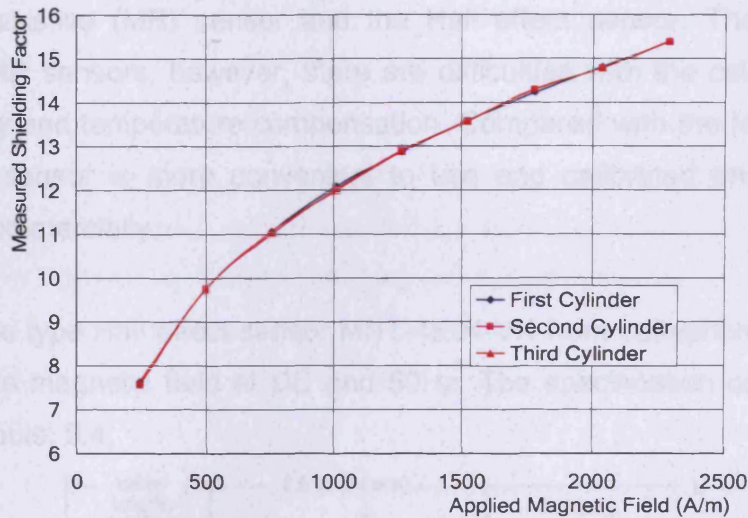


Fig. 5.10. Three cylinders used for the investigation

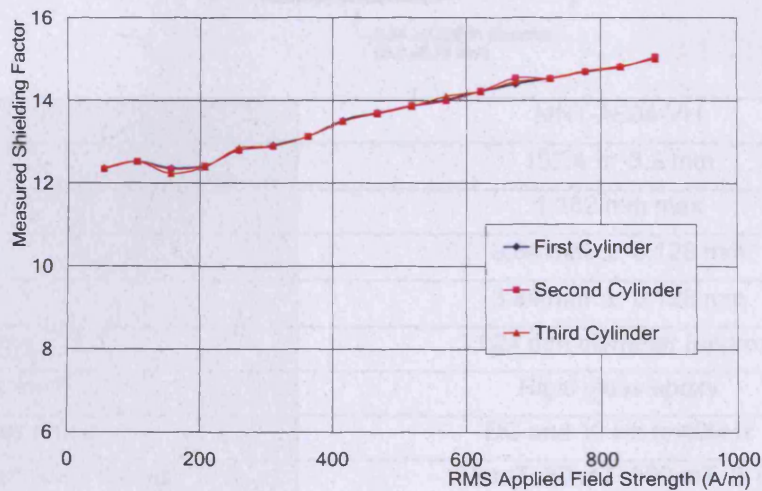
Three cylinders were made with the dimensions and specification shown in Fig. 5.10. These three cylinders varied in sizes and magnetic properties. The

Chapter 5. System Development

measured shielding factor curves of the 0.5 mm thick non-oriented sample M350-50A are presented in Fig. 5.11. These three curves are respectively from the setups with three different cylinders presented in Fig. 5.15. It can be seen that the results differ by less than 0.5%. Therefore, the effects of the cylinders of these three cases are negligible in the shielding factor measurements.



(1). DC



(2). 50 Hz

Fig. 5.11. The variation of the measured magnetic shielding factor of M350-50A with three cylinders presented in Fig.5.15 with the applied field strength, which is the reference field at the location shown in Fig. 5.3.

5.6. Measuring the magnetic field

Measurement of magnetic fields can be done by different sensors, such as the magnetic resistive (MR) sensor and the Hall effect sensor. There is a good variety of MR sensors, however, there are difficulties with the calibration of the non-linearity and temperature compensation. Compared with the MR sensor, the Hall effect sensor is more convenient to use and calibrated ones are widely available commercially.

A transverse type Hall effect sensor MNT-4E04-VH from Lakeshore was used to measure the magnetic field at DC and 50Hz. The specification of this probe is shown in Table. 5.4,



Probe	MNT-4E04-VH
L	102.4 ± 3.2 mm
T	1.152 mm max
W	3.84 mm ± 0.128 mm
A	3.84 mm ± 0.128 mm
Active area	1.024 mm diameter (approx)
Stem material	Rigid glass epoxy
Frequency range	DC and 10 Hz to 400Hz
Usable full scale ranges	3 mT, 30 mT, 300 mT, 3 T
Corrected accuracy (%rdg)	± 0.25% to 3 T
Operating temp range	0°C to +75 °C
Temp coefficient (max) zero	± 0.09E-5/ °C
Temp coefficient (max) calibration	± 0.015%/ °C

Table. 5.4. Specifications of Lakeshore Hall Effect probe MNT-4E04-VH[10]

The Lakeshore Gaussmeter 450 with MNT-4E04-VH probe can provide 10^{-7} Tesla resolution on the 3 mT range when measuring magnetic field at DC and 50Hz. The measurement accuracy is $\pm 0.10\%$ of reading and $\pm 0.005\%$ of range for DC field measurements and $\pm 2\%$ of reading at 50Hz at the temperature of 20 °C.

An alternative way of measuring AC magnetic field is the inductive sensing coils. Compared to the Hall effect probe, the effective area in which the magnetic field is being measured is much larger due to the size of the coil. The measured field will be an average field across the sensing coil rather a point value at the location. This will make a difference especially when measuring a non-uniform field. However, the magnetic field range that the inductive coil measures can be easily improved in several ways such as increasing number of turns or amplification of the output.

The sensing coil has to be as small as possible to measure the field across a small area. A 500-turn, 10 mm high, 0.7 mm diameter coil was used to measure the AC magnetic field. An amplification circuit was built to improve the sensitivity of the measurement. The operational amplifier LF353[11] was configured as in Fig. 5.12 to amplify the output from the sensing coil before the measurement by the voltmeter. The gain was set by the ratio of the resistance of R and R_1 , to be 1000.

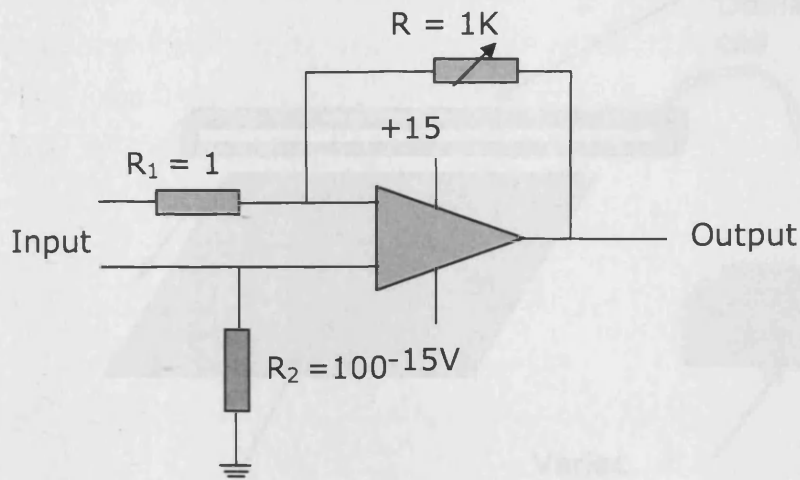


Fig. 5.12. Amplification circuit using LF353 [11]

The calibrated Hall effect probe is commercially available and easy to use, however, there are limits on the measurement resolution and frequency range. Comparing with the Hall effect probe, the sensing coil provides a more powerful method with signal amplification for measuring the low field, but introduces uncertainty on the location where the measurement is taken due to its larger size. The shielding factors presented in chapter 6 are from the Hall effect probe, while the out-of-plane field contour on the sample surface is for the measurement by the sensing coil with the amplification circuit.

5.7. Sample demagnetization and test repeatability

The magnetization status of the sample determines its permeability. The purpose of demagnetization is to remove the effect of the remnant magnetization of the sample and achieve repeatable measurements. This process is critical for many magnetic measurements. As discussed in chapter 2, a widely used method is by reversal of the applied field. To accommodate the planar samples in the shielding factor measurement, a demagnetizing coil is designed as shown in Fig. 5.13.

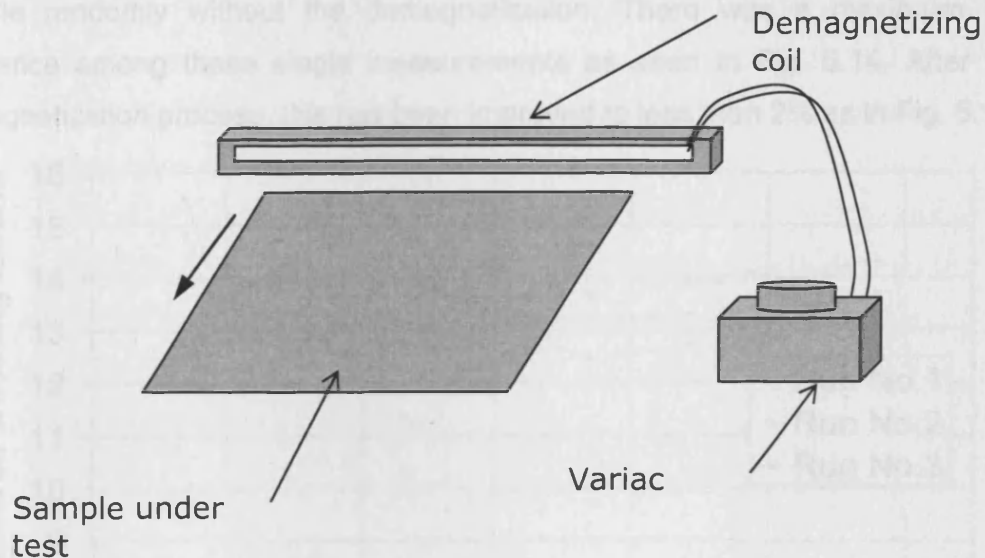


Fig. 5.13. Sample demagnetization by passing through a demagnetizing coil

The former of the demagnetizing coil has a 520 mm wide and 5 mm deep slot for the sample to pass through. The length of the coil is 120 mm. 350 turns with 1.2 mm thick copper wire provides a maximum magnetic field around 5000 A/m when there is a 3.6 A demagnetizing current at 50 Hz. The sample could be passed through the coil with a constant current from the variac to the coil. The applied field on the sample is decreasing as it passes through. It can be seen from the measured shielding factor that demagnetizing procedure is necessary for all shielding factor measurements, especially at DC and frequencies lower than 100 Hz.

The magnetic flux generated from the magnetizing solenoid penetrates into the sample and diverts along the sample. Both in-plane and out-plane magnetization are involved. Although the demagnetization is only done along the in-plane direction (rolling directions of grain oriented and both rolling and transverse directions of non-oriented steels), there is a good improvement on the repeatability as demonstrated below, because firstly the majority of the flux is along the in-plane direction, secondly the remnant magnetization along the out-

plane direction is unlikely. Seven measurements were carried out on the same sample randomly without the demagnetization. There was a maximum 9% difference among these single measurements as seen in Fig. 5.14. After the demagnetization process, this has been improved to less than 2% as in Fig. 5.15.

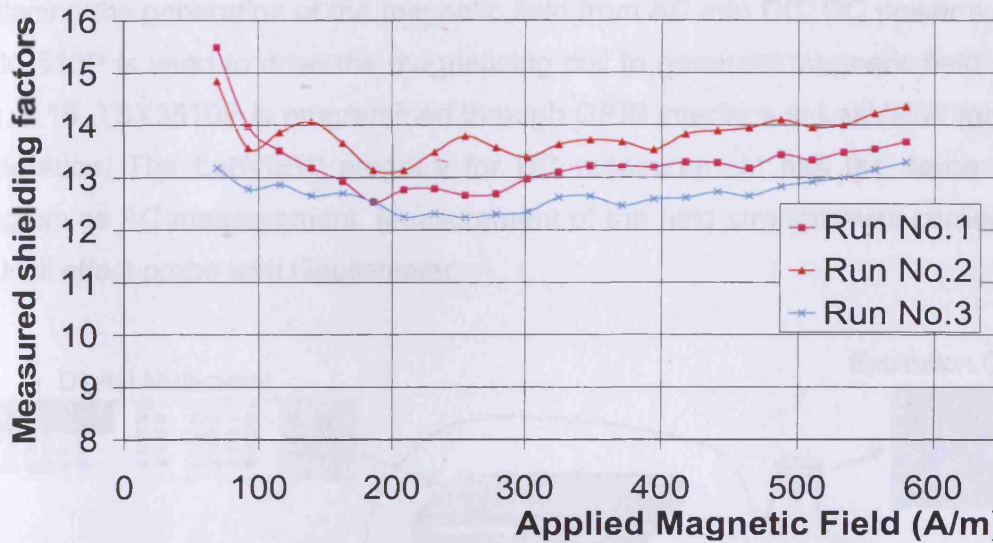


Fig. 5.14. Measured 50 Hz shielding factors of grain-oriented steel M103-27P from random measurements of without demagnetization procedure.

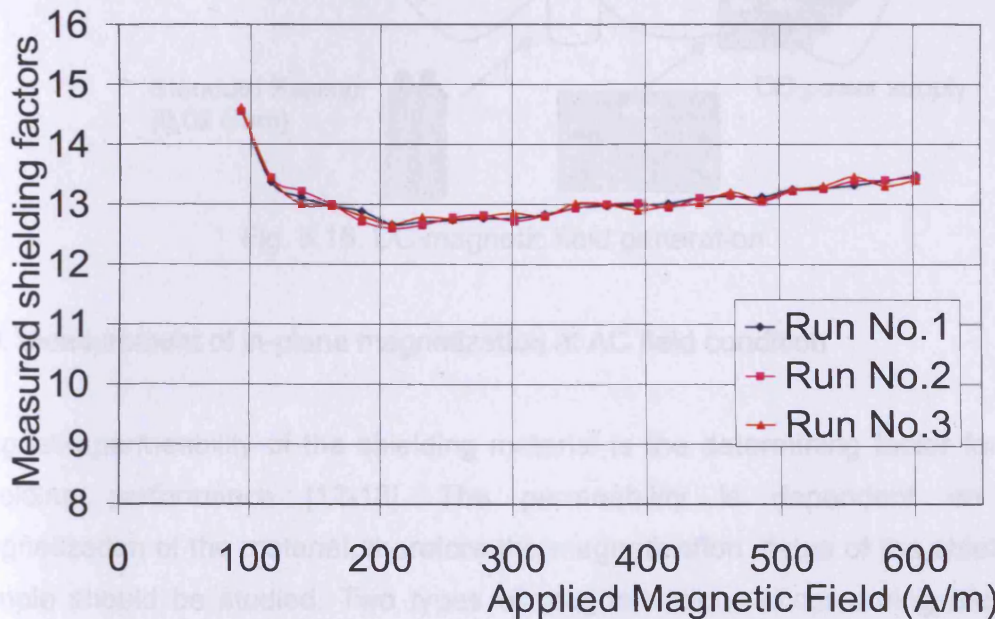


Fig. 5.15. Shielding factors from random measurements of grain-oriented steel M103-27P with demagnetizing procedures

5.8. DC magnetic shielding factor measurement

The setups of measurements at AC conditions are presented in this section. With this setup, DC shielding factor of the samples can also be measured by only replacing the generation of the magnetic field from AC into DC. DC power supply TSX3510P is used to drive the magnetizing coil to generate magnetic field as in Fig. 5.16. TSX3510P is programmed through GPIB interface in LabVIEW for field generation. The LabVIEW program for DC measurement has the same logic diagram as AC measurement. Measurement of the field strength was carried out by Hall effect probe with Gaussmeter.

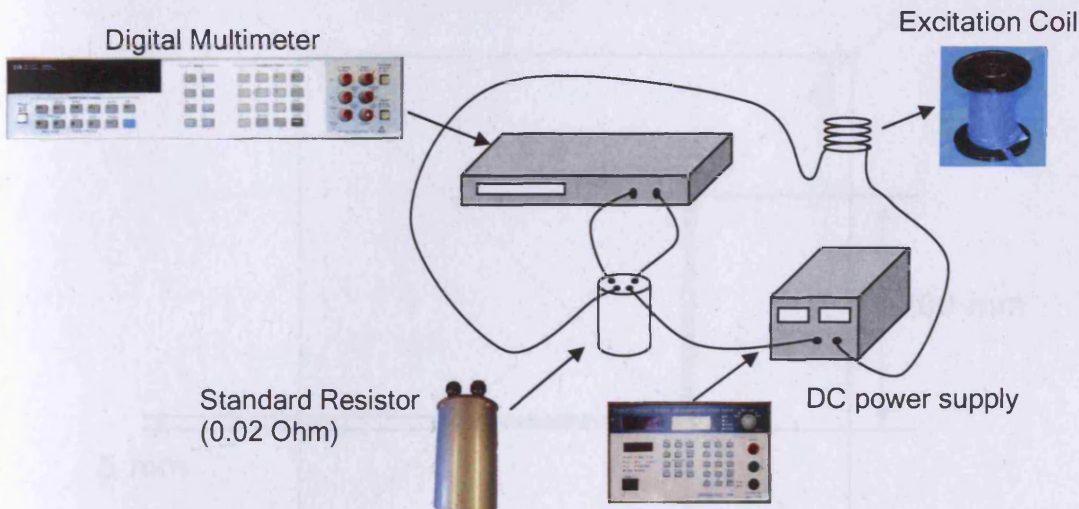


Fig. 5.16. DC magnetic field generation

5.9. Measurement of in-plane magnetization at AC field condition

Magnetic permeability of the shielding material is the determining factor for the shielding performance [12-13]. The permeability is dependent on the magnetization of the material, therefore the magnetization status of the shielding sample should be studied. Two types of magnetizations occur during the flux being ducted by the shield. The first type is a complicated three-dimensional magnetization during the flux entering and rotating from the perpendicular direction to the in-plane direction. The other type is the magnetization along the

in-plane direction. The in-plane magnetization determines the ability of the shield holding the flux within the shield.

To investigate the in-plane magnetization of the shielding sample, holes were drilled into the sample and B-sensing coils were mounted across the holes. The layout of the sensing coils can be seen in Fig. 5.17. The width of the coil is much larger compared to the size of the drilled hole to minimize effect of the damaged magnetic properties due to the drilling process. The output signal of the five-turn sensing coil is amplified using the amplification circuit shown as in Fig. 5.13. The peak magnetization was integrated from the output voltage of the sensing coil.

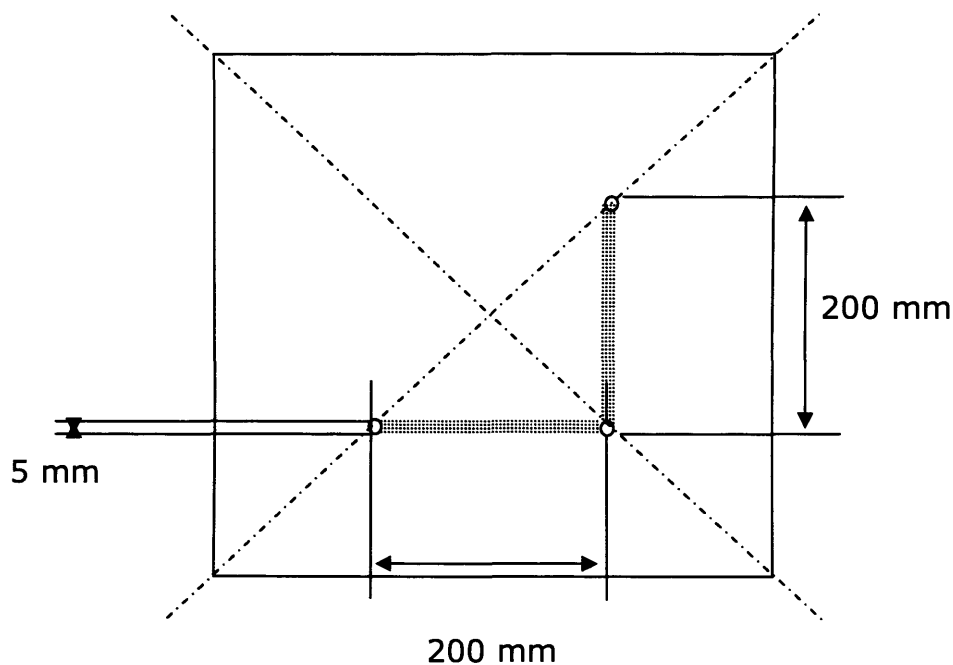


Fig. 5.17. Layout of the B-Sensing coil on the shielding sample

In-plane magnetization closer to the centre of the sample is also measured by additional sensing coils shown in Fig. 5.18. The additional coil is with 5 turns winding and 100 mm wide. The distance to the centre of the panel is 50 mm, which is half of the distance between the original 200 mm wide sensing coil and the panel centre.

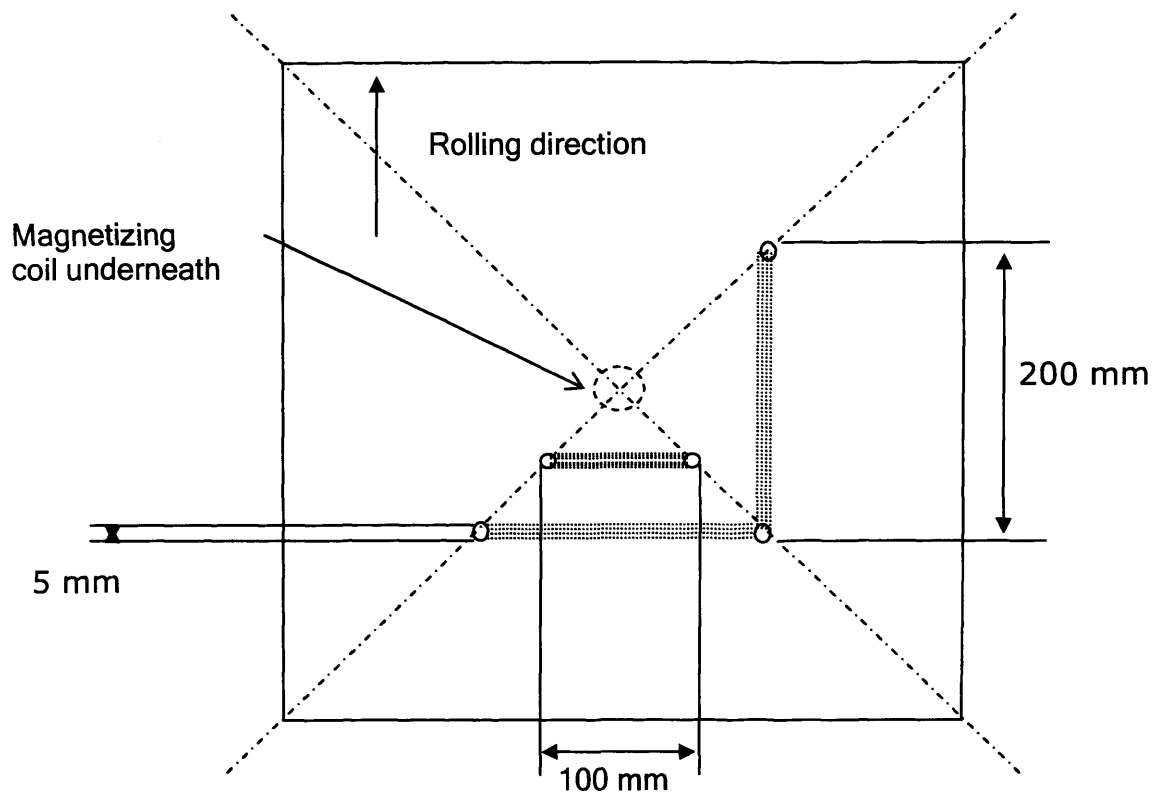


Fig. 5.18. Location of 100 mm wide coils to measure the in-plane magnetization along the rolling directions at different location

References:

1. U.S. Government, "*MIL-STD-285, Attenuation measurements for enclosures, electromagnetic shielding, for electronic test purposes, method of.*" U.S. Government, 1954.
2. IEEE, "*IEEE STD 299, Shielding enclosures, electromagnetic, for electronic test purposes, method for measuring the effectiveness of.*" Institute of Electrical and Electronic Engineers, 1985.
3. ASTM, "*Standard Test Method for Magnetic Shield Efficiency in Attenuating Alternating Magnetic Fields,*" American Society of Testing Materials. 2002.
4. Rikitake, T., *Magnetic and Electromagnetic Shielding.* Kluwer Academic Publishers, 1987.
5. Jiles, D., *Introduction to Magnetism and Magnetic Materials.* 2nd. ed. New York, Chapman&Hall, 1997.
6. Cogent Power, *Products brochure: Unisil, Unisil-H, Grain oriented electrical steels.* Cogent Power Ltd, 2004.
7. Cogent Power, *Products brochure: Non-oriented full processed electrical steels.* Cogent Power Ltd, 2003.
8. National Instruments. *GPIB(IEEE 488) Solution,* 1999.
9. National Instruments. *Manual: LabVIEW user guide,* 1999.
10. Lakeshore Instrument, *User Manual: DSP Gaussmeter 450.* 1998.
11. National Semiconductor. *User Manual - LF353.*
12. Okazaki, Y.; Fujirawa, M., "*Magnetic shielding by grain oriented silicon steel composite panels.*" Studies in Applied Electromagnetic and Mechanics 10: Nonlinear Electromagnetic systems, pp. 644-647, 1996.
13. Okazaki, Y.; Ueo, K., "*Magnetic shielding by soft magnetic materials in alternating magnetic field,*" Journal of Magnetism and Magnetic Materials, Volume: 112, pp. 192-194, 1992.

Chapter Six.

Results and Discussions

Variety of electrical steel panels were tested with the test method introduced in Chapter 5. Measured shielding factors at DC and AC up to 400 Hz are presented and discussed in this chapter. The discussion of the test results is also extended with the 2-dimensional FEM method due to the capability of the test and the availability of the samples. The measured shielding factor of the electrical steel is determined by the material properties, such as thickness, permeability and conductivity. The study covers the following aspects:

- Sample thickness
- Power loss grade of the sample
- Eddy current cancellation in AC shielding
- Double-layered shield
- Out -of-plane flux and in-plane magnetization
- Drilled hole as a defect in the shield
- Joints

6.1 Panel thickness

The study of single shell spherical and cylindrical shields was presented in chapter 4 and the approximated shielding factors can be calculated by equation 6.1 for spheres and 6.2 for cylinders [1]. It can be seen that the shielding factor increases with the thickness of the shield with uniform external field and simple geometry of the shields.

$$S = 1 + \frac{2}{3} \frac{\mu t}{R} \quad (6.1)$$

$$S = 1 + \frac{1}{2} \frac{\mu t}{R} \quad (6.2)$$

To study how the thickness of the electrical steel panel affects the shielding factor in the experiment, the ideal case is to test the samples of the same magnetic property but of different thickness. However, the electrical steel panels, which can meet this requirement, are not available due to the manufacture process. Grain-oriented steel 27M4 and 30M3 are 3.1% silicon steels manufactured by the same process but of thickness 0.27 and 0.30 mm respectively. It can be seen from Fig. 6.1 that the measured relative permeability of these two samples along the rolling directions obtained using the standard Epstein frame test method [2] are very similar, so any performance difference will be due to the thickness only.

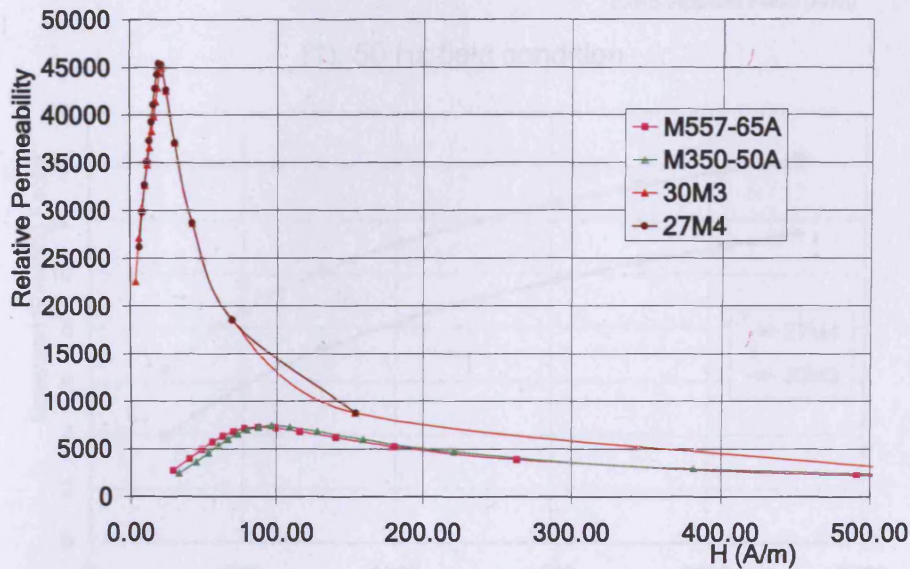
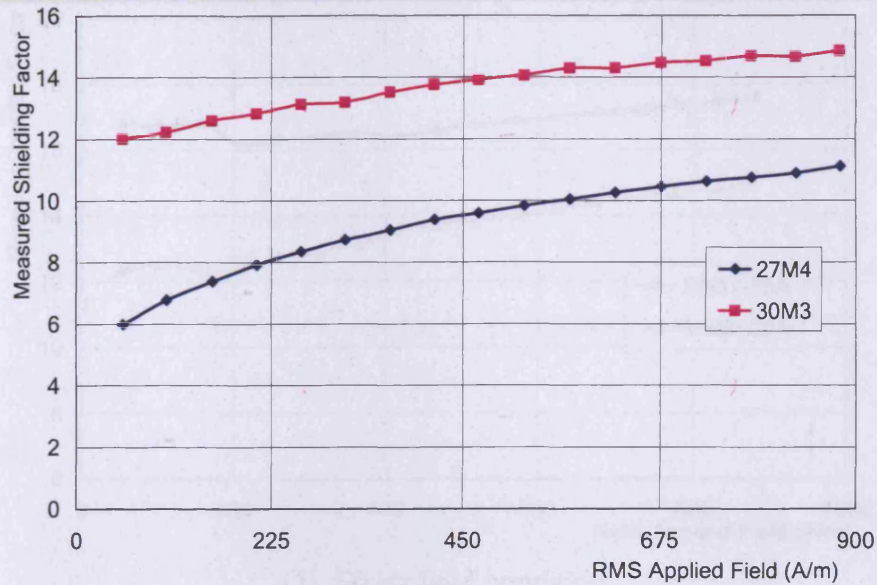


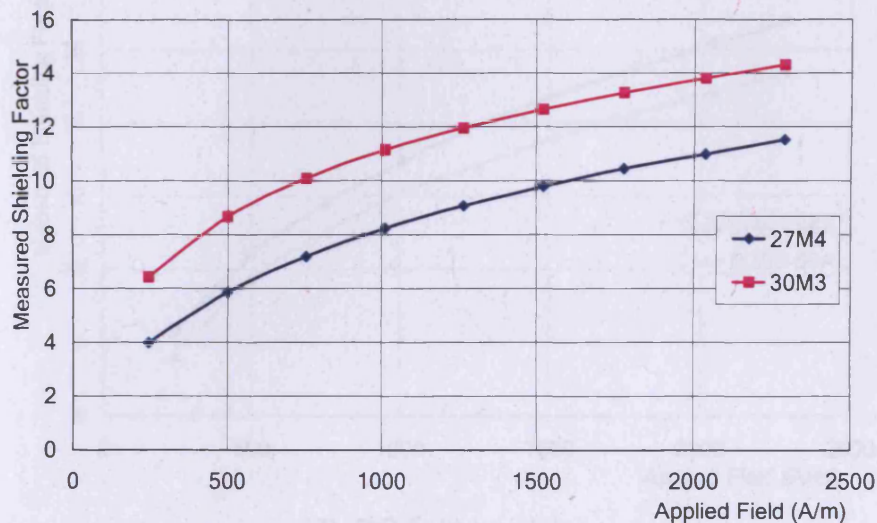
Fig. 6.1. Variation of relative permeability of Epstein strips with applied magnetic field at 50Hz sinusoidal conditions measured using the standard Epstein frame test method

The shielding panels of 27M4 and 30M3 are tested at static field and 50 Hz conditions respectively. It can be seen from Fig. 6.2 that as expected the thicker sample has better shielding factor over the full range of applied field.

Chapter 6. Results and Discussions



(1). 50 Hz field condition

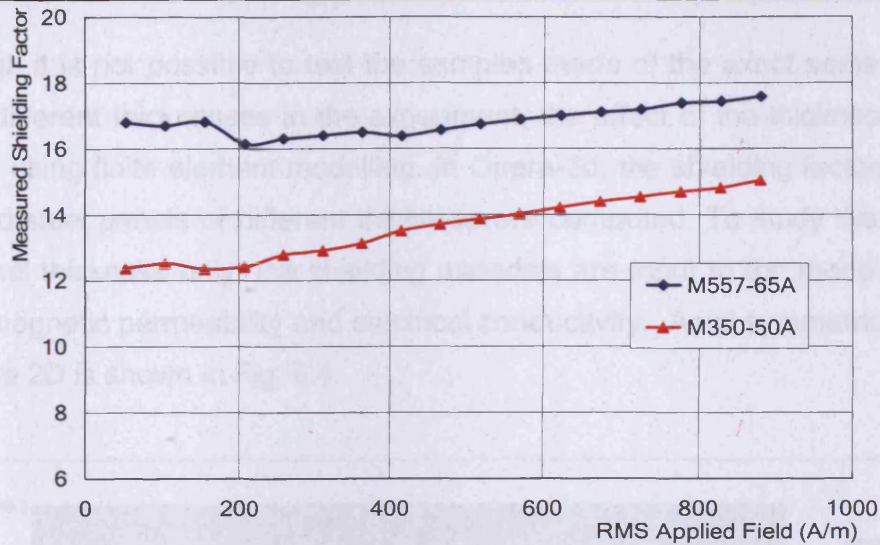


(2). DC field condition

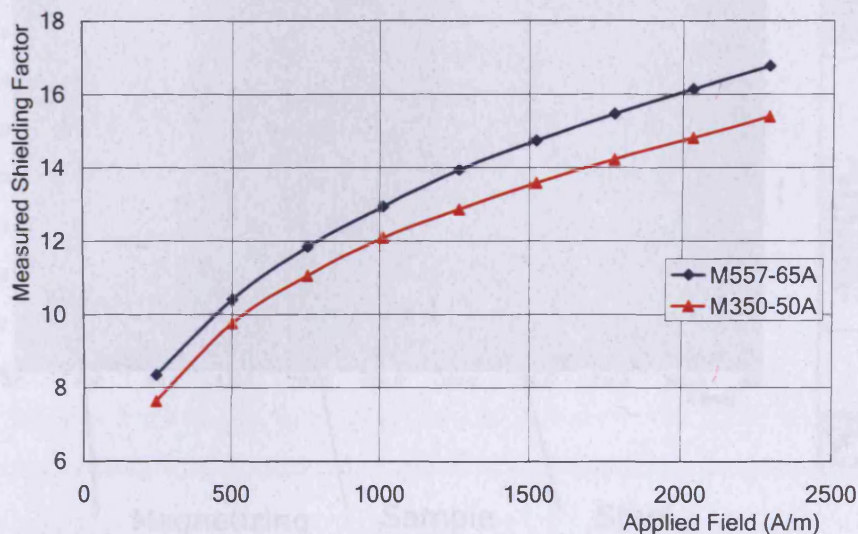
Fig. 6.2. Variation of measured shielding factors of 0.27 mm and 0.30 mm conventional grain-oriented steels with applied magnetic field strength at DC and 50 Hz

The same trend is seen in the comparison between non-oriented steel M350-50A and M557-65A in Fig. 6.3. Both samples have 1.3% silicon composition and the thicknesses are 0.50 mm and 0.65 mm respectively.

Chapter 6. Results and Discussions



(1). 50 Hz field condition



(2). DC field condition

Fig. 6.3. Variation of measured shielding factors of 0.50 mm and 0.65 mm non-oriented steels with applied magnetic field strength at DC and 50 Hz

It can be seen from Fig. 6.2 and Fig. 6.3 that thicker shield has a better shielding factor if the materials have similar magnetic properties. This applies for both grain-oriented and non-oriented samples. This trend also agrees with the theoretical calculation of the shielding factor of the spherical shield shown in Fig. 3.3 in chapter 3.

Although it is not possible to test the samples made of the exact same material but of different thicknesses in the experiment, the effect of the thickness can be studied using finite element modelling. In Opera-2d, the shielding factors of non-oriented steel panels of different thickness are computed. To study the effect of the panel thickness only, the shielding materials are input to the model with the same magnetic permeability and electrical conductivity. Axial symmetrical model in Opera 2D is shown in Fig. 6.4.

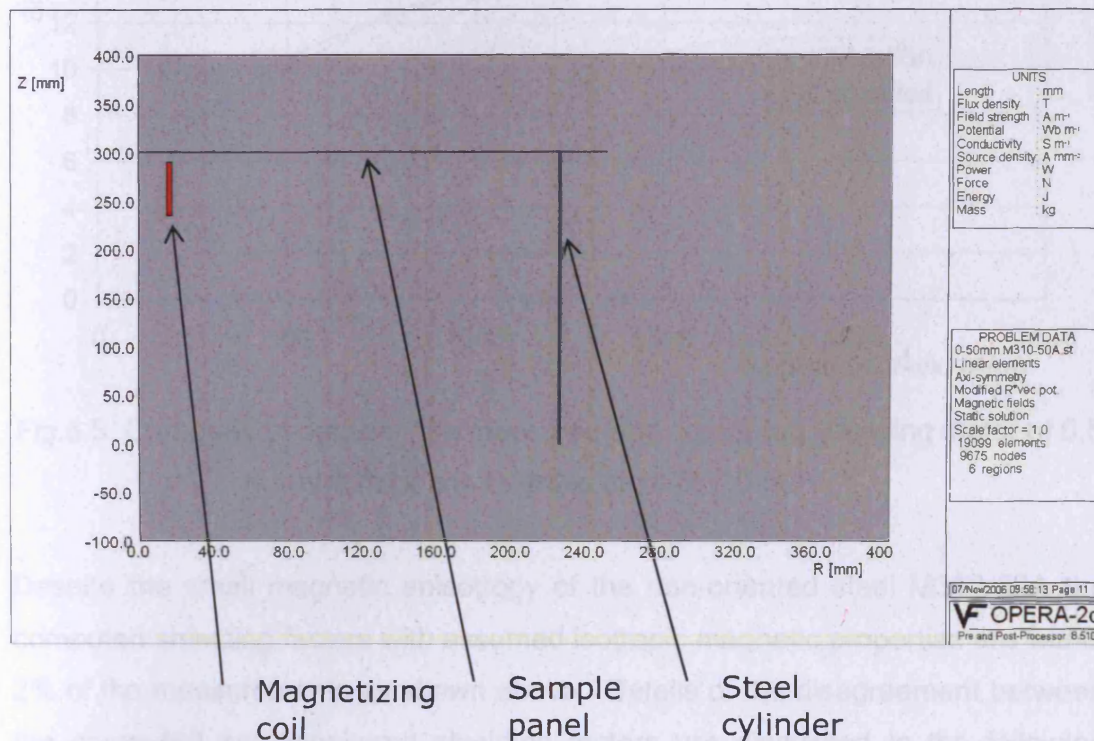


Fig. 6.4. Axial symmetry 2 dimensional model of the test setup in Opera-2d

Non-linear computation is enabled by the input of the B-H curve of the sample. The B-H curve in this model is measured from Epstein strips of M310-50A. The simplification made in the model is that the material is magnetically isotropic. The measured in-plane B-H curve is used to describe the magnetic property along any directions in the sample. The shielding phenomenon involves incident flux

Chapter 6. Results and Discussions

rotation inside the material, therefore the simplification of the isotropic material brings certain errors. Beside the assumption of the isotropic shielding material, B-H characteristics along the out-of-plane direction cannot be measured due to the difficulty in measuring the flux density within the sample. The difference between the computed and measured shielding factor is shown in Fig. 6.5.

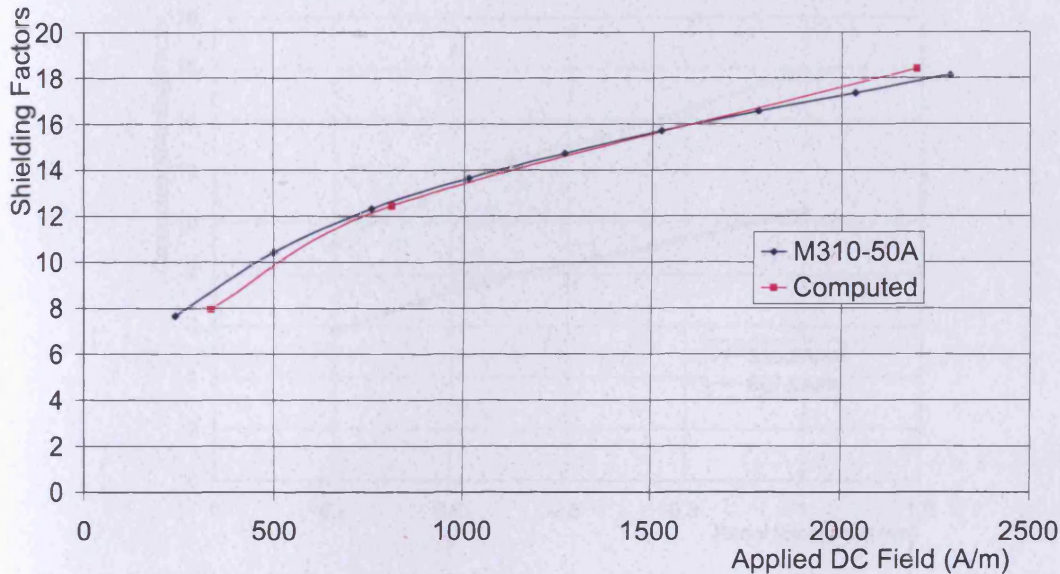


Fig.6.5. Comparison between the measured and computed shielding factor of 0.5 mm thick non-oriented steel M310-50A

Despite the small magnetic anisotropy of the non-oriented steel M310-50A the computed shielding factors with assumed isotropic magnetic properties are within 2% of the measurements as shown above. Details of the disagreement between the computed and measured shielding factors are discussed in the following section.

Panels of the material of the same magnetic permeability and electrical conductivity as M310-50A but of different thickness are modelled. The variation of the shielding factors at different applied fields at reference point with the increasing thickness is presented in Fig. 6.6. An approximated linear relationship is seen between the shielding factor and the thickness of the shield. The shielding factors of the panels under this setup cannot be calculated analytically

because of the complex geometries of the test rig and also the non-uniform excitation. However the linear relationship in Fig. 6.6 agrees with equation 6.1 and 6.2, which give static shielding factor of single shell spherical and cylindrical shields.

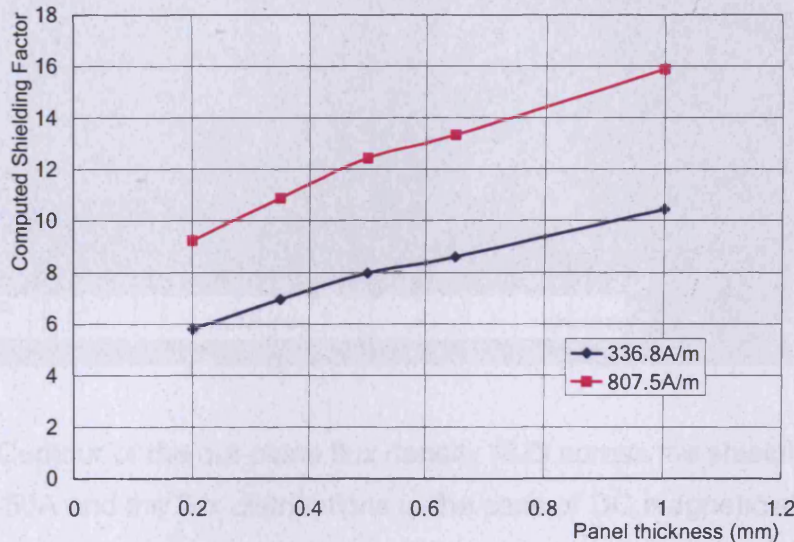


Fig. 6.6. Variation of the modelled DC shielding factors of panels at different applied reference fields with the thickness of the panel

It is important to study the magnetization status of the shielding, because the magnetic permeability of the material depends on the magnetization. The magnetization is not uniform within the sample due to the magnetizing method. It is not practical to measure 3-dimensional flux density at certain points of interest within the sample. Therefore this is investigated in Opera-2d to help understand the theory. The magnetic field source is perpendicular to the sample, however the flux rotates inside the sample and tries to follow the magnetically easy path. The flux distribution inside the sample can be broken into two parts: along the in-plane directions and out-plane directions. The component along the out-plane direction represents the magnetic flux which is penetrating through the shielding sample and the one along the in-plane direction for the flux diverted by the shield. This is presented in Fig. 6.7 with the applied field at the reference point of 827 A/m.

Chapter 6. Results and Discussions

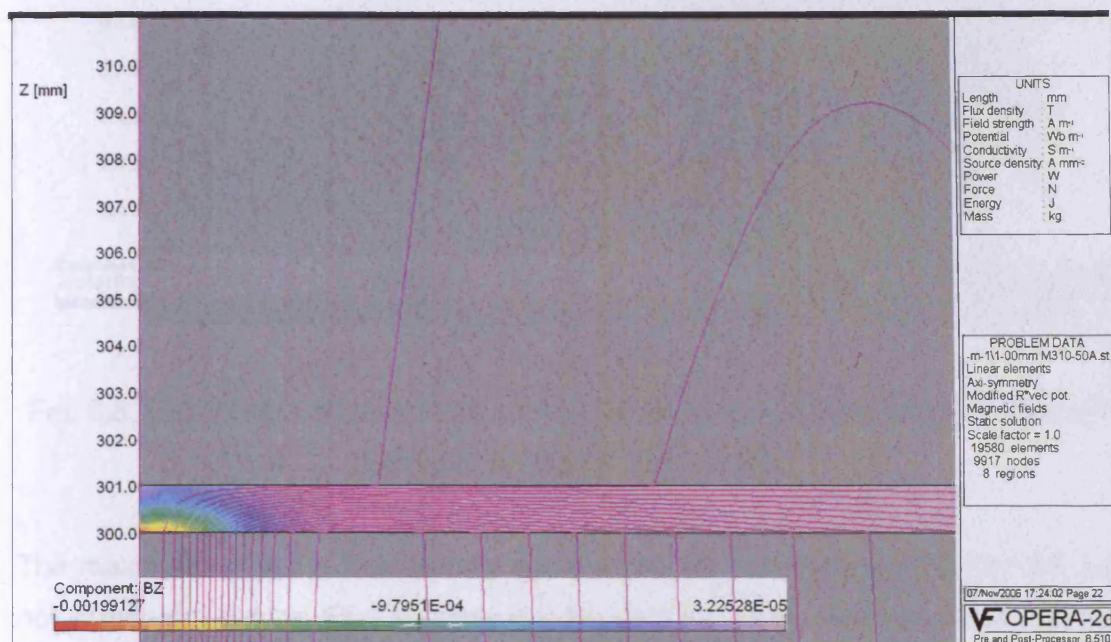


Fig. 6.7. Contour of the out-plane flux density (BZ) across the shielding sample M310-50A and the flux distributions in the case of DC magnetic shielding

The maximum of BZ (-1.99127 mT) appears above the magnetizing solenoid. The flux rotates and turns along the sample. The majority of the flux leaves the shield from the bottom surface going back to the other end of the excitation coil of the magnetic field source. It can be seen that only a small amount of flux escapes from the top surface to the shielded region, but most of it returns to the top surface from the shielded region again. Because the majority of the flux keeps leaving the shield from the bottom surface, the magnetization along the sample direction BR decreases as the distance increase from the field source as shown in Fig. 6.8. The amplitude of the flux density distribution regardless of its direction is presented in Fig. 6.9.

Chapter 6. Results and Discussions

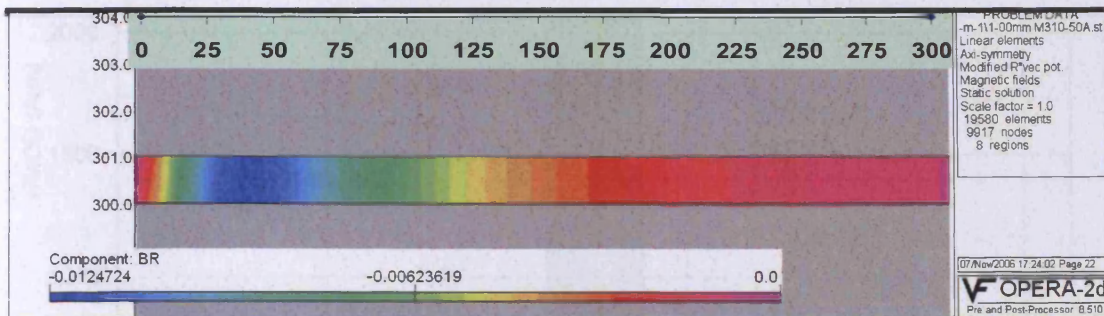


Fig. 6.8. Distribution of the flux along the sample in-plane direction (BR) through the cross section of the sample.

The maximum in-plane flux density appears on the top of the excitation coil, but not in the very centre. Flux leakage is from both top and bottom surfaces and the in-plane flux density in the sample decreases quickly when move away from the excitation coil. The total flux density shows the same trend as shown in Fig. 6.9.

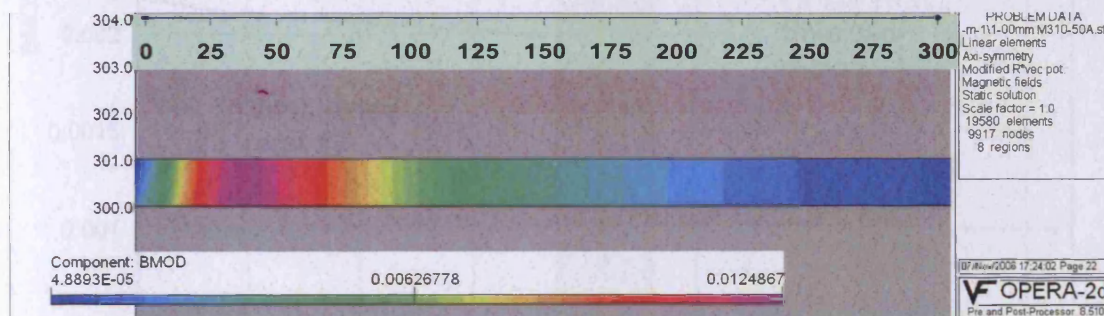
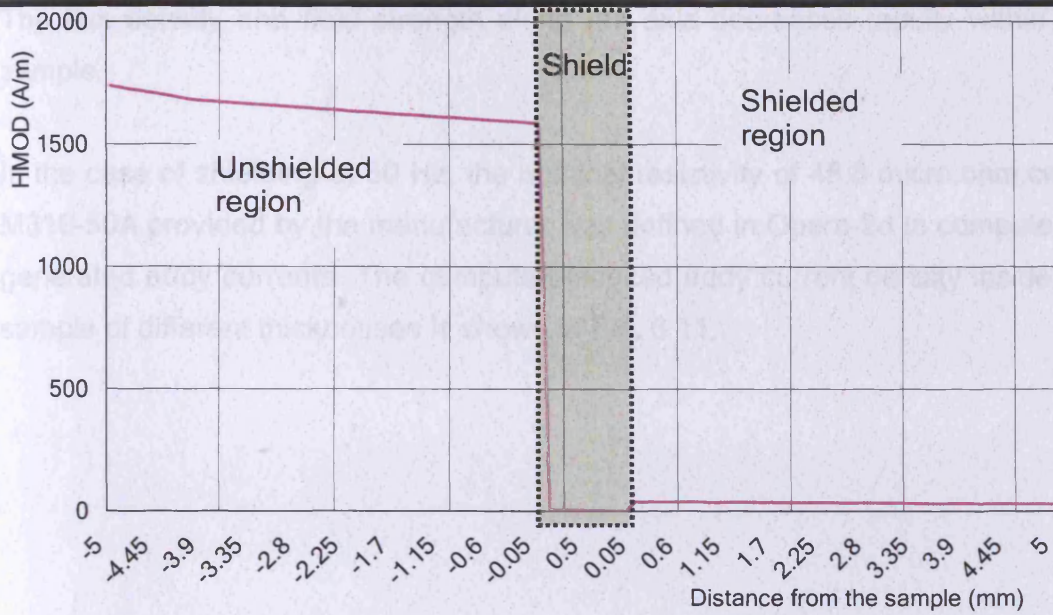


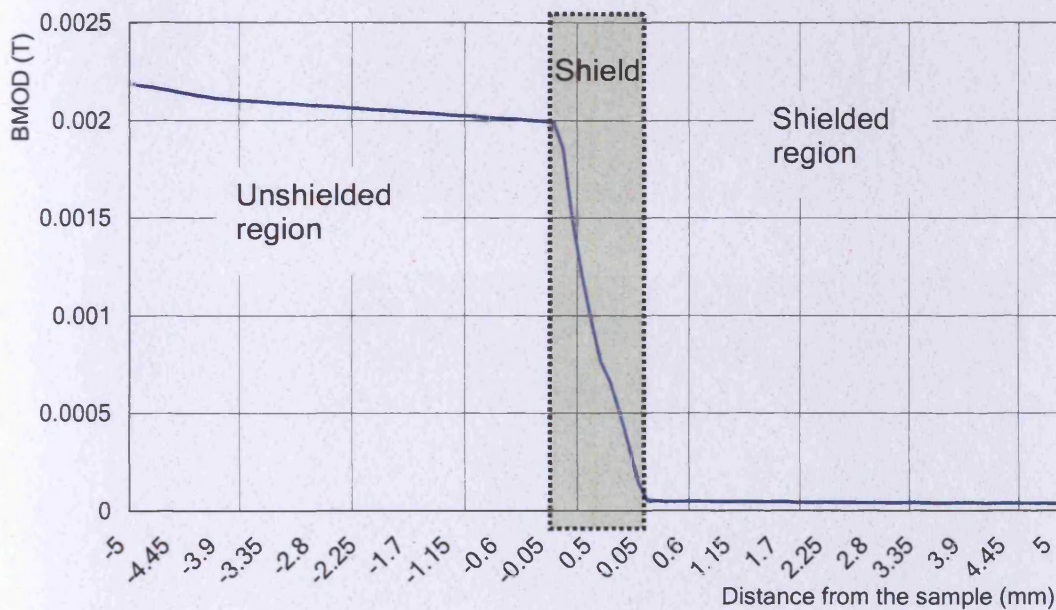
Fig. 6.9. Contour of the flux density (scalar amplitude BMOD) through the cross-section of the sample.

The magnetic field strength and flux density along the axis of the model from 5 mm below the sample to 5 mm above the sample is plotted in Fig. 6.10.

Chapter 6. Results and Discussions



(1). Magnetic Field strength (H_{MOD})



(2). Magnetic Flux Density (B_{MOD})

Fig. 6.10. The variation of the computed DC magnetic field strength and flux density along the axis of the model with the distance from the sample. (From 5 mm below the sample to 5 mm above the sample)

Chapter 6. Results and Discussions

The flux density and field strength along the axis decreases rapidly within the sample.

In the case of shielding at 50 Hz, the nominal resistivity of 48.8 micro.ohm.cm of M310-50A provided by the manufacturer was defined in Opera-2d to compute the generated eddy currents. The computed induced eddy current density inside the sample of different thicknesses is shown in Fig. 6.11.

Chapter 6. Results and Discussions

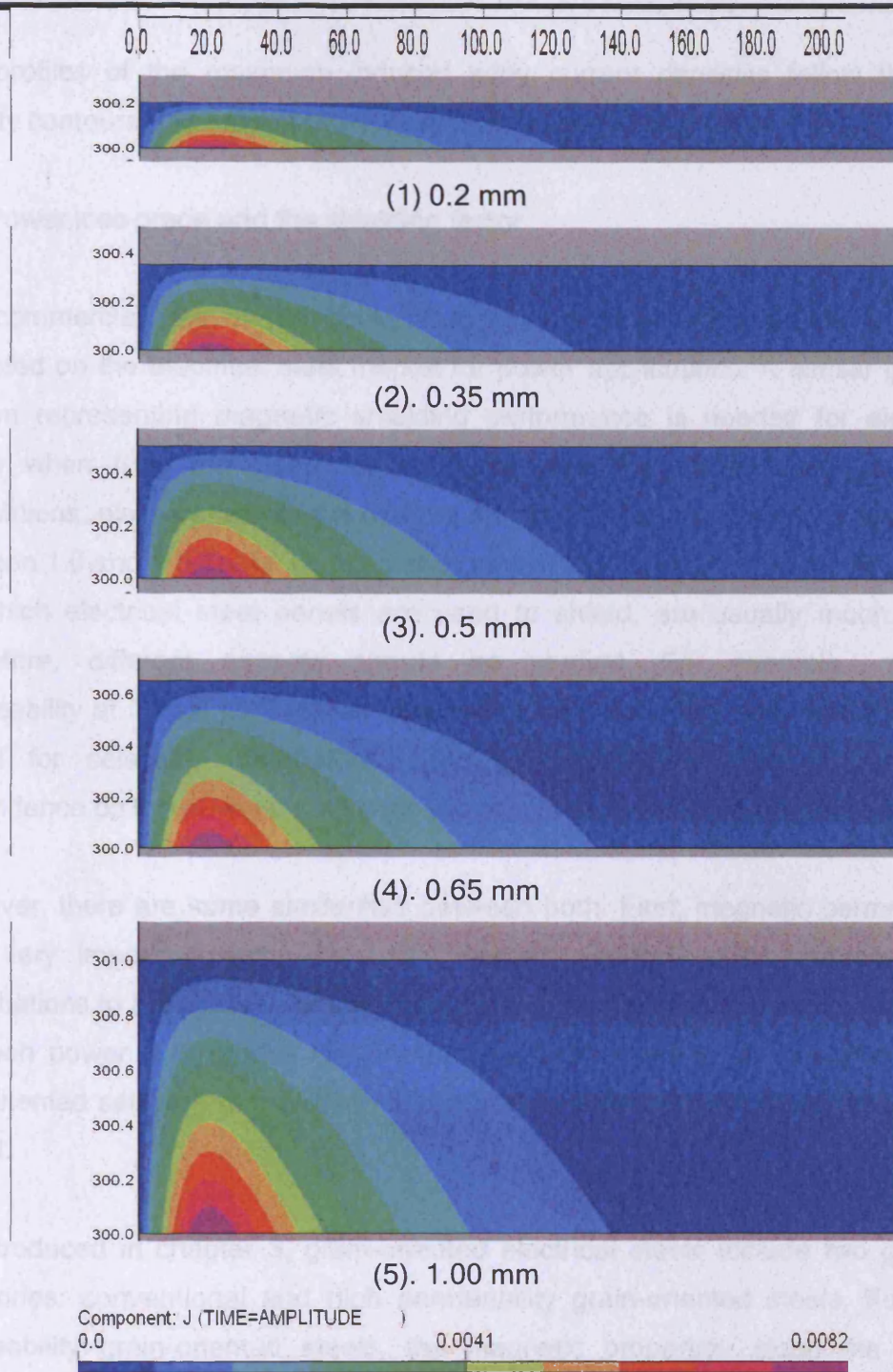


Fig. 6.11. Distribution of computed induced eddy current density within samples of different thickness

The profiles of the maximum induced eddy current densities follow the flux density contours and are not dependent on the sample thickness.

6.2. Power loss grade and the shielding factor

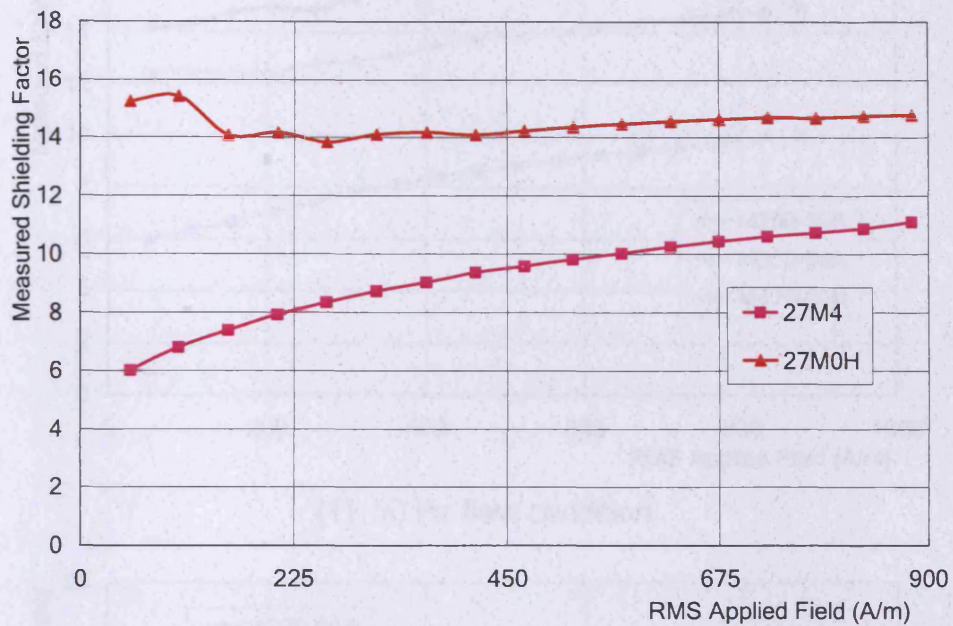
The commercial use of the power loss grades of electrical steels is widely accepted on the electrical steel market for power applications. A similar grading system representing magnetic shielding performance is needed for electrical steels when they are used for magnetic shielding applications. In power applications, electrical steels are used to amplify the flux and usually magnetized between 1.0 and 1.8 Tesla. Compared to power applications, the magnetic fields, for which electrical steel panels are used to shield, are usually much lower. Therefore, different aspects should be studied. For example, material permeability at 1.5 or 1.7 Tesla is important for transformers and motors but not useful for selecting material to build magnetically shielded rooms. The dependence on the power loss grades for magnetic shielding can be wrong.

However, there are some similarities between both. First, magnetic permeability is a very important factor for both. Second, induced eddy currents bring contributions to both power loss and shielding factor. To discover the correlations between power loss grades and magnetic shielding factor, grain-oriented and non-oriented samples of the same thickness but different power loss grades are tested.

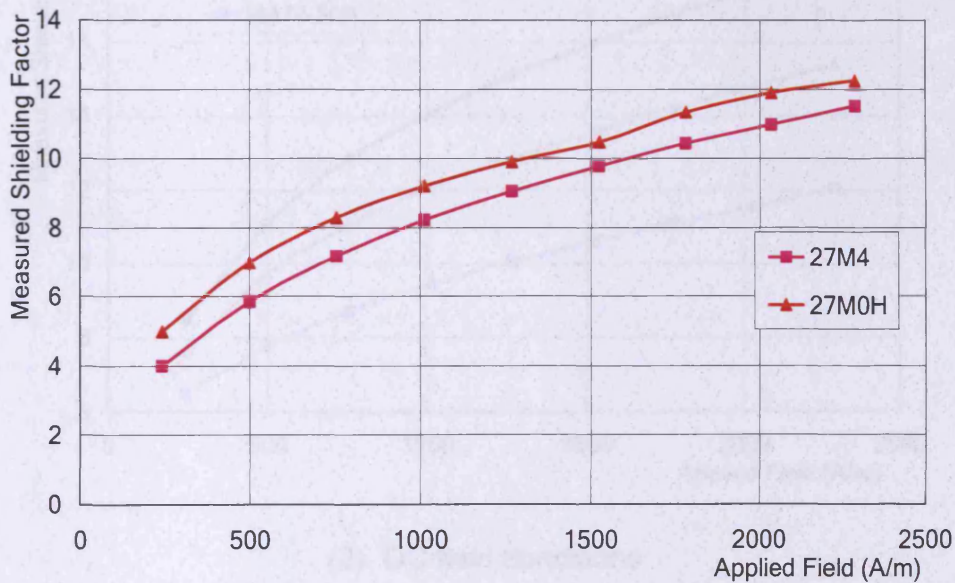
As introduced in chapter 3, grain-oriented electrical steels include two general categories: conventional and high permeability grain-oriented steels. For high permeability grain-oriented steels, the magnetic properties along the rolling direction are further improved and offer a lower power loss compared with the conventional grain-oriented steels. 27M4 and 27M0H are both 0.27 mm thick grain-oriented steels. 27M4 is conventional while 27M0H is high permeability

Chapter 6. Results and Discussions

grain-oriented steel. The shielding factors of 27M4 and 27M0H at DC and 50 Hz field conditions are measured and shown in Fig. 6.12.



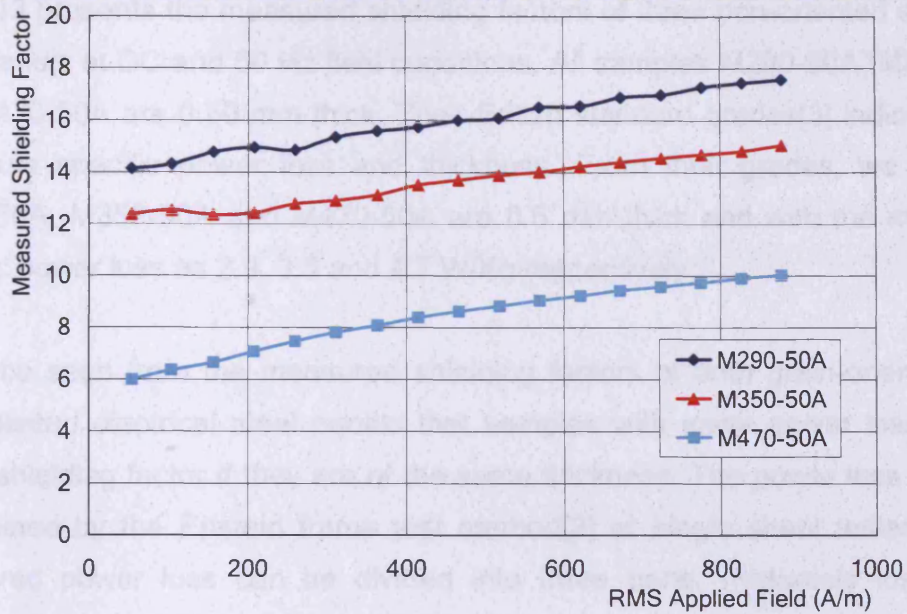
(1). 50 Hz field condition



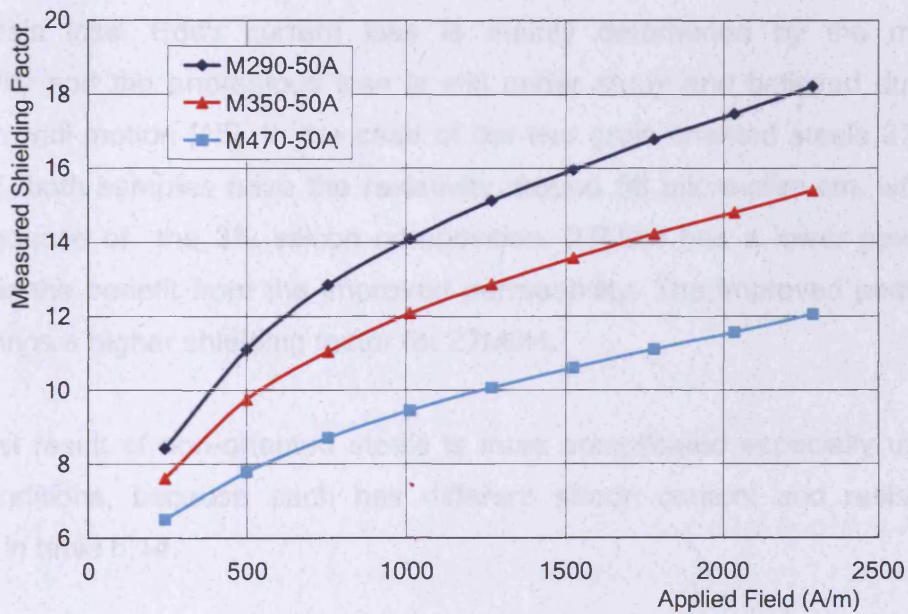
(2). DC field condition

Fig. 6.12. Variation of measured shielding factor of 0.27 mm thick grain-oriented steels with applied field strength at 50 Hz and DC field conditions

Chapter 6. Results and Discussions



(1). 50 Hz field condition



(2). DC field conditions

Fig. 6.13. Variation of measured shielding factor of three 0.50 mm thick non-oriented steels with applied field strength at 50 Hz and DC field conditions

Chapter 6. Results and Discussions

Fig. 6.13 presents the measured shielding factors of three non-oriented electrical steel panels at DC and 50 Hz field conditions. All samples M290-50A, M350-50A and M470-50A are 0.50 mm thick. Their British standard grades[3] indicate their maximum specific power loss and thickness. From their grades, we can tell M290-50A, M350-50A and M470-50A are 0.5 mm thick and with the maximum specific power loss as 2.9, 3.5 and 4.7 W/Kg respectively.

It can be seen from the measured shielding factors of both grain-oriented and non-oriented electrical steel panels that samples with lower power loss give a better shielding factor if they are of the same thickness. The power loss grade is determined by the Epstein frame test method[2] or single sheet tester[4]. The measured power loss can be divided into three parts, hysteresis loss, eddy current loss and anomalous loss[5]. The hysteresis loss depends on magnetic properties of the material, generally higher permeability indicates lower hysteresis loss. Eddy current loss is mainly determined by the material's resistivity and the anomalous loss is still under study and believed due to the domain wall motion [15]. In the case of the two grain-oriented steels 27M4 and 27M0H, both samples have the resistivity around 58 micro-ohm-cm, which is a consequence of the 3% silicon composition. 27M0H has a lower power loss, which is the benefit from the improved permeability. The improved permeability also brings a higher shielding factor for 27M0H.

The test result of non-oriented steels is more complicated especially under the AC conditions, because each has different silicon content and resistivity as shown in table 6.14.

Grade	Silicon content	Resistivity (micro.ohm.cms)
M290-50A	3.27%	59
M350-50A	1.81%	36.4
M470-50A	1.28%	30.2

Table. 6.14. Silicon contents and resistivity of non-oriented steels [6]

According to the basic shielding theory introduced in chapter 3, the shielding factor depends on both flux ducting and eddy currents. Although M290-50A has the highest silicon content, which decreases the amount eddy current, generated under the same magnetizing condition, its permeability is the determining factor and flux ducting is the dominant effect, therefore it gives the best shielding factor among the samples shown in Table. 6.14.

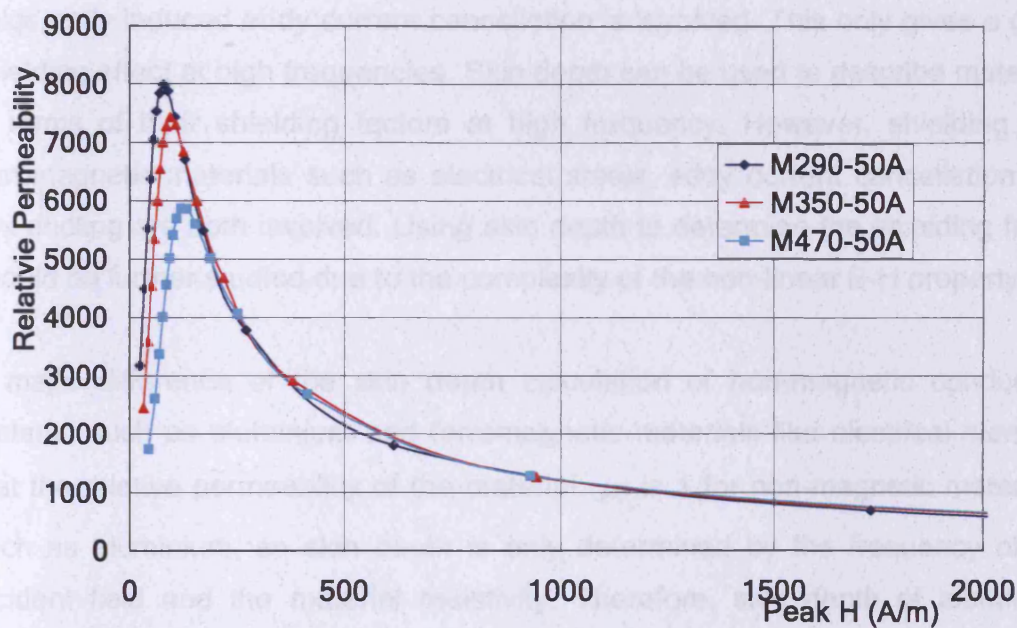


Fig.6.15. Variation of measured relative permeability of non-oriented steel samples by Epstein frame method with applied magnetic field strength

It can be seen from the results presented above that magnetic permeability plays a more important role than the resistivity at 50 Hz. Magnetic flux ducting is the determining factor in low frequency magnetic shielding. As the frequency increases, the eddy current cancellation plays a more important role. This is discussed in section 6.3.

6.3. Frequency dependent shielding factors

The amount of induced eddy current depends on the frequency of the incident magnetic field and material properties. The skin depth[7] represents the capability of the material to attenuate the incident electromagnetic fields with induced eddy current.

If non-magnetic conducting materials are used to shield against the AC magnetic fields, only induced eddy current cancellation is involved. This only gives a good shielding effect at high frequencies. Skin depth can be used to describe materials in terms of their shielding factors at high frequency. However, shielding with ferromagnetic materials such as electrical steels, eddy current cancellation and flux ducting are both involved. Using skin depth to determine the shielding factor should be further studied due to the complexity of the non-linear B-H property.

A major difference of the skin depth calculation of non-magnetic conducting material such as aluminium and ferromagnetic materials like electrical steels is that the relative permeability of the material. μ_r is 1 for non-magnetic materials, such as aluminium, so skin depth is only determined by the frequency of the incident field and the material resistivity. Therefore, skin depth of aluminium decreases with the increase of the frequency, therefore aluminium has better shielding factor at higher frequency. However, the skin depth of electrical steel does not have such a simple relationship with frequency of the incident field, because its relative permeability is very dependent on the material's magnetization status. Fig. 6.15 shows the measured 50 Hz relative permeability of non-oriented steel M470-50A with the standard Epstein frame tests. The skin depth of M470-50A also becomes dependent on the magnetization of the material due to the permeability dependence on applied field. Taking the curve shown in Fig. 6.15 into account, the skin depth can be calculated depending on the applied field as presented in Fig. 6.16.

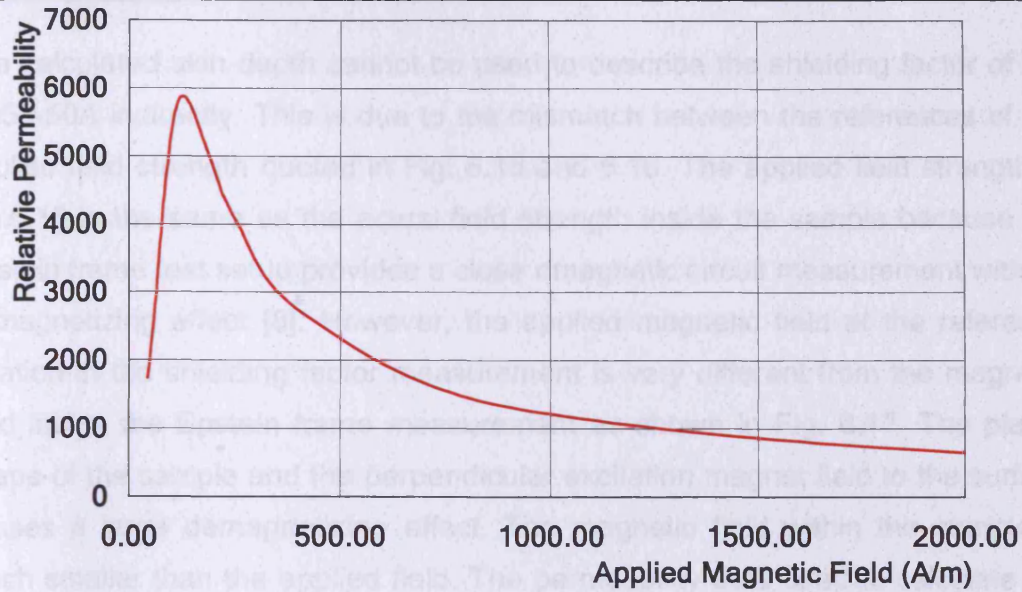


Fig. 6.15. Variation of relative permeability of non-oriented steel M470-50A at 50 Hz with applied magnetic field strength, measured with the standard Epstein frame test [2].

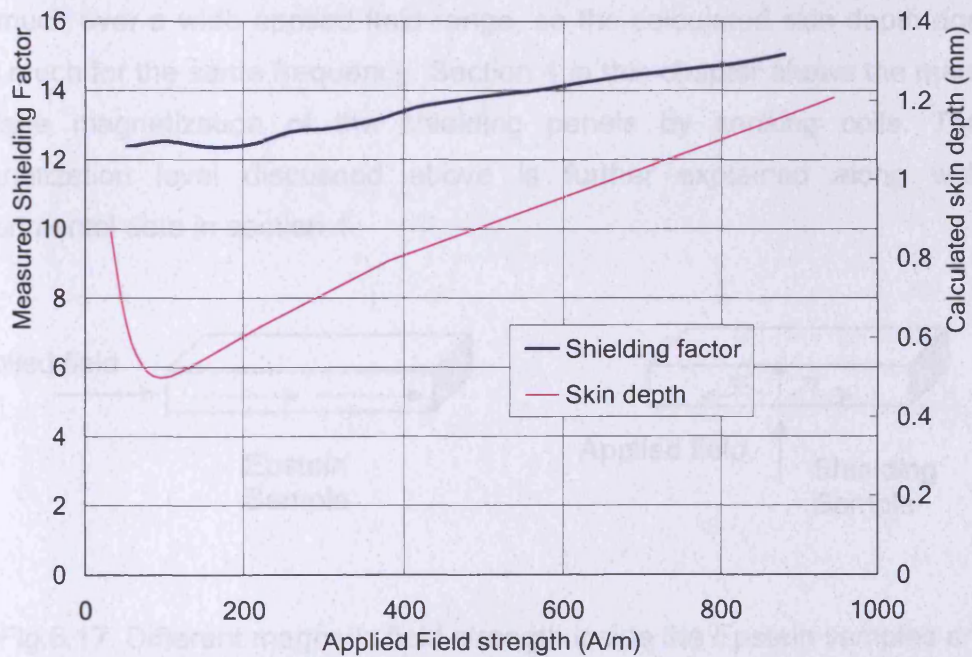


Fig. 6.16. Variation of measured shielding factor and calculated skin depth of non-oriented electrical steel M350-50A at 50 Hz with the applied field strength.

The calculated skin depth cannot be used to describe the shielding factor of the M350-50A indirectly. This is due to the mismatch between the references of the applied field strength quoted in Fig. 6.15 and 6.16. The applied field strength in Fig.6.15 is the same as the actual field strength inside the sample because the Epstein frame test setup provides a close dmagnetic circuit measurement without demagnetizing effect [8]. However, the applied magnetic field at the reference location in the shielding factor measurement is very different from the magnetic field inside the Epstein frame measurement as shown in Fig. 6.17. The planar shape of the sample and the perpendicular excitation magnet field to the surface causes a large demagnetizing effect. The magnetic field within the sample is much smaller than the applied field. The permeability data used to calculate the skin depth cannot be determined from the curve measured from the Epstein frame test. The magnetization level of the sample in Epstein frame test is across a wide range of the applied field, while the permeability falls into the initial permeability region in the shielding samples [9]. The permeability will not change too much over a wide applied field range, so the calculated skin depth does not vary much for the same frequency. Section 4 in this chapter shows the measured in-plane magnetization of the shielding panels by sensing coils. The low magnetization level discussed above is further explained along with the experimental data in section 4.

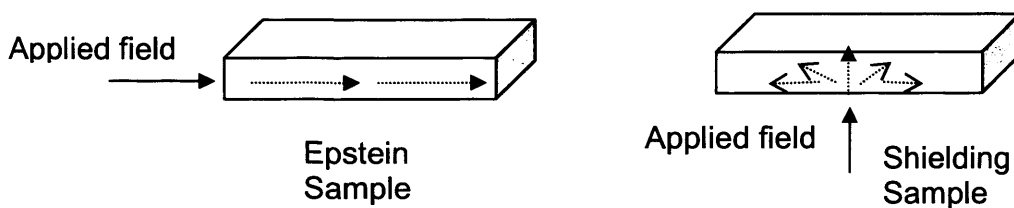
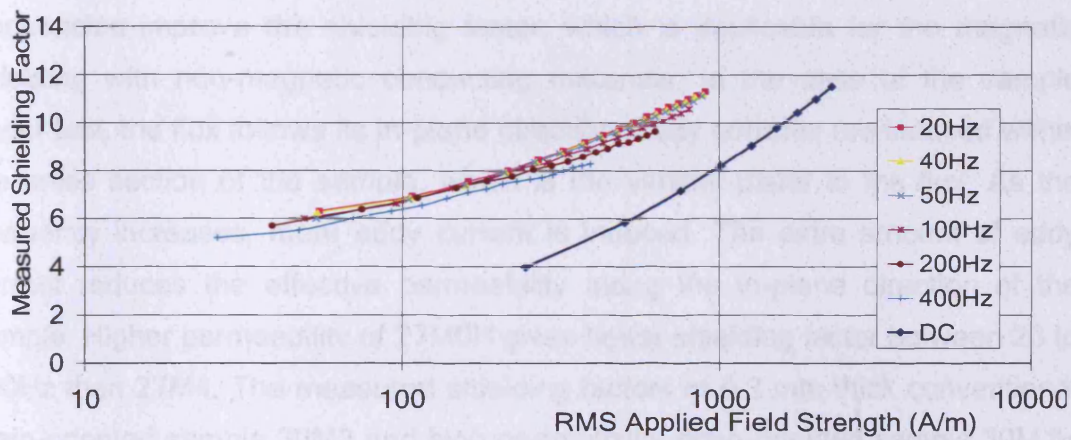


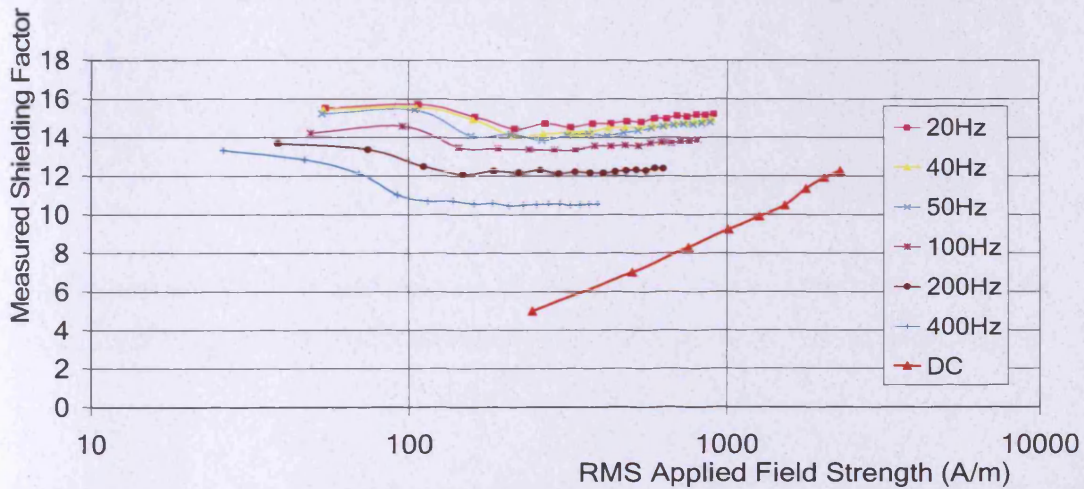
Fig.6.17. Different magnetic field strength inside the Epstein samples and shielding samples due to the demagnetizing effect

Chapter 6. Results and Discussions

A conducting non-magnetic shield has an improved shielding factor with increasing frequency. The shielding factors of conducting magnetic shields, such as electrical steels, are difficult to predict, because the induced eddy current cancellation and flux ducting are both determining factors and cannot be treated separately. Grain-oriented and non-oriented electrical steels samples are measured and the shielding factors from DC, to 400 Hz are presented below. The results at different frequencies are in different field ranges due to the limitation of the field generation at higher frequencies.



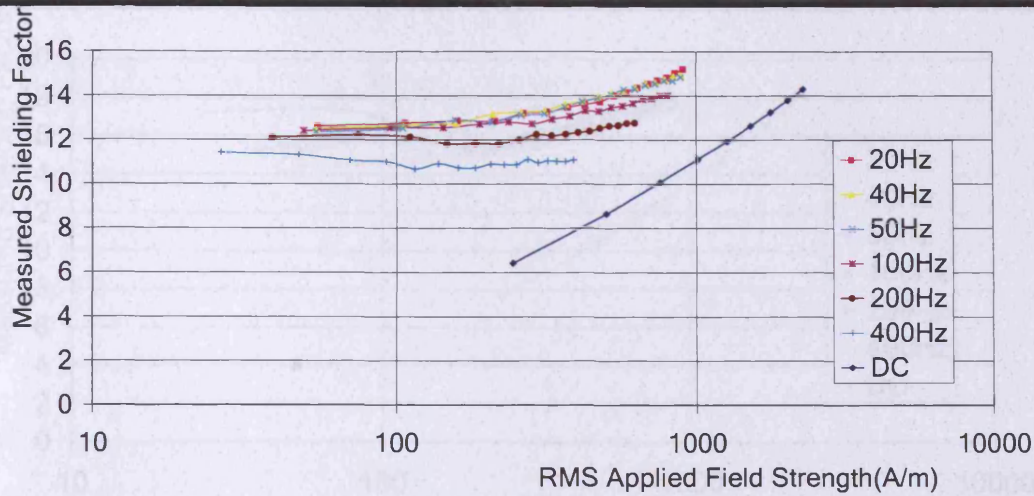
(1). 27M4



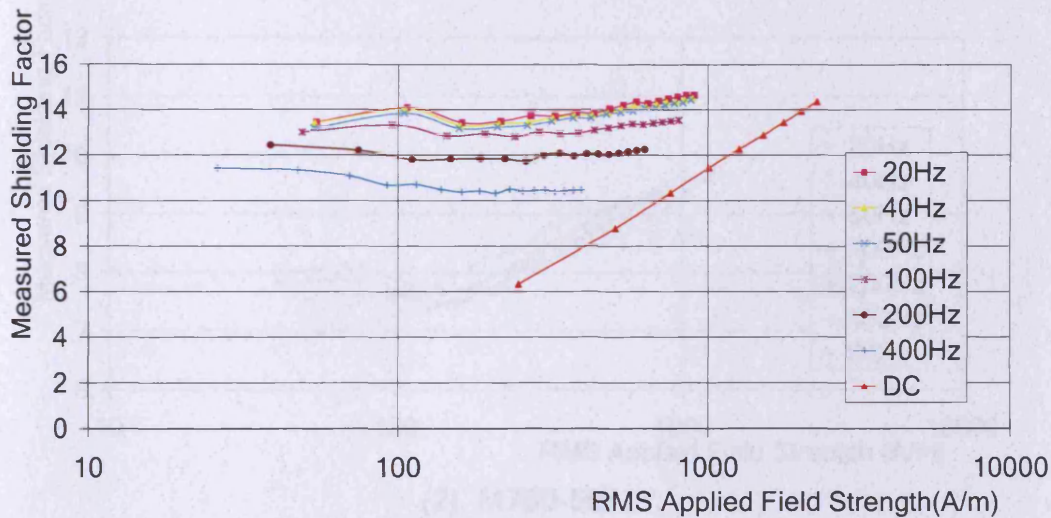
(2). 27M0H

Fig. 6.18. Variations of the measured shielding factors of 0.27 mm thick grain-oriented steel at different frequencies with the applied field strength at the reference location

The AC shielding performance of both samples are nearly doubled than the DC shielding performance. This can be understood as the enhancement from the eddy current cancellation at AC conditions. However, the AC shielding factors are not greatly improved with the increasing frequency for both samples, especially the high permeability sample 27M0H. The trend is very clear from measurements of 27M0H that the AC shielding factor is reduced with increased frequency from 20 to 400 Hz. It does not follow that more eddy currents generated at higher frequencies improve the shielding factor, which is applicable for the magnetic shielding with non-magnetic conducting materials. In the case of the sample under test, the flux follows its in-plane direction. Eddy currents are induced within the cross section of the sample, which is the vertical plane to the flux. As the frequency increases, more eddy current is induced. The extra amount of eddy current reduces the effective permeability along the in-plane direction of the sample. Higher permeability of 27M0H gives better shielding factor between 20 to 400Hz than 27M4. The measured shielding factors of 0.3 mm thick conventional grain-oriented sample 30M3 and high permeability grain-oriented sample 30MJH are presented in Fig. 6.19. The same trend can be found as Fig. 6.18.



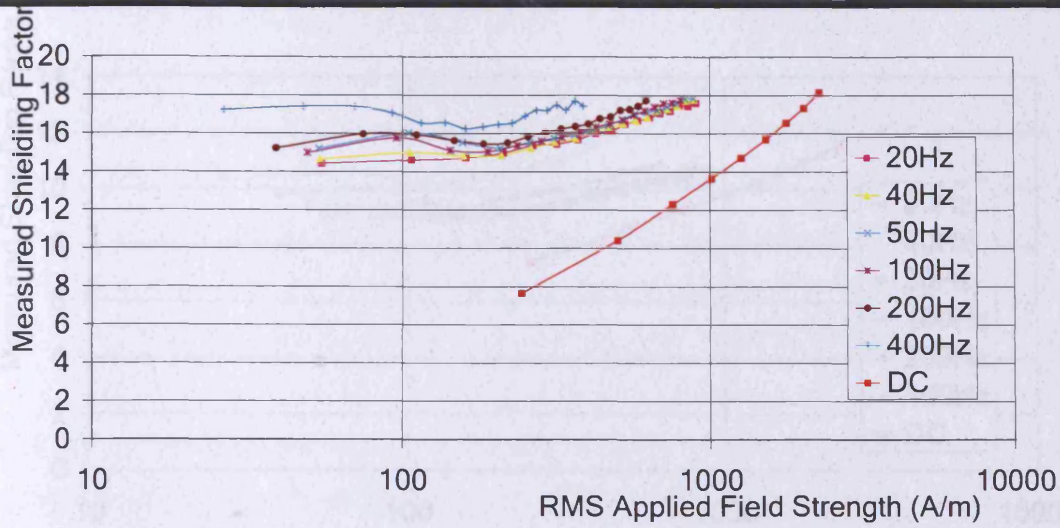
(1). 30M3



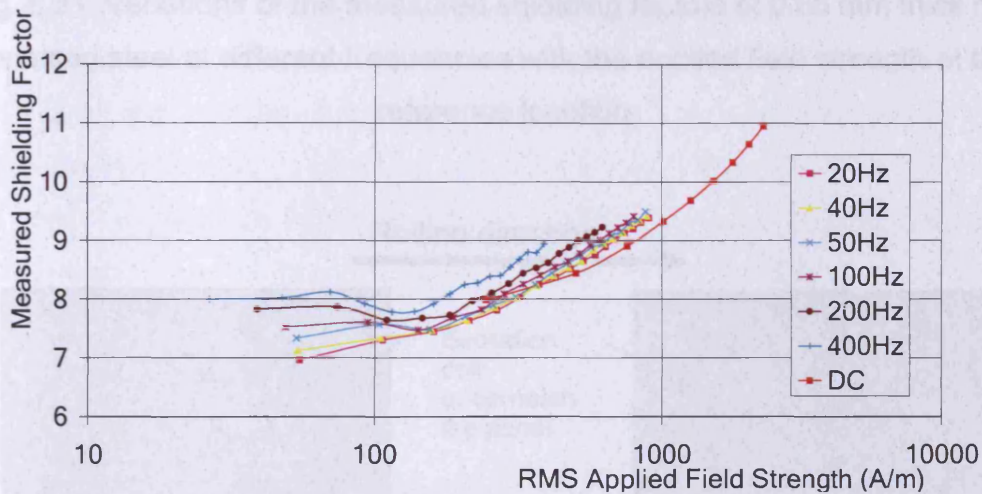
(2). 30MJH

Fig. 6.19. Variations of the measured shielding factors of 0.3 mm thick grain-oriented steel at different frequencies with the applied field strength at the reference location

0.5 mm thick non-oriented samples M310-50A and M700-50A are measured. The results are shown in Fig. 6.20. Although the test rig cannot provide very good sensitivity at the very low applied field range, the shielding factors of both samples improve with increased frequency.



(1). M310-50A



(2). M700-50A

Fig. 6.20. Variations of the measured shielding factors of 0.5 mm thick non-oriented steel at different frequencies with the applied field strength at the reference location

Improved shielding factor with increasing frequency is also found from the test of 0.65 mm thick non-oriented sample M700-65A as shown in Fig. 6.21.

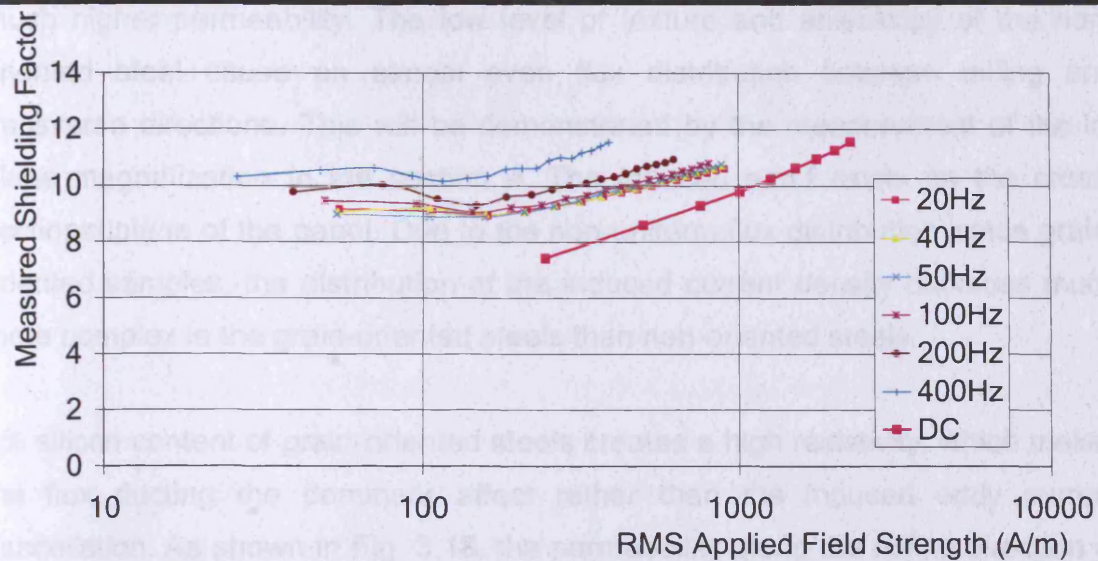


Fig. 6.21. Variations of the measured shielding factors of 0.65 mm thick non-oriented steel at different frequencies with the applied field strength at the reference location

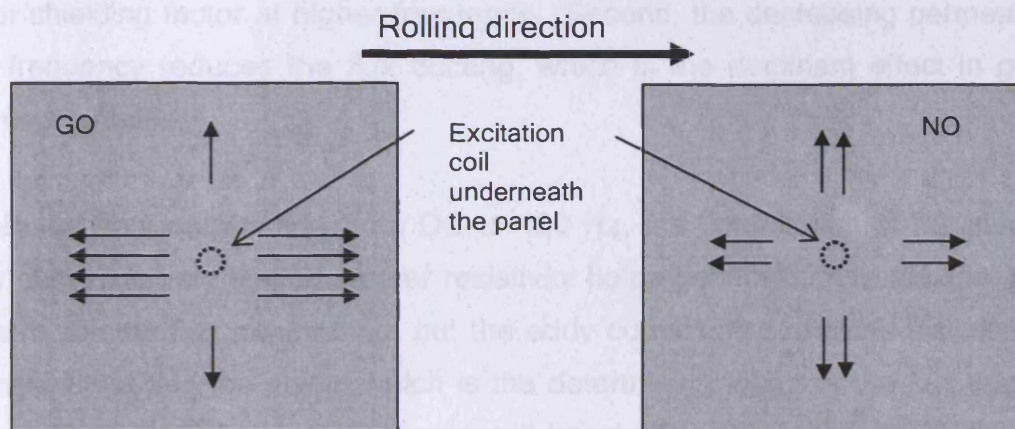


Fig. 6.22. Comparison of the flux distribution along rolling and transverse directions between grain-oriented and non-oriented sample

Fig. 6.22 shows a schematic diagram on the comparison of the flux distribution along rolling and transverse directions between grain-oriented and non-oriented steel panels. Due to the large anisotropy of the grain-oriented steel, rolling direction, which is also the magnetically easy direction, attracts most flux for its

Chapter 6. Results and Discussions

much higher permeability. The low level of texture and anisotropy of the non-oriented steel cause an almost even flux distribution between rolling and transverse directions. This will be demonstrated by the measurement of the in-plane magnetization in the section 4. The induced e.m.f exists on the cross-sectional plane of the panel. Due to the non-uniform flux distribution inside grain-oriented samples, the distribution of the induced current density becomes much more complex in the grain-oriented steels than non-oriented steels.

3% silicon content of grain-oriented steels creates a high resistivity, which makes the flux ducting the dominant affect rather than the induced eddy current cancellation. As shown in Fig. 3.18, the permeability along the rolling direction of grain-oriented steels decreases with increasing frequency. All the above discussion can be summarized as: first, the induced eddy current contributes less in grain-oriented samples than non-oriented samples. The skin depth of non-oriented steel samples decreases with increasing frequency, and then give a better shielding factor at higher frequency. Second, the decreasing permeability with frequency reduces the flux ducting, which is the dominant effect in grain-oriented samples.

Within the frequency range from DC to 400 Hz, the contribution of the induced eddy current is very limited. Lower resistivity helps generate more induced eddy currents to stop flux penetrating, but the eddy current also reduces the effective permeability along the shield which is the determining factor of the flux ducting, especially in the case of grain-oriented steel. Therefore, the resistivity and permeability as the most important material properties for magnetic shielding materials have to be studied at the same time. The study of the flux distribution along rolling and transverse directions of grain-oriented and non-oriented steel is helpful in understanding how in-plane permeability and material resistivity affect the shielding factors. These are covered in section 6.4.

6.4. Flux leakage out of the sample surface and in-plane magnetization

Flux emanates from the surface of the sample under test as shown in Fig. 6.7. The components perpendicular to the sample surface of the field leakage were measured. The test points were positioned as shown in Fig. 6.23. The centre point is along the axis of the excitation coil and the cylinder in the test rig. Beside the centre point, another 20 test points were positioned along rolling and transverse directions with 30 mm gap. The flux leakage from the surface can be used to analyze the capability of the sample in holding the flux. This reflects the shielding performance between different samples if the test condition remains the same. Also the comparison between the flux leakage on the rolling and transverse directions can help understanding how magnetic anisotropic properties of the electrical steels affect the shielding performance.

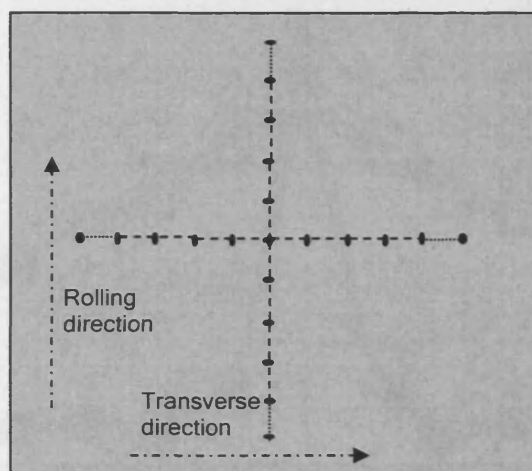
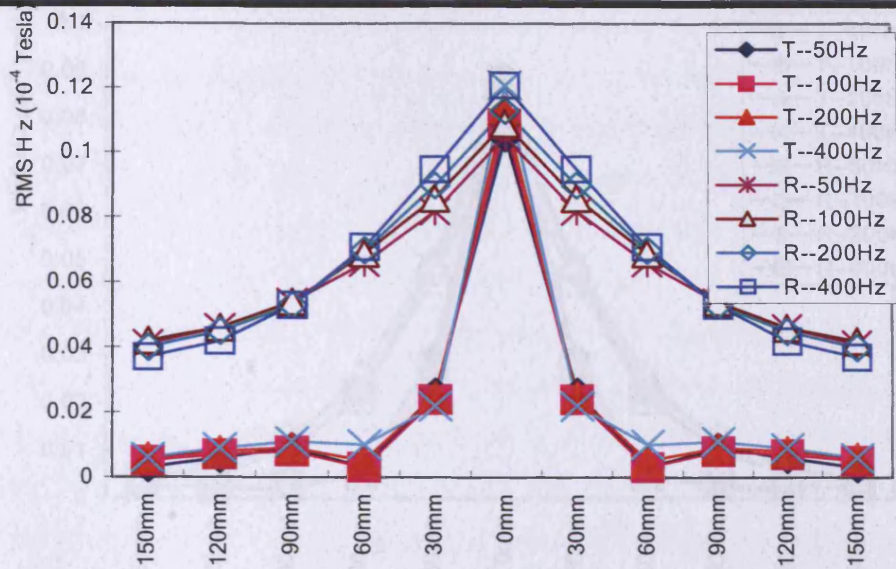
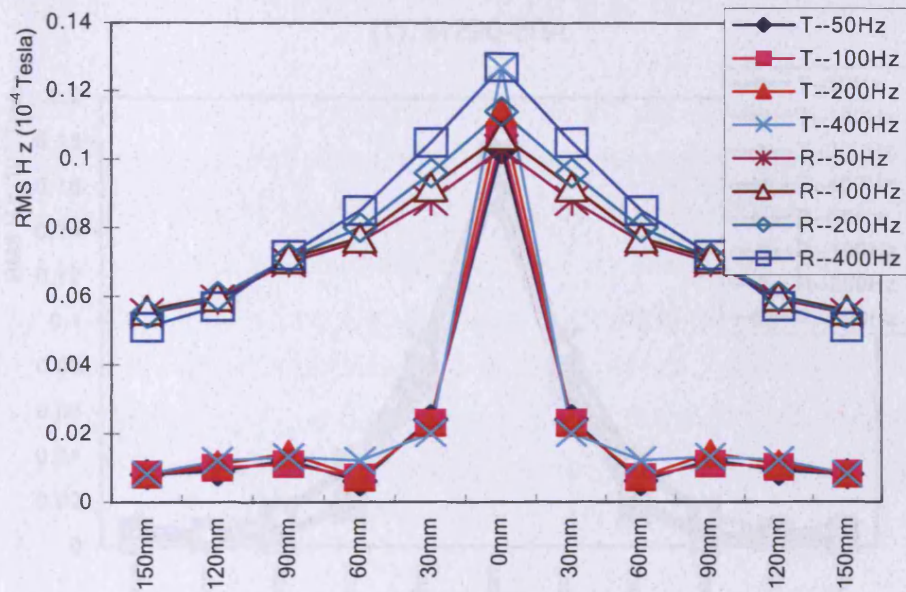


Fig. 6.23. Test points on the sample surface to measure the perpendicular field leakage (H_z) from the sample.

Samples of 30M3, 30MJH, M290-50A and M470-50A were selected for the test. During each test, the applied field was controlled to be 300 A/m. The results for 0.3 mm thick grain-oriented samples 30MJH and 30M3 are shown in Fig. 6.24 and for 0.5 mm thick non-oriented samples M290-50A and M470-50A in Fig. 6.25.

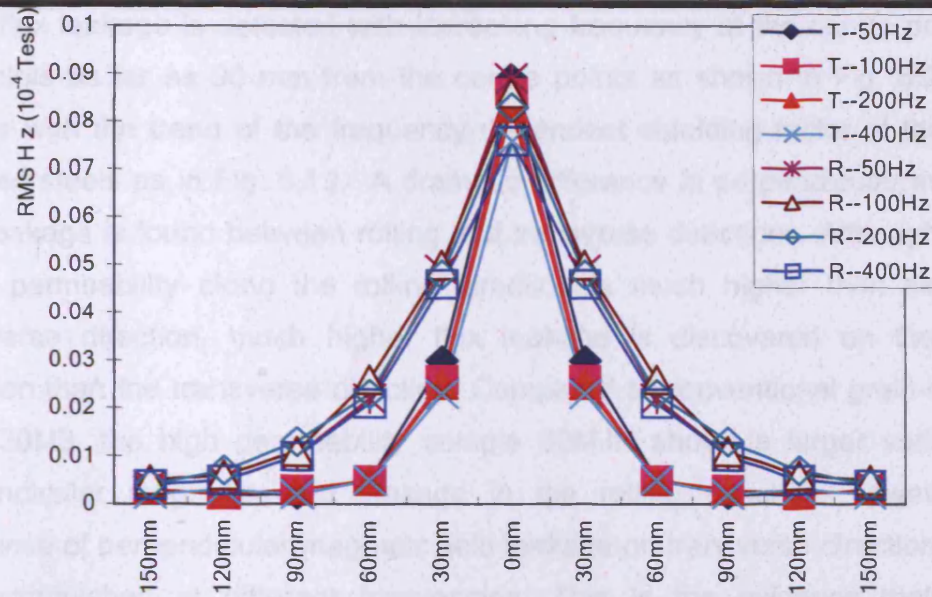


(1). 30M3

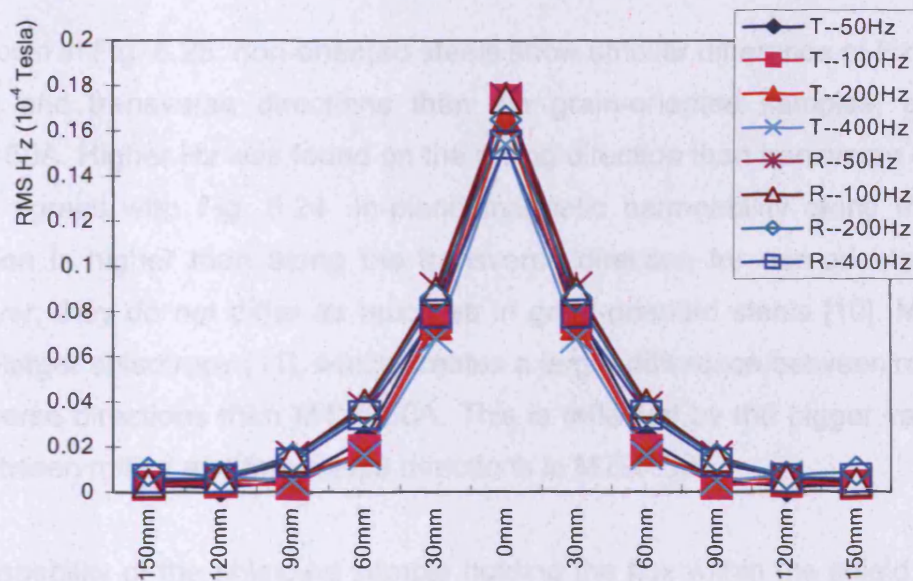


(2). 30MJH

Fig. 6.24. Perpendicular magnetic field leakage (H_z) from surfaces of 0.3 mm thick grain-oriented samples at different frequencies with the distance from the centre of the sample (T: transverse direction, R: rolling direction)



(1). M290-50A



(2). M470-50A

Fig. 6.25. . Perpendicular magnetic field leakage (H z) from surfaces of 0.5 mm thick non-oriented samples at different frequencies with the distance from the centre of the sample (T: transverse direction, R: rolling direction)

Chapter 6. Results and Discussions

More flux leakage is detected with increasing frequency at the centre point and the points as far as 90 mm from the centre points as shown in Fig. 6.24. This agrees with the trend of the frequency dependent shielding factor of the grain-oriented steels as in Fig. 6.19. A dramatic difference in perpendicular magnetic field leakage is found between rolling and transverse directions. Although the in-plane permeability along the rolling direction is much higher than along the transverse direction, much higher flux leakage is discovered on the rolling direction than the transverse direction. Compared to conventional grain-oriented steel 30M3, the high permeability sample 30MJH shows a larger variation of perpendicular magnetic field leakage in the rolling direction, however, the difference of perpendicular magnetic field leakage on transverse direction cannot be distinguished at different frequencies. This is the evidence that higher permeability makes shielding factor more sensitive to increasing frequency.

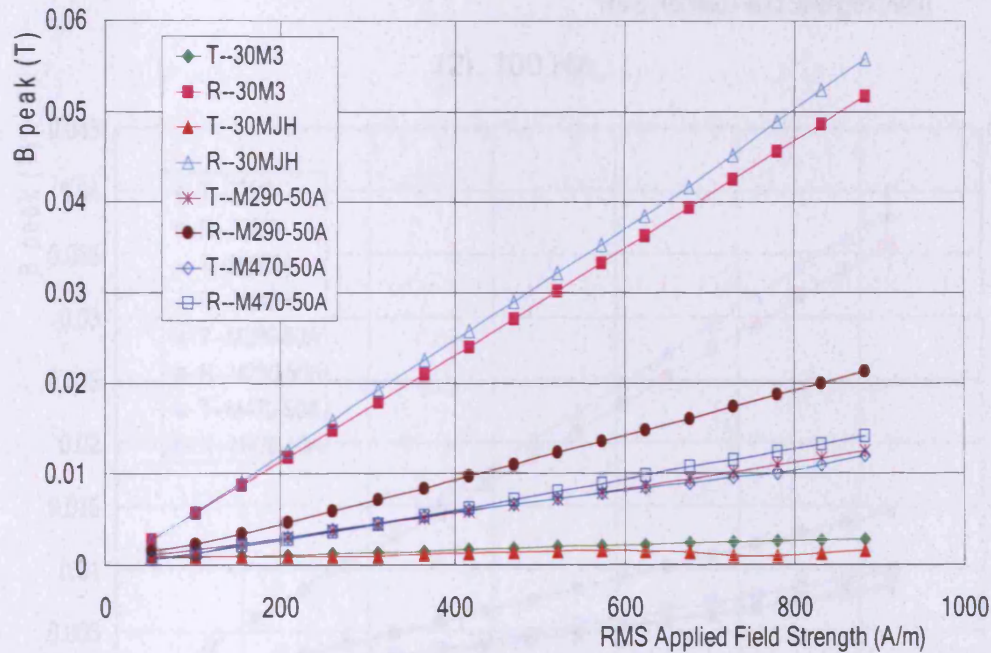
As shown in Fig. 6.25, non-oriented steels show smaller difference of Hz between rolling and transverse directions than the grain-oriented samples, especially M470-50A. Higher Hz was found on the rolling direction than transverse direction, which agrees with Fig. 6.24. In-plane magnetic permeability along the rolling direction is higher than along the transverse direction for non-oriented steels, however, they do not differ as much as in grain-oriented steels [10]. M290-50A has a larger anisotropy [11], which creates a larger difference between rolling and transverse directions than M470-50A. This is reflected by the bigger variation of Hz between rolling and transverse directions in M290-50A.

The capability of the shielding sample holding the flux within the shield depends upon the in-plane permeability and this has been used as the shielding factor of the material by Kubota in 2002[9]. However, the yoke magnetizing method used by Kubota put the material between 0.5 and 1 Tesla which is much higher than the magnetization of the shielding material used for the magnetic shielding rooms. The results are useful but not representative for the real shielding factors.

Chapter 6. Results and Discussions

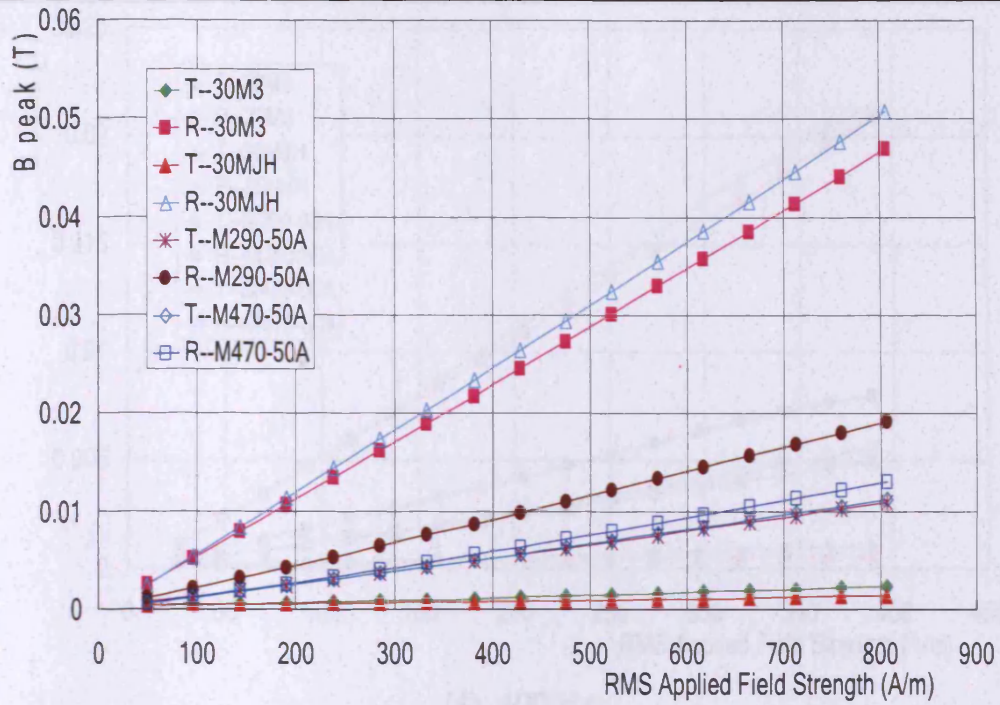
Magnetization along the in-plane direction is studied by fixing sensing coils in the sample. Three 5 mm diameter holes were drilled in the sample and 10-turn coils were wound as shown in chapter 5 (Fig. 5.23) to measure flux density inside the sample. The width (200 mm) of the coil is very large compared to the diameter of the drilled hole, which reduces the error from the damage from the drilling process.

Conventional 0.3 mm thick (30M3) and high permeability (30MJH) grain-oriented steels were tested at different frequencies to compare the magnetization along the rolling and transverse directions. Also 0.5 mm thick non-oriented samples M290-50A and M470-50A are tested. The peak magnetization along rolling and transverse directions at 50 Hz, 100 Hz, 200 Hz and 400 Hz are presented in Fig.6.26.

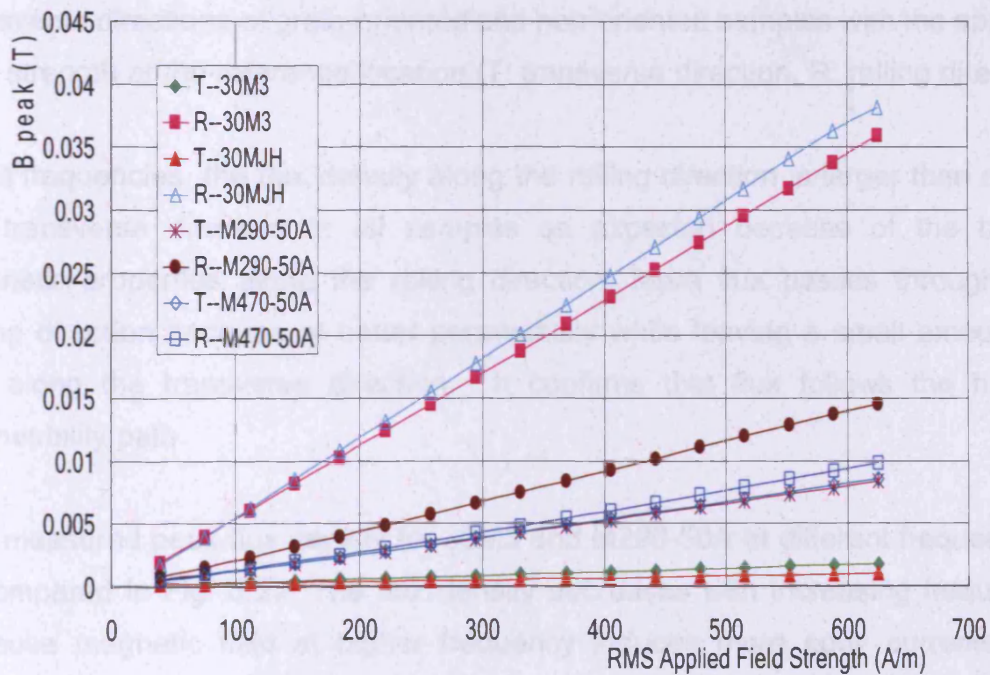


(1). 50 Hz

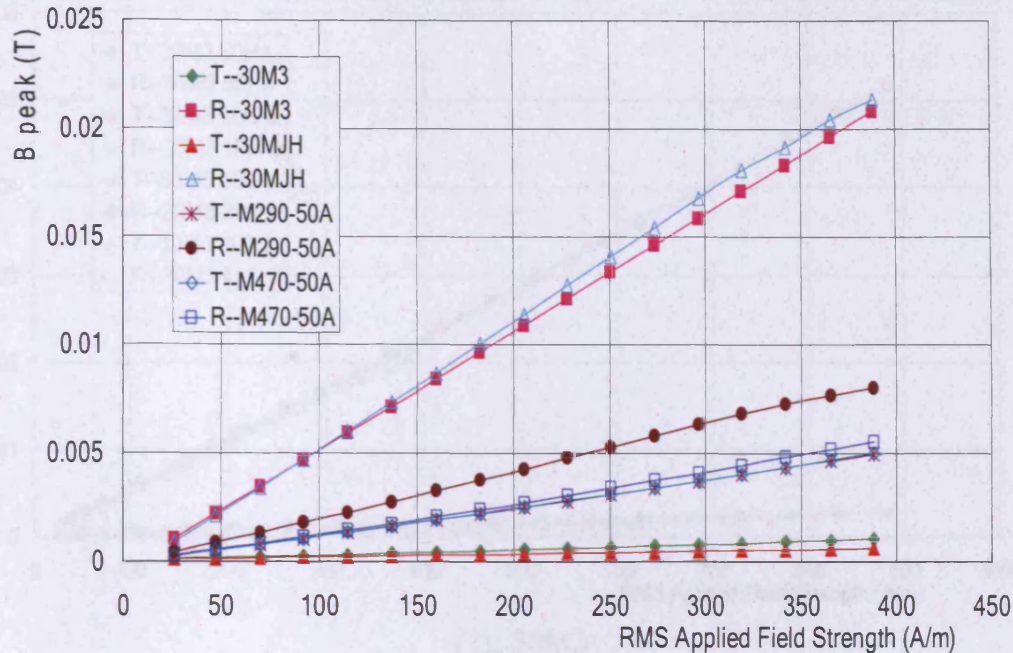
Chapter 6. Results and Discussions



(2). 100 Hz



(3). 200 Hz



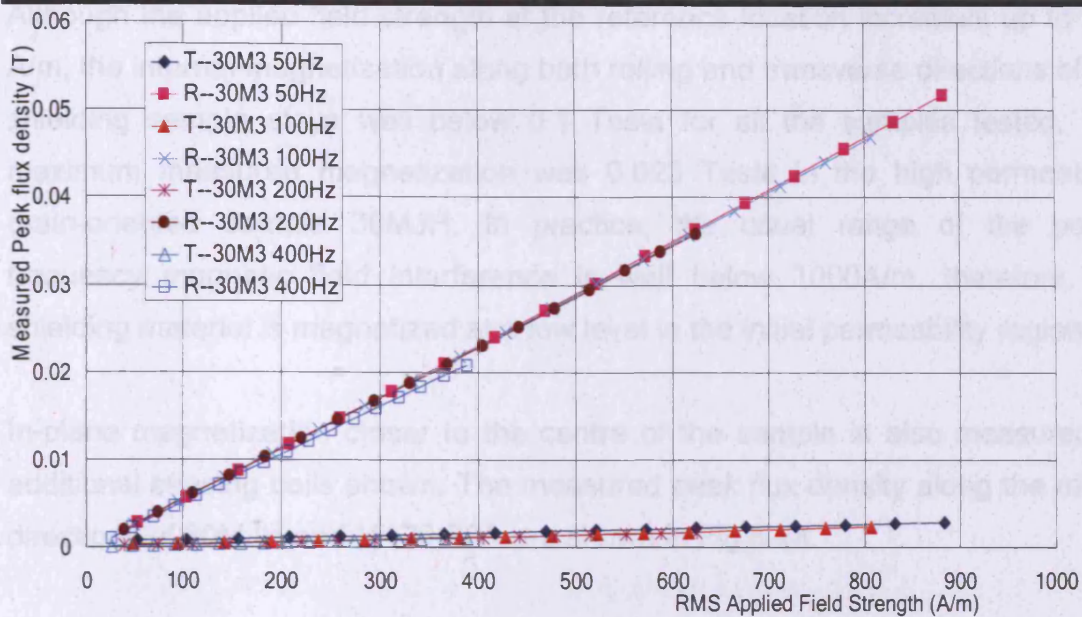
(4). 400 Hz

Fig. 6.26. Variation of measured peak flux density along the rolling and transverse directions of grain-oriented and non-oriented samples with the applied field strength at the reference location (T: transverse direction, R: rolling direction)

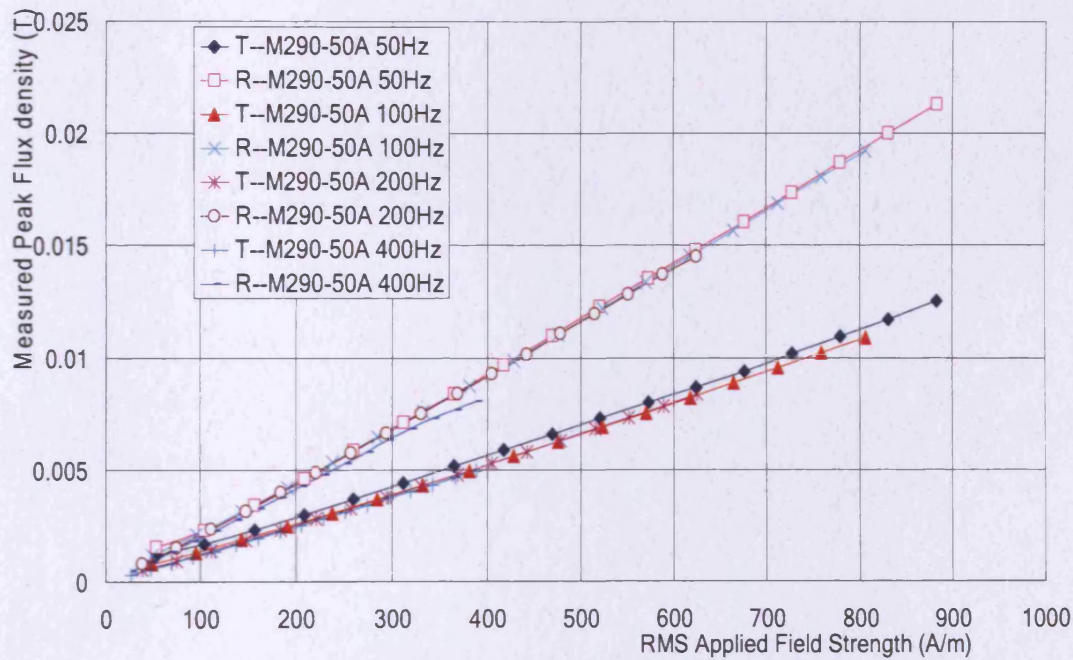
At all frequencies, the flux density along the rolling direction is larger than along the transverse direction in all samples as expected because of the better magnetic properties along the rolling direction. More flux passes through the rolling direction because of better permeability while leaving a small amount of flux along the transverse direction. It confirms that flux follows the higher permeability path.

The measured peak flux density for 30M3 and M290-50A at different frequencies is compared in Fig. 6.27. The flux density decreases with increasing frequency because magnetic field at higher frequency induces more eddy currents are induced at higher frequency along the flux path to reduce the effective permeability.

Chapter 6. Results and Discussions



(1). 30M3



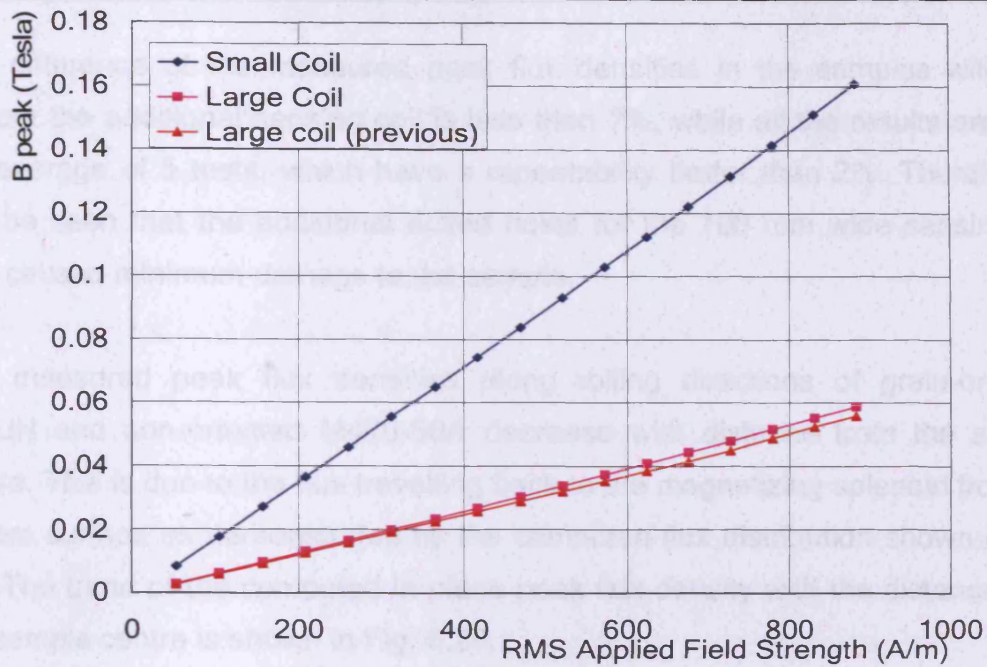
(2). M290-50A

Fig.6.27. Variation of measured peak flux density along rolling and transverse directions of 30M3 and M290-50A at 50 Hz, 100 Hz, 200 Hz and 400 Hz with the applied field strength at reference location (T: transverse direction, R: Rolling direction)

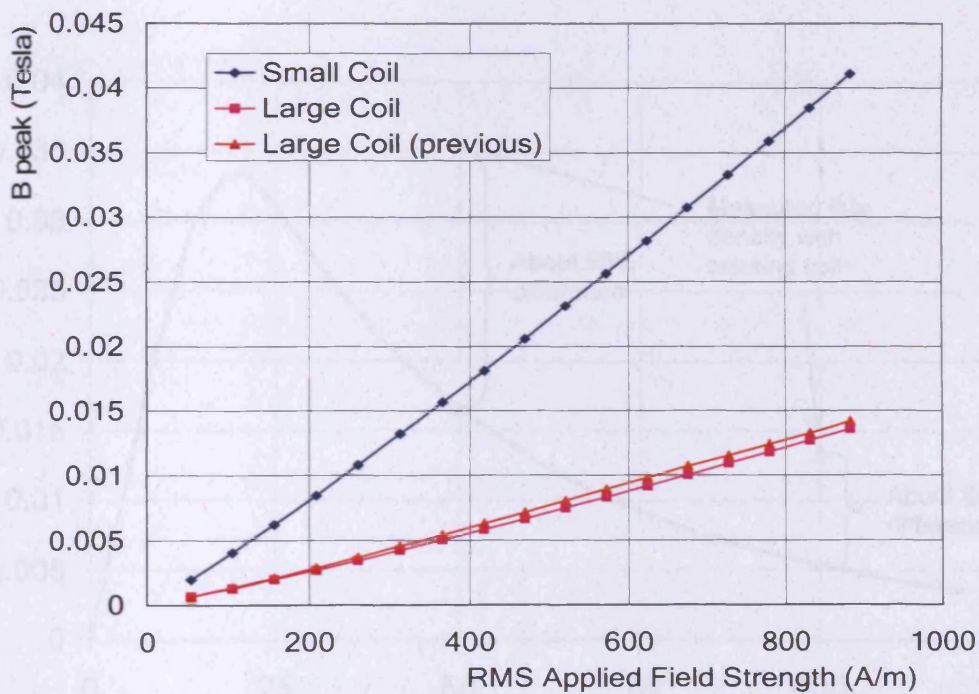
Chapter 6. Results and Discussions

Although the applied field strength at the reference location increases up to 900 A/m, the internal magnetization along both rolling and transverse directions of the shielding sample stays well below 0.1 Tesla for all the samples tested. The maximum measured magnetization was 0.023 Tesla in the high permeability grain-oriented sample 30MJH. In practice, the usual range of the power frequency magnetic field interference is well below 1000A/m, therefore, the shielding material is magnetized at a low level in the initial permeability region.

In-plane magnetization closer to the centre of the sample is also measured by additional sensing coils shown. The measured peak flux density along the rolling directions of 30MJH and M470-50A are shown in Fig.6.28.



(1) 30MJH



(2). M470-50A

Fig. 6.28. Variation of measured peak flux density at 50 Hz along the rolling directions of the sample with the applied magnetic field strength (The 100 mm wide coil is the small one)

The difference of the measured peak flux densities in the samples with and without the additional sensing coil is less than 7%, while all the results are from the average of 5 tests, which have a repeatability better than 2%. Therefore, it can be seen that the additional drilled holes for the 100 mm wide sensing coil only caused minimum damage to the sample.

The measured peak flux densities along rolling directions of grain-oriented 30MJH and non-oriented M470-50A decrease with distance from the sample centre. This is due to the flux travelling back to the magnetizing solenoid from the bottom surface as demonstrated by the computed flux distribution shown in Fig. 6.7. The trend of the computed in-plane peak flux density with the distance from the sample centre is shown in Fig. 6.29.

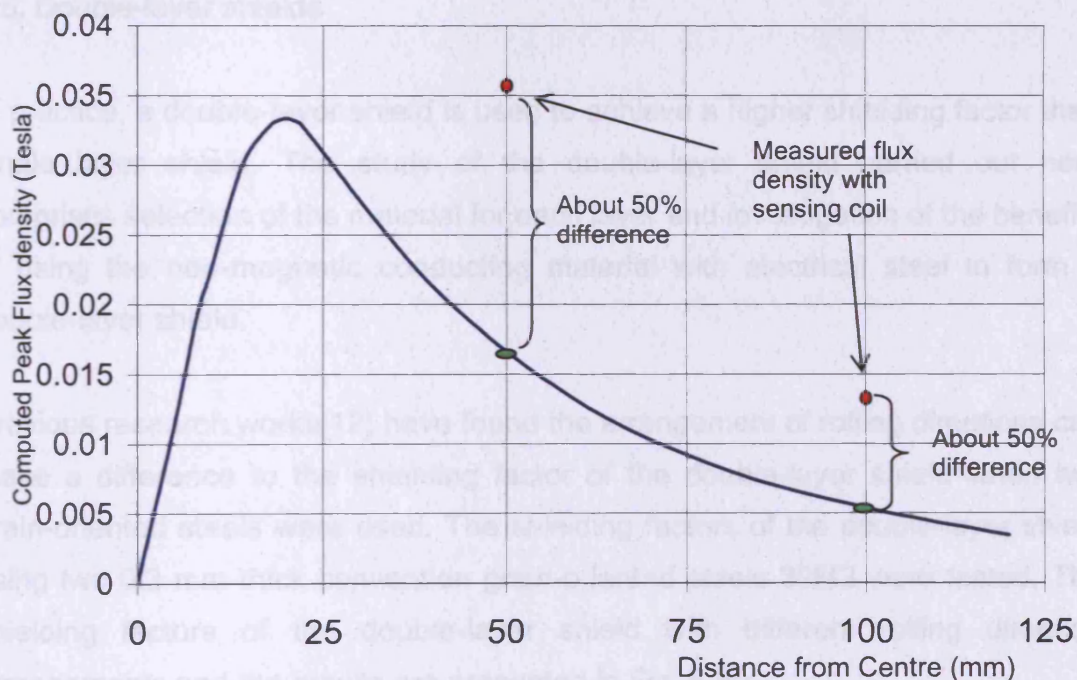


Fig. 6.29. Computed peak flux density along the in-plane direction of M470-50A at an applied field strength of 800 A/m

Chapter 6. Results and Discussions

The difference between the measured peak flux density as shown in Fig. 6.28 (2) and computed peak flux density as shown in Fig. 6.29 along the in-plane direction is as large as 50%. This is due to the error of the solver and potential false data input for the software, which will be discussed in details in section 6.6 of this chapter. It can be seen that the computed peak flux density 50 mm away from the centre is about 3 times of the value at a distance of 100 mm. The same ratio is found from the measured values shown in Fig. 6.28 (2).

The permeability along the perpendicular direction of the sample surface is a key factor in understanding how the magnetic flux penetrates into the sample. However, this permeability is difficult to measure in practice. To correlate the shielding factor with the in-plane permeability, the flux leakage from the sample surface has been studied as above. The in-plane magnetic permeability can be used to describe the capability of shield in restricting the flux inside [9].

6.5. Double-layer shields

In practice, a double-layer shield is used to achieve a higher shielding factor than single layer shield. The study of the double-layer shield carried out here comprises selection of the material for each layer and investigation of the benefits of using the non-magnetic conducting material with electrical steel to form a double-layer shield.

Previous research works[12] have found the arrangement of rolling directions can make a difference to the shielding factor of the double-layer shield when two grain-oriented steels were used. The shielding factors of the double-layer shield using two 0.3 mm thick convention grain-oriented steels 30M3 were tested. The shielding factors of the double-layer shield with different rolling direction arrangements and the results are presented in Fig. 6.30.

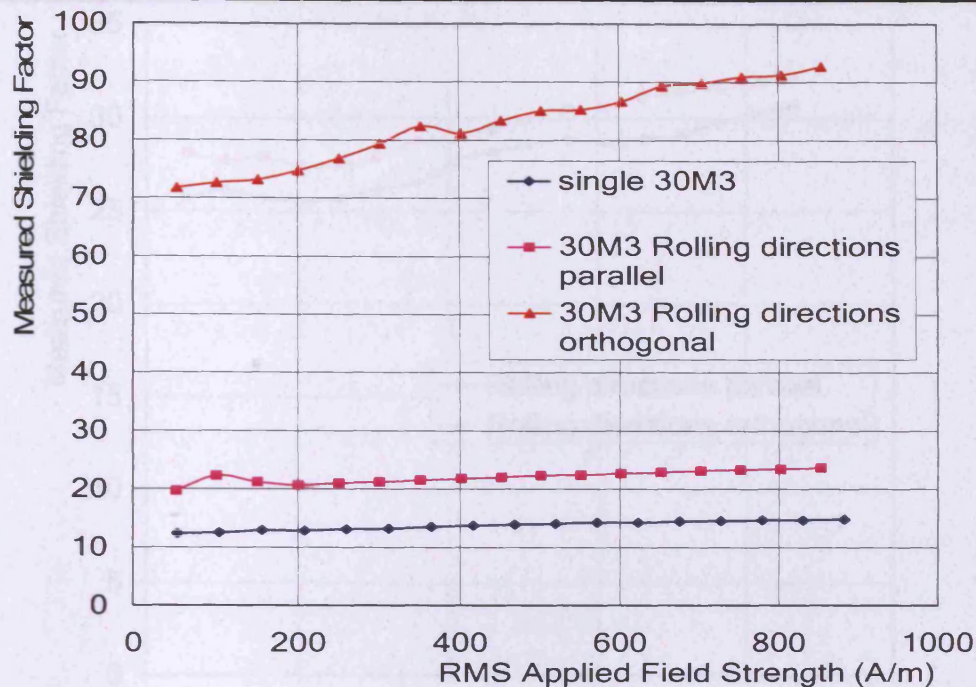


Fig. 6.30. Variation of the measured shielding factors at 50 Hz of single layer 30M3, double-layer with different rolling direction arrangements with the applied magnetic field strength.

The results confirmed that orthogonal rolling directions give a higher shielding factor. The double-layer shield with parallel rolling directions has a higher shielding factor than a single layer of 30M3, but the improved shielding factor is less than double that of the single layer shield. As predicted in previous discussion of the flux leakage from the surface in section 4, different arrangements of the rolling directions of two anisotropic panels can give different shielding factors. Besides the double 30M3 shown in Fig. 6.30, shielding factors of double M290-50A shield is tested and the results are shown in Fig. 6.31.

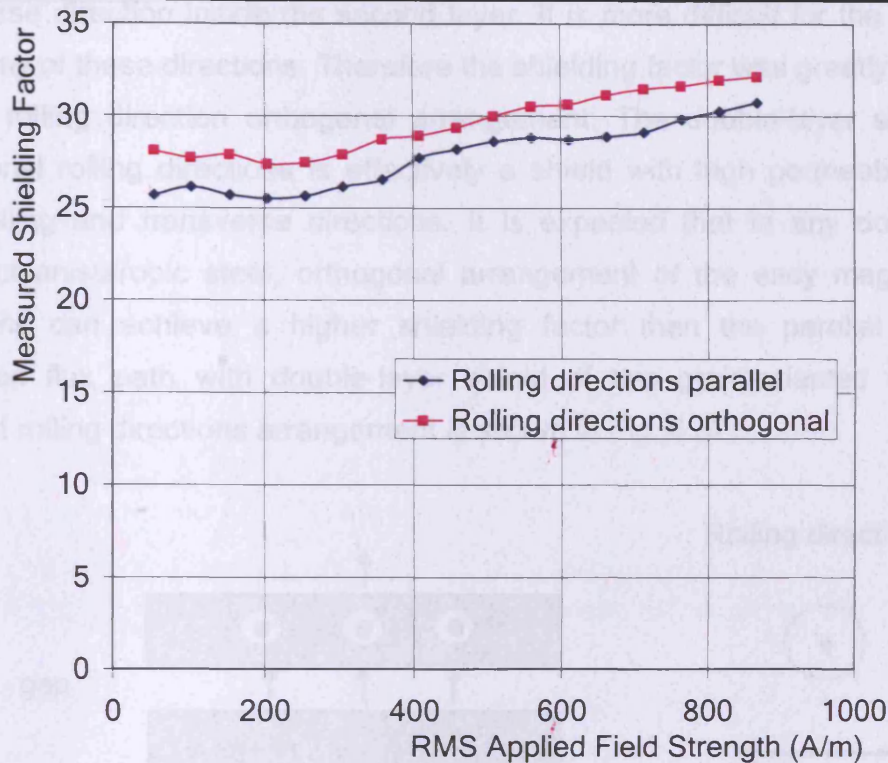


Fig. 6.31. Variations of measured shielding factors of double M290-50A with different rolling directions arrangements at 50 Hz with the applied field strength.

M290-50A is more anisotropic, which is the likely the reason why the shielding factor was improved by the rolling directions orthogonal arrangement.

Fig. 6.26 shows that most flux distributes along the rolling direction in the grain-oriented samples. This distribution causes a much larger field leakage from the sample's rolling direction, which can be seen in (1) and (2) of Fig. 6.24. In the double-layer 30M3, the flux has to go through both shields to reach the shielded region. If the two layers are arranged as rolling direction parallel, the flux leakage from the first layer shield can easily turn into the second layer and run along the rolling direction inside the second layer. This has an equivalent effect as the increased thickness. However, if the second layer was set as its rolling direction orthogonal to the first layer, the flux or field leakage from the first layer has to either rotate into the rolling direction of the second layer or run along the

transverse direction inside the second layer. It is more difficult for the flux to go along any of these directions. Therefore the shielding factor was greatly improved by the rolling direction orthogonal arrangement. The double-layer shield with orthogonal rolling directions is effectively a shield with high permeability along both rolling and transverse directions. It is expected that in any double-layer shield of anisotropic steel, orthogonal arrangement of the easy magnetization directions can achieve a higher shielding factor than the parallel setup. A simplified flux path with double-layer shield of two grain-oriented steel with different rolling directions arrangement is shown in Fig. 6.32.

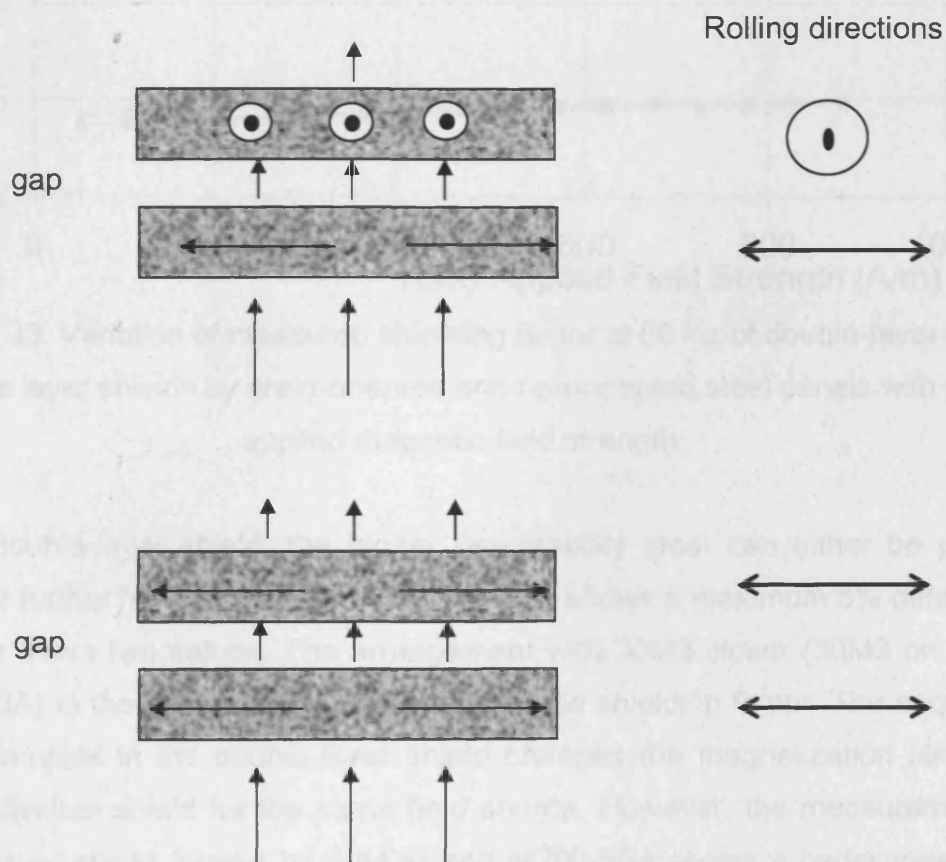


Fig. 6.32. Simplified flux path through double grain-oriented steel shields with rolling directions parallel or orthogonal.

The double-layer shield can also be formed by one grain-oriented and one non-oriented steel. A shield with 0.30 mm thick grain-oriented steel 30M3 and 0.5 mm

thick non-oriented steel M700-50A was tested. The measured shielding factors of the double-layer shield and single shield of either 30M3 or M700-50A are presented in Fig. 6.33.

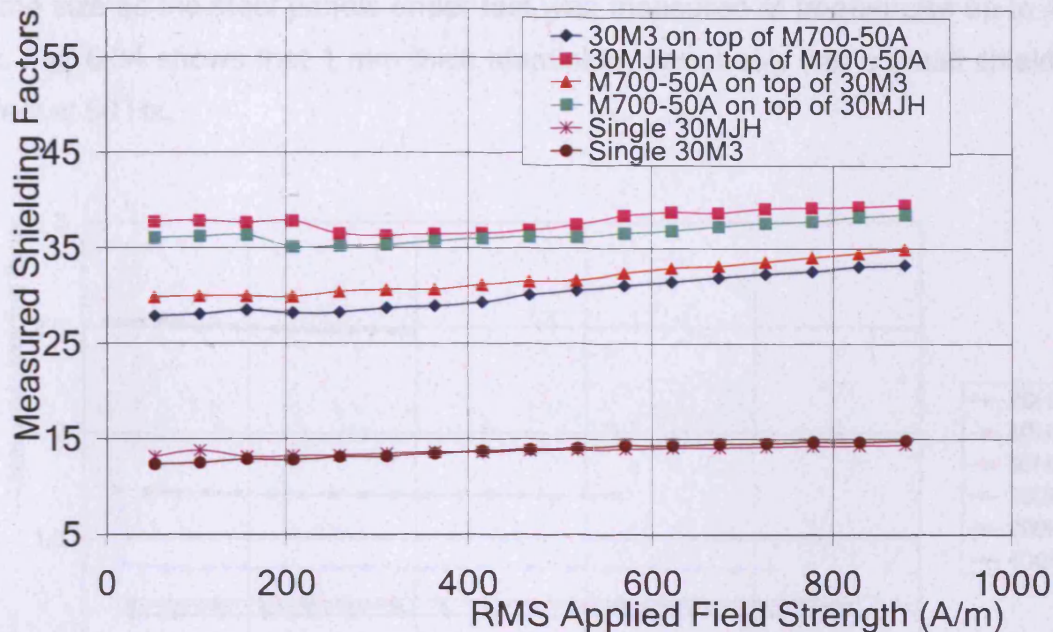


Fig. 6.33. Variation of measured shielding factor at 50 Hz of double-layer and single layer shields by grain-oriented and non-oriented steel panels with the applied magnetic field strength

In the double-layer shield, the higher permeability steel can either be placed closer or further from the field source. Fig. 6.33 shows a maximum 5% difference between these two setups. The arrangement with 30M3 closer (30M3 on top of M700-50A) to the source has a higher measured shielding factor. The sequence of the samples in the double-layer shield changes the magnetization status of each individual shield for the same field source. However, the measurement of double-layer shield formed by 30MJH and M700-50A shows a better measured shielding factor by placing M700-50A closer to the field source. The improvement of the shielding depends on the field source and material properties of each individual shield. It cannot simply draw a general conclusion of the sequence within the double-layer shield formed by one grain-oriented and one non-oriented steel panels.

Another possible combination for a double-layer shield is by electrical steel and conducting material. The shielding factor of a 1 mm thick aluminium panel of the same size as the steel panels under test was measured at frequencies up to 400 Hz. Fig. 6.34 shows that 1 mm thick aluminium panel only has a small shielding effect at 50 Hz.

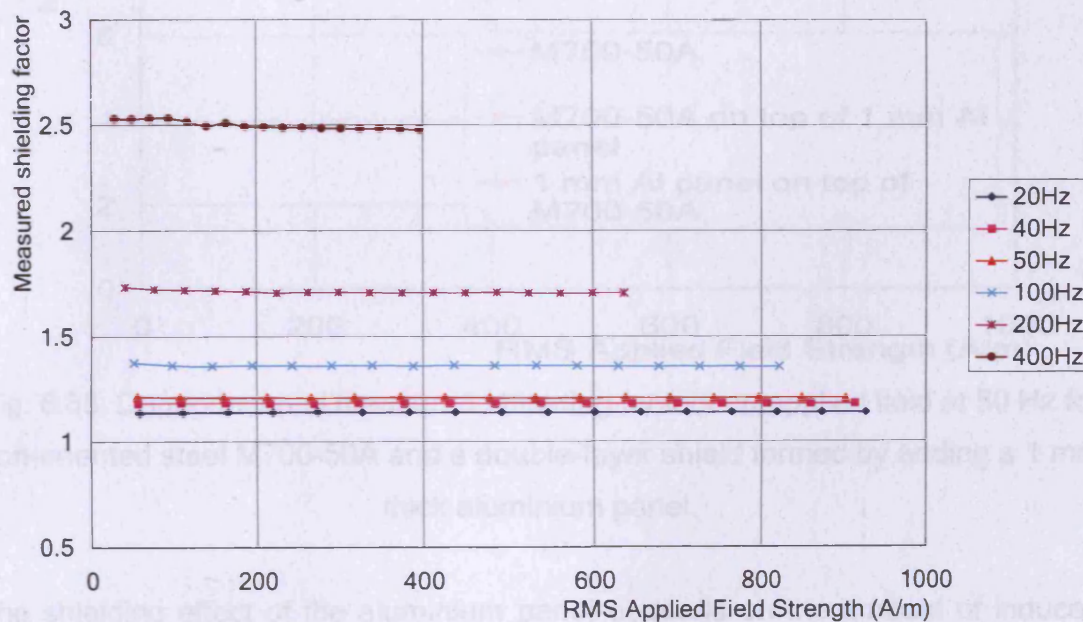


Fig. 6.34. Variation of the measured shielding factor of 1 mm thick aluminium panel at different frequencies with the applied magnetic field strength

Fig. 6.35 shows that adding a 1 mm thick aluminium panel to form a double-layer shield with non-oriented steel M700-50A increases the shielding factor of M700-50A by as much as 20%.

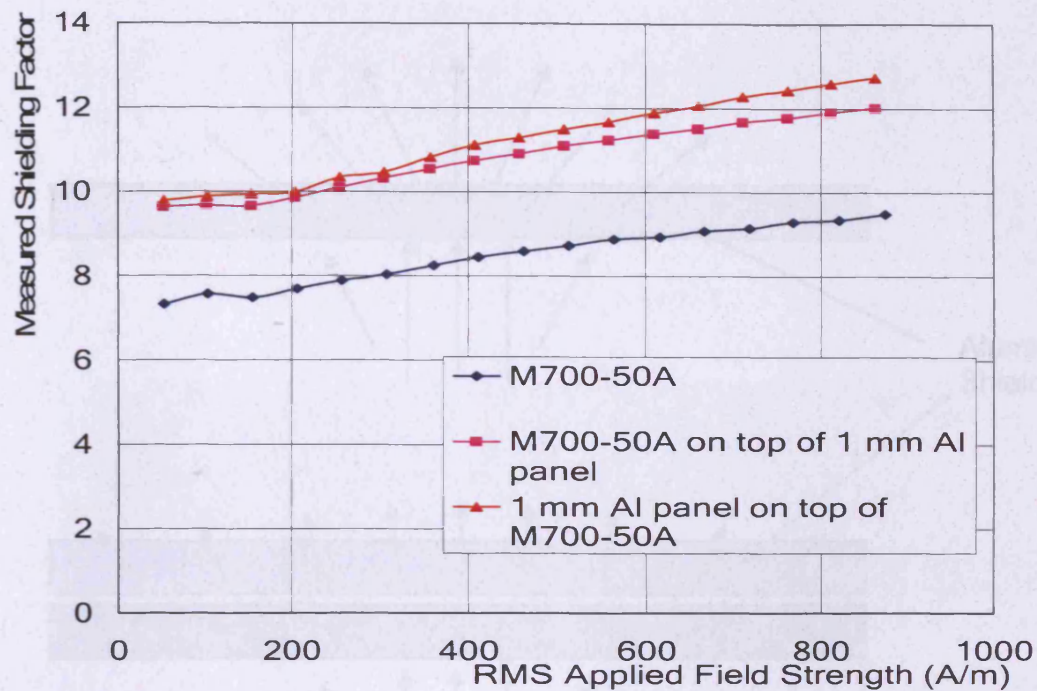


Fig. 6.35. Dependence of measured shielding factors on applied field at 50 Hz for non-oriented steel M700-50A and a double-layer shield formed by adding a 1 mm thick aluminium panel.

The shielding effect of the aluminium panel depends on the amount of induced eddy current because eddy current cancellation is the only shielding mechanism for aluminium shielding. In this test setup, the aluminium panel only provide low shielding because firstly, the applied field has an extremely low frequency; secondly, the magnetic flux is concentrated in a small area just above the excitation coil, so the effective area where the eddy current was generated is very small. After the placement of the electrical steel panel, the leakage flux is spread all over the surface of the steel panel. The amount of flux that penetrates through the shielding of aluminium only and aluminium with M470-50A is presented in Fig. 6.36. The effective area of eddy currents distribution is much lower in aluminium panel alone.

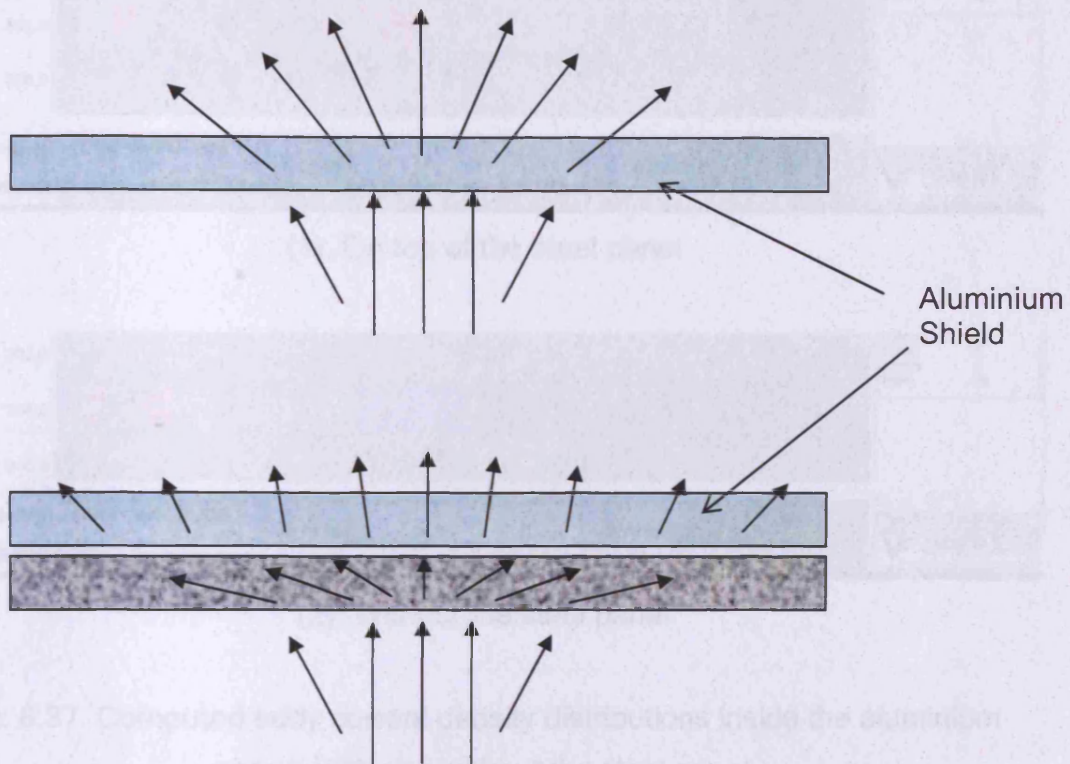
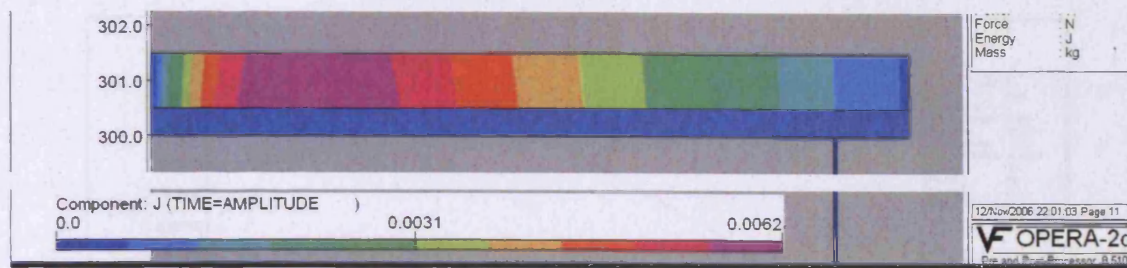


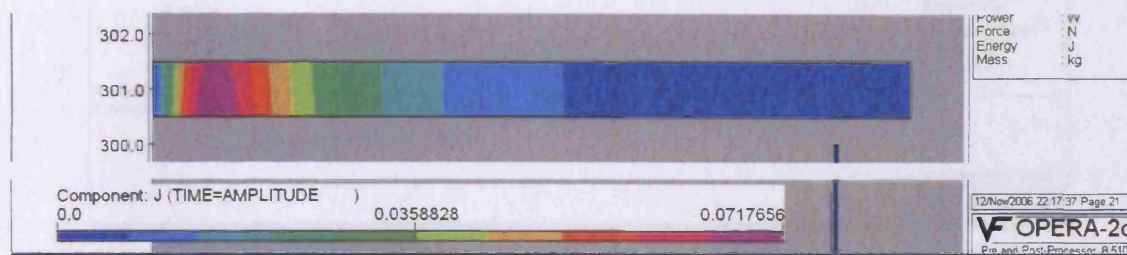
Fig. 6.36. Increased effect area for induced eddy current within the aluminium shield by adding a layer of non-oriented steel M700-50A.

FEM quantitative analysis was carried out using Opera 2D. The computed induced eddy current distributions with and without the steel panel are presented in Fig .6.37. The induced eddy current density along the marked dashed line inside the aluminium panel (shown in Fig. 6.38) is also plotted in Fig. 6.39. It can be seen that the eddy current distribution is much wider in the aluminium panel within the double-layer shielding with M700-50A than when only the aluminium panel is present.

Chapter 6. Results and Discussions



(1). On top of the steel panel



(2). Without the steel panel

Fig. 6.37. Computed eddy current density distributions inside the aluminium panels with and without the steel panel

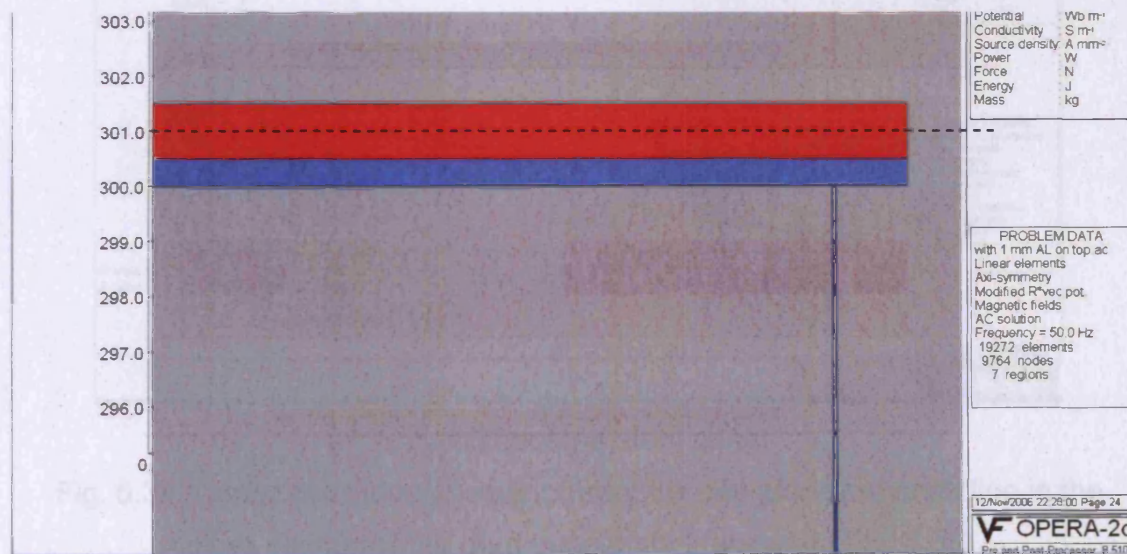
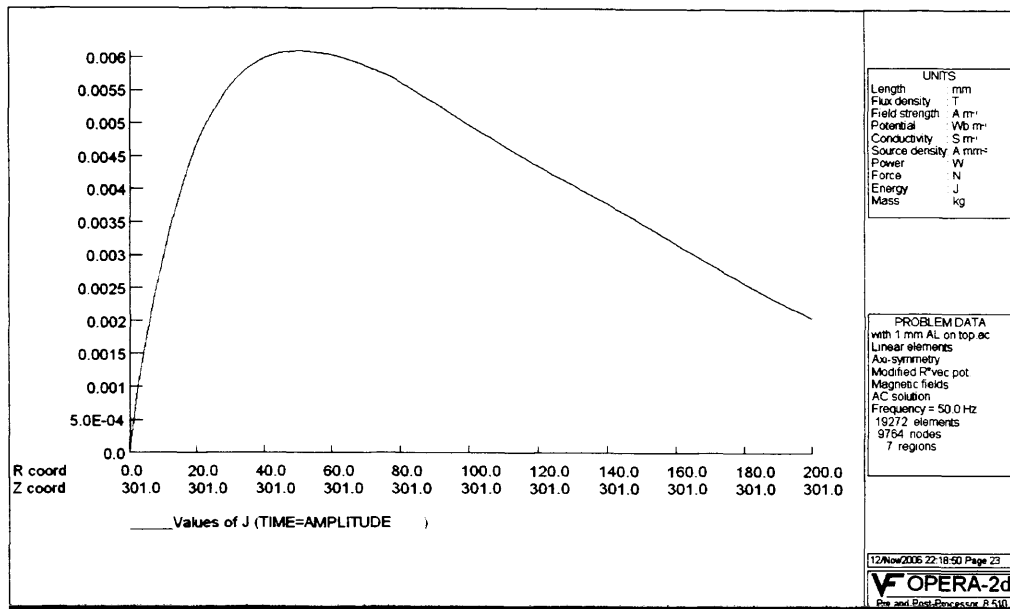
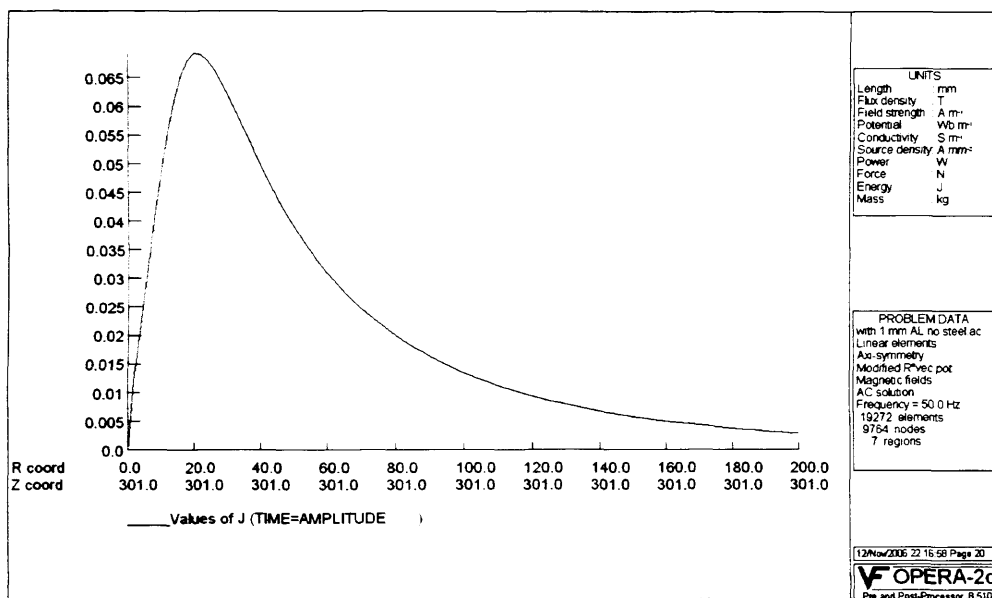


Fig. 6.38. The modelled double-layer shield with aluminium panel (the red) and M700-50A (the blue)

Chapter 6. Results and Discussions



(1). With the steel panel



(2). Without the steel panel

Fig. 6.39. Computed induced eddy current density along the dash line in the cross section of the aluminium panel (shown in Fig. 6.39)

6.6. Degradation of shielding factor by drilled holes on the steel panel

The shielding factor measurements and the factors affecting materials' magnetic shielding have been discussed in the previous sections of this chapter. In this section, practical shielding issues such as the shielding factor degradation by drilled holes and different ways of joining the panels are discussed.

Steel panels assessed in this project are the basic element for the construction of magnetically shielded rooms or enclosures. A typical situation is that panels are drilled and mounted onto the walls to make a room into magnetic shield. In this process, mechanical damage to the samples especially drilled holes are unavoidable. The experimental system developed for assessment of steel panels is also used to assess the degradation of the shielding factor by a drilled hole. A square steel sheet M310-50A is clamped and secured by a timber board and then a high speed steel drill bit is used to drill a 6 mm diameter hole in the middle of the sheet as shown in Fig. 6.40. This arrangement creates the highest degradation of shielding factor due to the hole. The shielding factor was measured before and after drilling. Opera-2d is also used to model the degradation of the shielding factor caused by the hole.

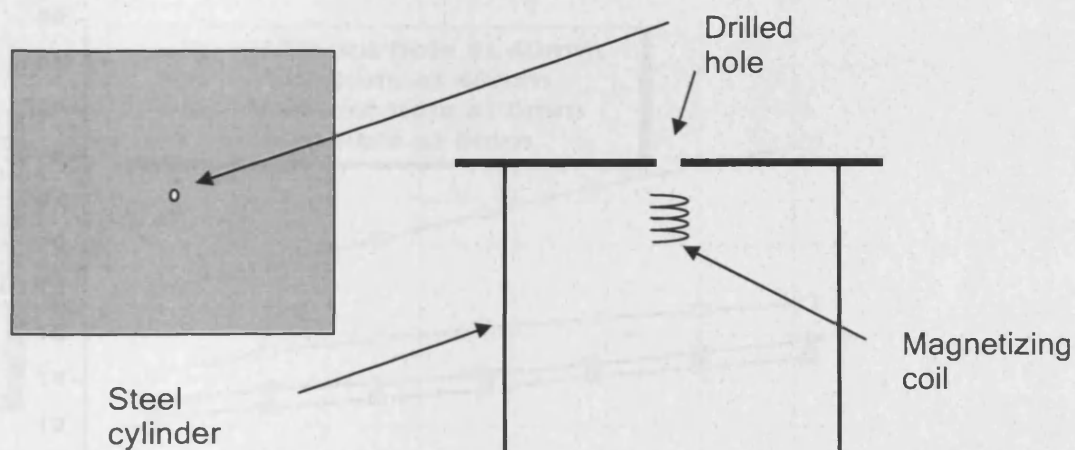


Fig. 6.40. Arrangement of the experiment to assess the shielding factor degradation by a drilled hole in the steel panel

Chapter 6. Results and Discussions

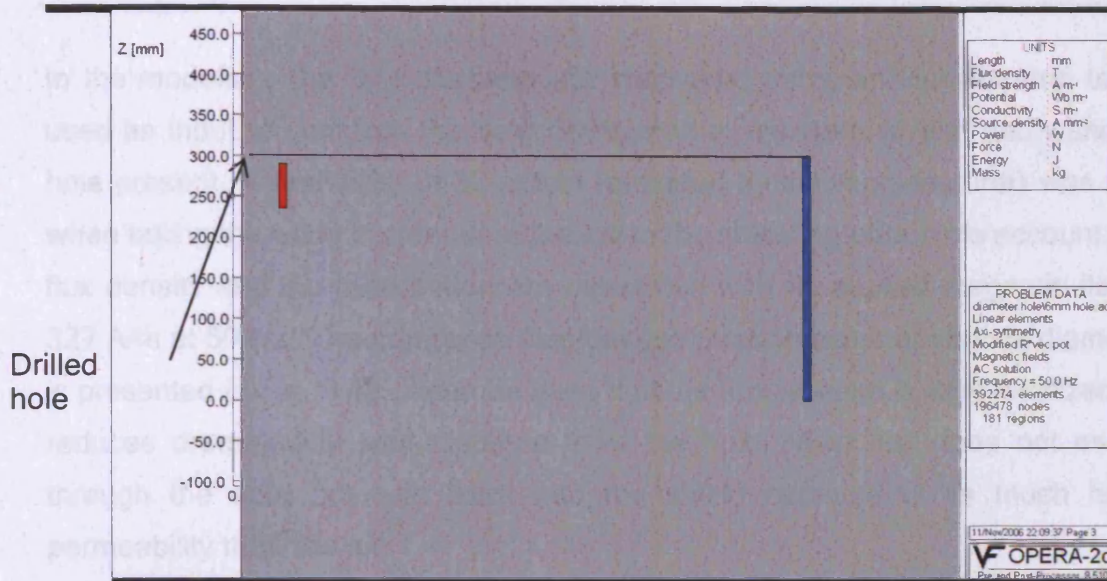


Fig. 6.41. Model constructed in Opera-2d to study shielding factor degradation by a drilled hole

Fig. 6.42 shows the dependence of shielding factor on applied field at the reference point. The shielding factor only falls by 5% at a distance of 40 mm above the sample due to the presence of the hole, but it falls by 25% 5 mm above the sample.

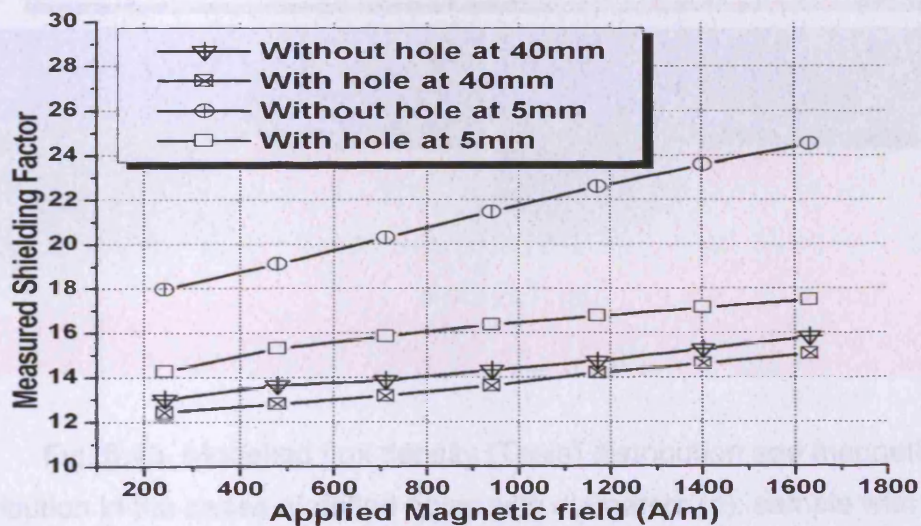


Fig.6.42. Variations of measured shielding factor 5 mm and 40 mm above the samples with and without a 6 mm diameter hole with applied magnetic field

In the modeling, the B-H characteristic measured using an Epstein strip test is used as input to compute the field distribution in the case of with and without a hole present. A resistivity of $52 \mu\Omega\text{cm}$ (provided by the manufacturer) was used when taking the eddy current contribution to the shielding effect into account. The flux density and flux distribution are calculated with an applied magnetic field of 327 A/m at 50 Hz . The computed flux leakage through holes of various diameters is presented in Fig. 6.43. It can be seen that the flux leakage is very localized and reduces dramatically with distance from the hole. Most flux does not escape through the hole but turn back into the shield because of its much higher permeability than the air.

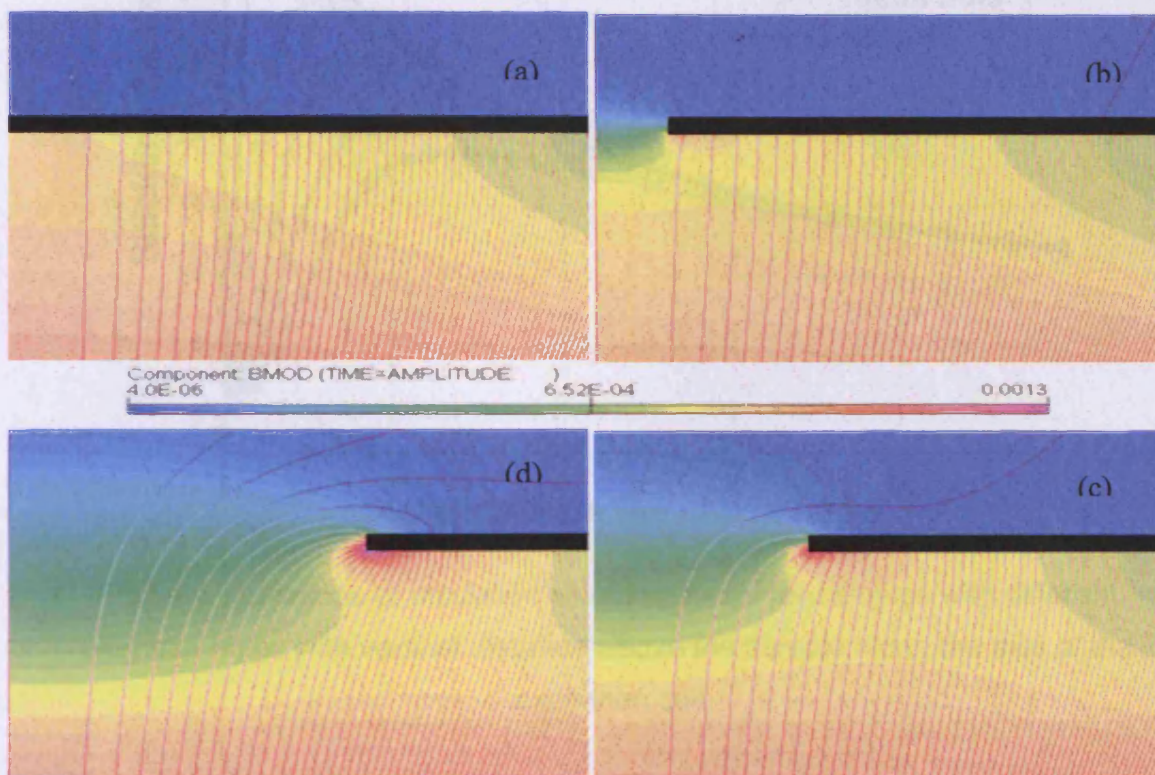


Fig. 6.43. Modelled flux density (Tesla) distribution and magnetic flux distribution in the cases of drilled holes with diameters (a). sample with no hole, (b). 2mm, (c). 6mm and (d). 10mm.

To quantify the effect of the drilled hole on the shielding efficiency of the sheet, shielding factors are calculated from the computed magnetic field strength instead of the measured from the experiments. The variations of the shielding factor with increased diameter of the drilled hole and distance from the sample are presented in Fig.6.44.

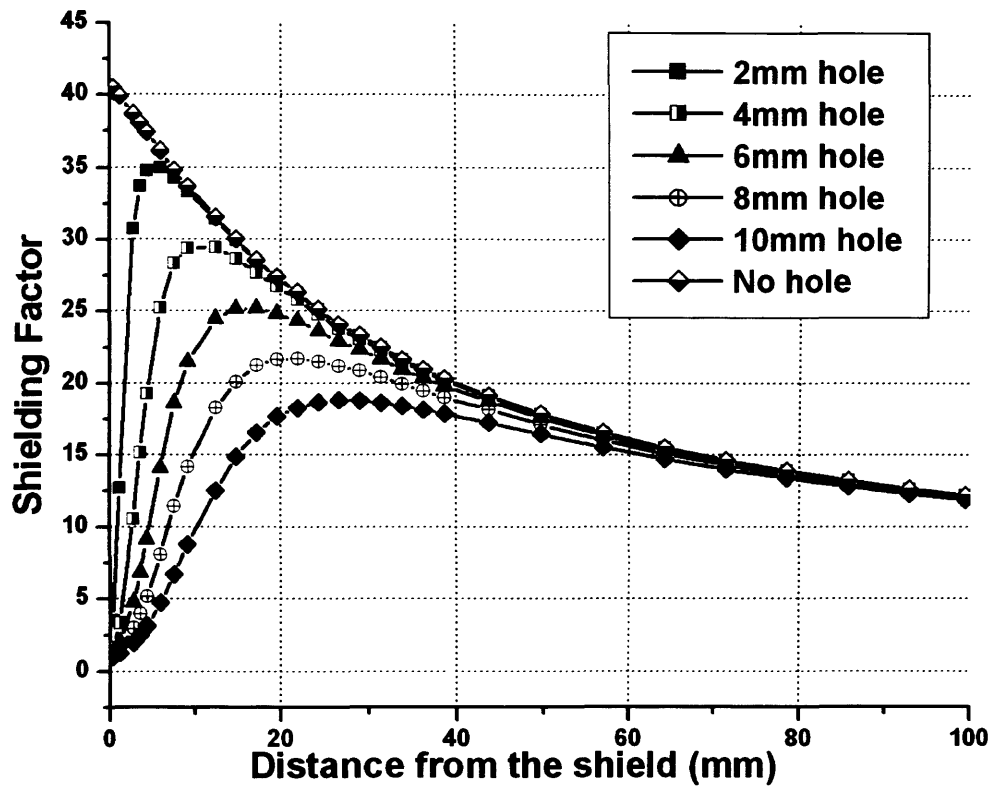


Fig.6.44. Variations of modelled shielding factor for samples with different diameter holes with vertical distance above the sample along the axis of the excitation coil

It can be seen that increasing hole diameter causes a significant reduction of shielding factor near the sample but beyond 70 mm, even the 10 mm diameter hole has no effect. The same trends in shielding factor variation have been found previously in opened type magnetic shielding[12].

Chapter 6. Results and Discussions

Differences as large as 50% between the computed and measured shielding factor can be seen in Fig. 6.45. Besides assumed isotropic material, which contributes to this difference, B-H data used for computation is another reason. As discussed in section 4 of this chapter, small thickness of the sheet results in a very large demagnetizing effect, which limits the sample to very low magnetization and the material is most likely working within the initial magnetization region. Hence accurate definition of initial permeability is a key factor in accurately computing the shielding factor. The possibility of variations of initial permeability even within the same grade[13] indicates that measured data from Epstein strip samples may not be reflecting the property of the shielding sample under test.

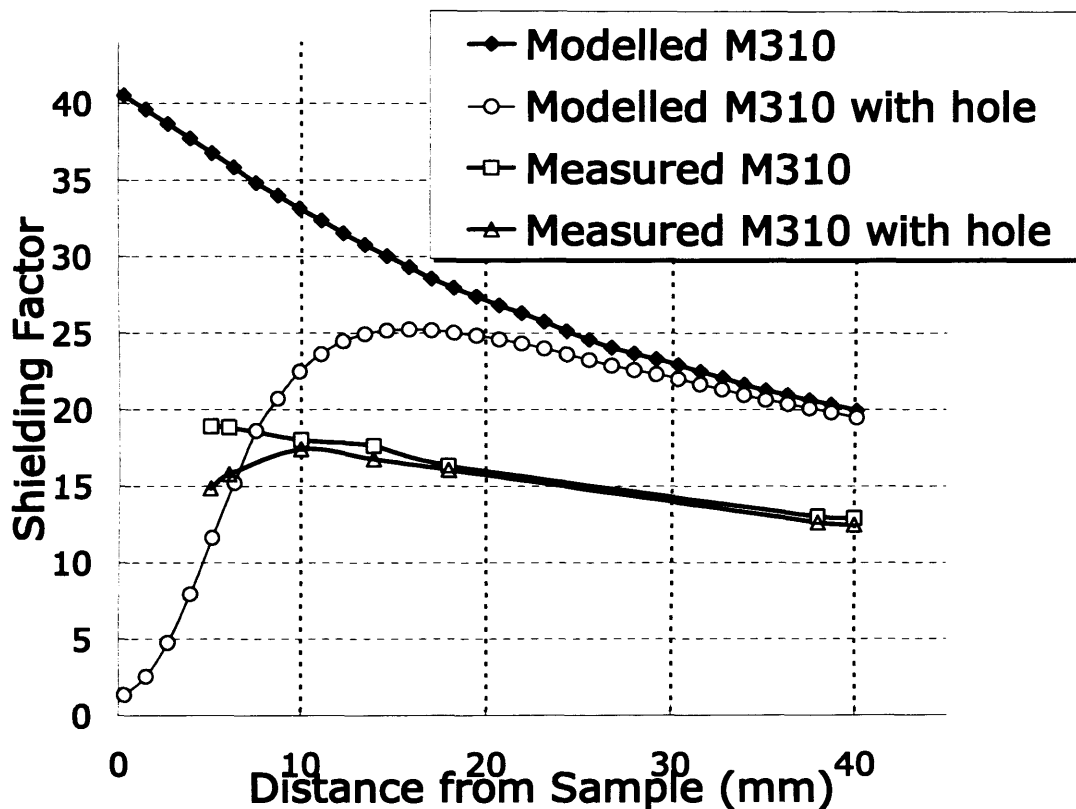


Fig.6.45 Variations of measured and computed shielding factor at different vertical distance above the sample along the axis of the excitation coil

A demonstration of the importance of initial permeability on the computed shielding factor is shown in Fig. 6.46. Only a 13% change of initial permeability

from 1500 to 1700 causes a 10% increase of shielding over the full distance range. A detailed discussion of the deficiency of FEM models is given in section 6.8.

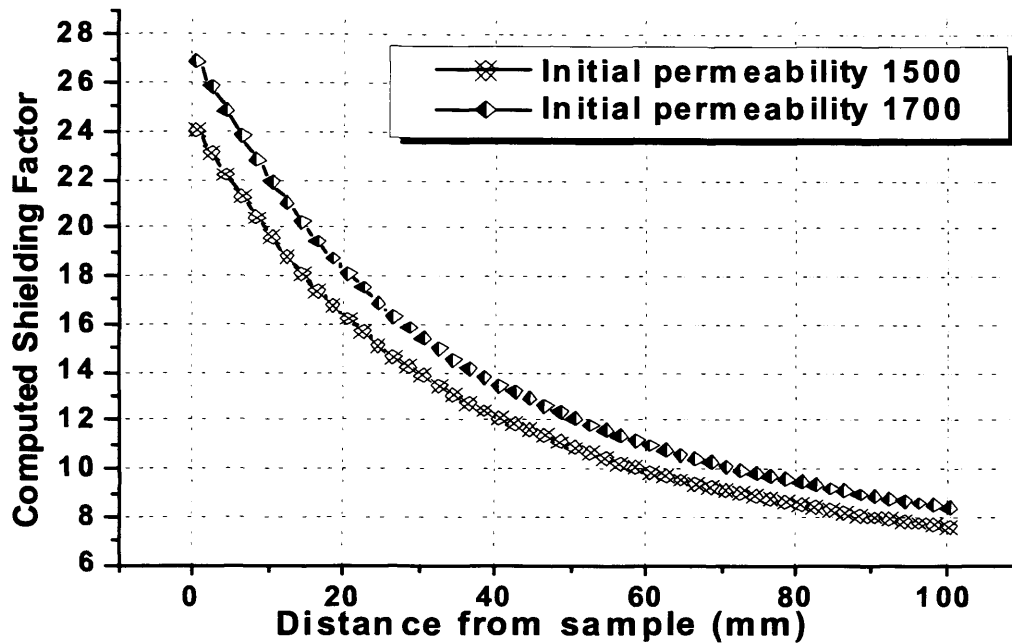


Fig.6.46. Computed shielding factor of materials with two initial permeabilities

Although differences between modelled and measured shielding factor are found because of the difficulty in anisotropic B-H curve modelling of the material and also uncertainty of the value of the inputted initial permeability and effective diameter of the drilled hole. However the trend is very clear from both the modelling and the measurements that the degradation of shielding factor due to a small drilled hole is localized as in this case. Therefore, it is unlikely the drilled holes during the installation of the panels can affect the overall shielding performance of the shielding room.

6.7. Joint between the steel panels and the air gaps between layers

A concern in practical shielding applications is how to join the panels. In high frequency shielding, the electrical continuity of the shield is very important[8]. For magnetic shield at extremely low frequencies, the magnetic continuity of the

Chapter 6. Results and Discussions

shield has to be maintained to reduce the flux leakage. An overlap structure is recommended for the joint between the panels. The overlap can provide a continuous path for the flux and the flux leakage can be reduced in this way. The overlap structure can be tested based on the existing experiment setup. The overlap is placed just above the magnetizing solenoid to create the worst scenario for the flux leakage as shown in Fig. 6.47.

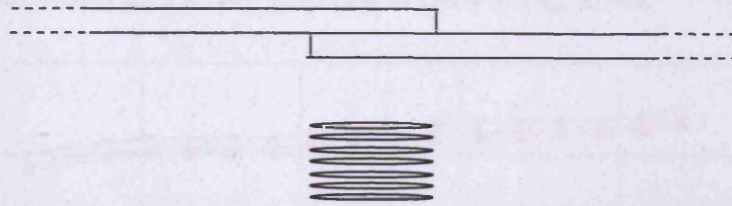


Fig.6.47. Overlap structure placed above the magnetizing coil to create the worst scenario of the flux leakage

Measured shielding factors of the structure shown in Fig. 6.47 with zero, 10 mm and 20 mm overlaps are shown in Fig. 6.48.

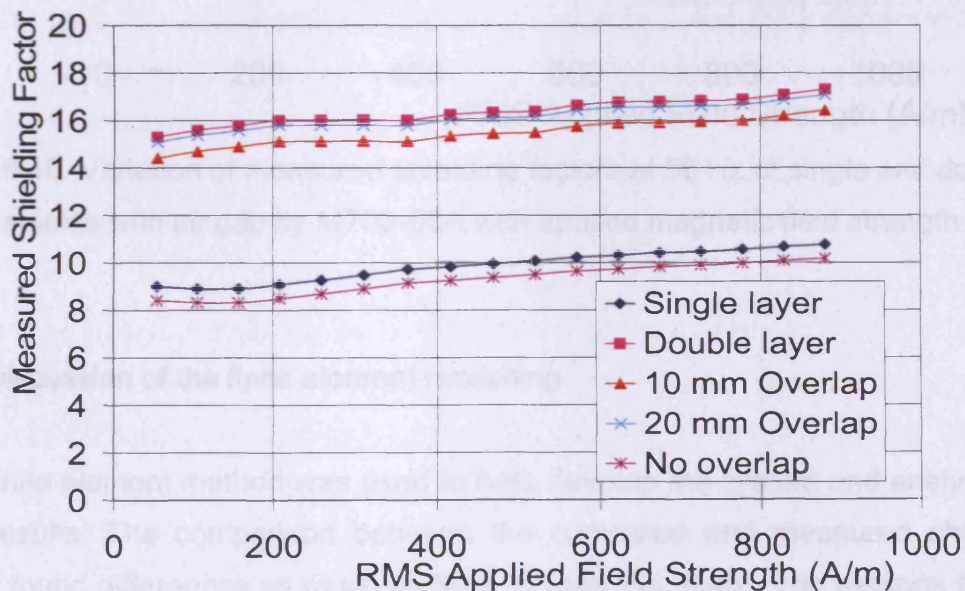


Fig. 6.48. Measured shielding factor at 50 Hz of different overlap setups of non-oriented steel M700-65A with applied field

It can be seen that the shielding factor is dramatically improved by the overlaps. The shielding effect is enhanced by increasing the overlap from 10 mm to 20 mm, in the model the δ -H data was from the measurement carried out in the standard. Air gaps between layers of the multi-layer shield can help improve the shielding factor[1]. This can be studied with this test setup. Double-layer shields of M700-65A were measured and air gaps of 1 mm and 2 mm were introduced by insertion of printing papers. The measured shielding factors of single, double and double-layer shield with 1 mm and 2 mm gap are shown in Fig. 6.49.

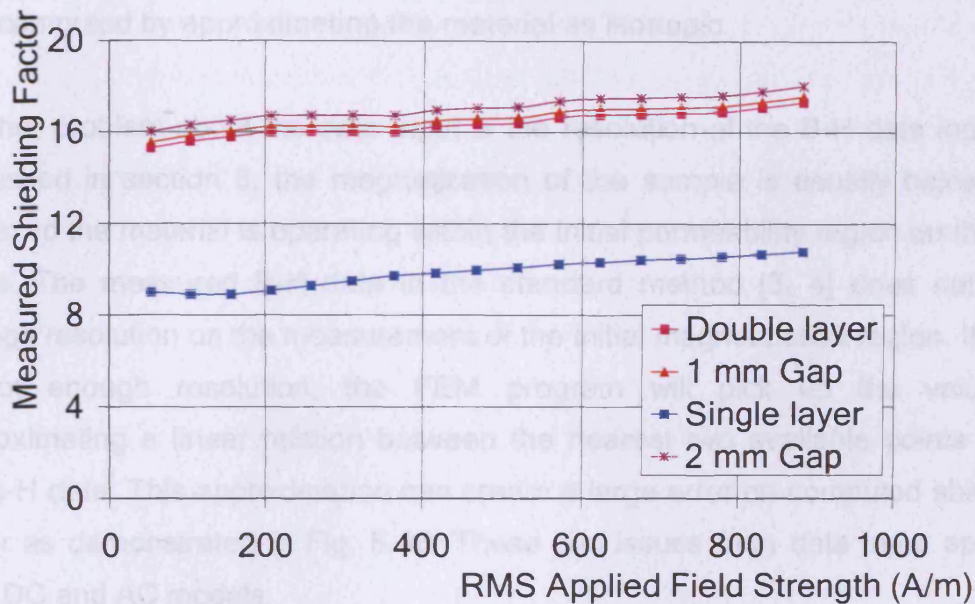


Fig. 6.49. Variation of measured shielding factors at 50 Hz of single and double shields with air gap by M700-65A with applied magnetic field strength.

6.8. Discussion of the finite element modelling

The finite element method was used to help develop the system and analyze the test results. The comparison between the computed and measured shielding factor found differences as much as 50% (shown Fig. 6.45). The reasons for this difference are believed from two aspects.

1. The data input.

In this model, the B-H data was from the measurement carried out in the standard methods[3, 4]. However, the measured B-H data is from the in-plane direction (either rolling direction for grain-oriented or both rolling and transverse direction for non-oriented samples). This data cannot take permeability at other directions in inside the sample. The shielding problem does involve the rotation of the flux after its penetration into the sample as shown in Fig. 6.7. This rotation process was computed by approximating the material as isotropic.

Another problem about the data input is the resolution of the B-H data input. As discussed in section 3, the magnetization of the sample is usually below 0.05 Tesla, so the material is operating within the initial permeability region on the B-H curve. The measured B-H data in the standard method [3, 4] does not have enough resolution on the measurement of the initial magnetization region. If there is not enough resolution, the FEM program will pick up the value by approximating a linear relation between the nearest two available points along the B-H data. This approximation can create a large error on computed shielding factor as demonstrated in Fig. 6.46. These two issues from data input apply to both DC and AC models.

2. The solver

The solver used to process the model under AC condition is a time harmonic solver, which cannot take the hysteresis of ferromagnetic material into account. Although mathematical models such as Jiles-Atherton [13] are available, the time harmonic solver in Opera 2d does not include hysteresis, especially in the 3 dimensional problems.

Chapter 6. Results and Discussions

If applying equation 5.1 to express shielding factor

$$SF = R + A + B \quad (5.1)[14]$$

Where SF is the shielding factor, R represents the contribution by reflection loss, A for material absorption and B for penetration loss.

In magnetic shielding at extremely low frequencies with electrical steels, the reflection loss can be neglected because the shield dimension is usually small compared to the wavelength of the incident field. The penetration loss is from the flux ducting and material absorption is from all the energy consumed by the material such as induced eddy currents and hysteresis loss. The computed shielding factor by the FEM models missed the part of the absorption loss that is the power absorption because of magnetic hysteresis.

References:

1. Rikitake, T., *Magnetic and Electromagnetic Shielding*. Tokyo, Springer, 1987.
2. British Standard, "*BS EN-60404-2: 1998- Methods of measurement of the magnetic properties of electrical steel sheet and strip by means of an Epstein frame*," British Standard Institute, 1998.
3. British Standard. "*Cold rolled non-oriented electrical steel sheet and strip delivered in the fully processed state*," British Standard Institute, 1996.
4. British Standard, "*BS EN 10280:2001-Methods of measurement of the magnetic properties of electrical sheet and strip by means of a single sheet tester*," British Standard Institute. 2001.
5. Moses, A.J., "*Electrical steels: past present and future developments*," *IEE proc. Part-A*, Volume:137, Issue: 5, pp. 233-245, 1990.
6. Cogent Power, Product booklet, Cogent Power Ltd, 2005.
7. Duzer, R., *Fields and waves in communications electronics*, John Wiley and Sons, 1994.
8. Kaiser, K.L., *Electromagnetic Shielding*, CRC press, 2005.
9. Jiles, D., *Introduction to Magnetism and Magnetic Materials*. Second edition, New York, Chapman&Hall, 1997.
9. Kubota, T., "*Recent progress on Electrical steel sheet for Eco-design of electrical equipment*," *21st annual conference on Properties and Applications of Magnetic Materials*, 2002.
10. Beckley, P, *Electrical steels, A handbook for Producers and Users*, European Electrical Steels, 2000.
11. Communication with Dr. Hugh Stanbury, Cogent Power Ltd.
12. Saito, T. "*Opened-type magnetic shielding*," *IEEE International Magnetics Conference*, pp: CR-03, 2003.
13. Jiles, D.; Atherton, D, "*Theory of ferromagnetic hysteresis*," *Journal of Magnetism and Magnetic Materials*, Volume: 61, pp. 48-60, 1986.
14. Moser, J.R., "*Low-frequency Low-impedance Electromagnetic Shielding*," *IEEE Transactions on Electromagnetic Compatibility*, Volume: 33, Issue: 3, pp. 202-209, 1988.

Chapter 6. Results and Discussions

15. Moses, A. J., Williams, P. I., Hoshtanar, O. A., "*Real time dynamic domain observation in bulk materials*," *Journal of Magnetism and Magnetic Materials*, Volume: 304, Issue: 2, pp. 150-154, 2006.

Chapter Seven

Conclusions and Future Work

A new method has been developed to measure the magnetic shielding factor of electrical steel panels at extremely low frequencies. Material properties of electrical steels have been investigated regarding to the shielding performance by the new test method and 2 dimensional finite element modelling. Practical issues, such as how defect in the panel and joint of the shielding panels affect the shielding factor has also been studied.

7.1 Conclusions

The following conclusions can be drawn from this investigation:

1. A new test method has been developed and proved to measure the shielding factors of 500 mm square electrical steel panels from DC to 400 Hz. This test setup provides more appropriate test conditions than the existing standard test for electrical steel panels used to build large-scale magnetically shielded rooms. The measured shielding factors are proposed to be used to grade the electrical steels for magnetic shielding purpose.
2. It can be seen from the measurement that both grain-oriented and non-oriented steel panels have a better AC shielding factor than DC. AC shielding factors are reduced with the increasing frequency between 20 and 400 Hz for grain-oriented steel panels, while improved for non-oriented steel panels due to different magnetization status caused by the magnetic anisotropy.
3. The measured DC shielding factor from selected group of sample,

which has very similar magnetic properties, is increasing with the thickness in an approximately linear relation.

4. Double-layer shields in the form of grain-oriented and non-oriented steel panels show better shield factor at 50 Hz than the sum of individual single layer shielding factor. Although the aluminium panel only has a little measured shielding effect, the shielding factor can be dramatically improved by adding an electrical steel panel next to it, because of the increased effective area of induced eddy current within the aluminium panel by the steel panel.
5. Magnetic anisotropic properties of electrical steels can help improving the magnetic shielding of double-layer shield of by the orthogonal arrangement of the rolling directions for both grain-oriented and non-oriented steels. The measured in-plane magnetization at AC field condition confirms that most flux being ducted along the grain-oriented panel distributed along the rolling directions rather than the transverse direction. Although magnetic permeability along rolling direction is much higher than transverse direction, much higher flux density results in more surface leakage at the rolling direction.
6. The Large demagnetizing effect limits the sample in very low magnetization. A maximum in-plane magnetization of 0.06 Tesla was found with the applied field up to 1000 A/m at 50 Hz. The low magnetization makes the initial permeability of the material a determining factor for the flux ducting.
7. The degradation of the shielding by a drilled hole on the steel panel has been measured and modelled. It is likely that the small defects in the electrical steel panels do not affect the overall shielding performance of

the large-scale magnetically shielded room. The overlap has been demonstrated to be a better way of reducing the flux leakage from the joint of the panels during the construction of the shielding room.

8. The computed DC shielding factor from finite element modelling has a good agreement with the measurement for non-oriented samples. The modelled shielding factors at 50 Hz have been proved to be very sensitive to the input initial permeability as shown in section 6 of the chapter 6. Due to the uncertainty of the low AC field B-H characterisation, a difference as large as 50% has been seen between the computed and measured shielding factors at 50Hz.

7.2. Recommendations for future work

Although the trend of the measurement results from this new method agrees with previous research work[1-4], no quantitative comparison can be made due to the difference of the experimental setup. Independent duplication of this system can be a good exercise to confirm the feasibility and usability of the new method.

Because of the difficulty in material handling, such as hole drilling, coil mounting, and low amplitude measurement, in-plane magnetization has been measured by 100 and 200 mm wide search coil along either rolling or transverse directions. More localised measurement of the flux density within the sample is very difficult due to the damage to the sample by mounting the sensing coil. A likely explanation has been made about the cause of the reduction of shielding factor of grain-oriented steel panels at 20 to 400 Hz. Local eddy current distribution, if can be measured, would be a great assistance in explaining the measured shielding factors.

This new method concentrated on measurements between DC to 400 Hz. It requires a huge instrumental upgrade to make the system capable of measurements up to 10 kHz. The tests within higher frequency range can further investigate the eddy current contribution to the shielding factor. It is expected that the eddy current becomes dominant at higher frequencies. The skin depth is more meaningful at these high frequencies[5].

Very low magnetization of the shielding samples has been confirmed by both experiment and modelling. The accurate measurement of very low magnetization B-H property is desired to support the modelling, also the study of the measured shielding factors.

The time harmonic solver used in finite element modelling cannot take the hysteresis into account. This is believed to be one of the major reasons for the disagreement between the computed and measured AC shielding factor. An attempt to incorporate non-linear hysteresis in computing shielding factor has been made recently[6]. Modelling packages, which are capable of hysteresis modelling, are expected.

References:

1. Okazaki, Y., Fujikura, M., "*Magnetic shielding by grain-oriented silicon steel composite panels*," Studies in Applied electromagnetics and mechanics 10: Nonlinear Electromagnetic systems, pp. 644-647, 1996,
2. Okazaki, Y., Ueno, K., "*Magnetic shielding by soft magnetic materials in alternating magnetic field*," Journal of Magnetism and Magnetic Materials, Volume 112, pp: 192-194, 1992.
3. Okazaki, Y., Takami, S., "*Magnetic shielding in alternating field by grain-oriented silicon steel sheets*," Journal of the Magnetism Society of Japan, Volume: 23, No. 4-2, pp. 1365-1368, 1999
4. Bottauscio, O.; Chiampi, D.; Chiarabaglio, D.; Fiorillo, F.; Rocchino, L.; Zucca, M. "*Role of magnetic materials in power frequency shielding: numerical analysis and experiments*," IEE Proceedings, Generation, Transmission and Distribution, Volume 148, Issue 2, pp: 104-110, 2001.
5. Bottauscio, O. Chiampi, M. Roccato, P. E. Zucca, M. , "*1-100 kHz magnetic shielding efficiency by metallic sheets: modelling and experiment by a laboratory test bed*," IEEE International Magnetism Conference, 2006, pp: 809-809, 2006.
6. Sergeant, P. Zucca, M. Dupre, L. Roccato, P.E., "*Magnetic shielding of a cylindrical shield in nonlinear hysteretic material*," IEEE Transactions on Magnetism, Volume 42, Issue 10, pp. 3189-3191, 2006

List of Publications:

1. Xiaojun Di, Anthony J. Moses, Philip Anderson, "*A method of measuring the performance of electrical steels for extremely low frequency magnetic shielding*" in Soft Magnetic Material Conference 17, Bratislava, 2005.
2. Xiaojun Di, Anthony J. Moses, Philip Anderson, "*Assessment of Low frequency shielding performance of electrical steel sheet*" in The Magnetic Measurement Conference,
3. Anthony J. Moses, Xiaojun Di, Philip Anderson, Philip Beckely, Hugh J. Stanbury, "*Low frequency magnetic shielding - Present and future measurement*" in The 9th International Workshop on 1 & 2 Dimensional Magnetic Measurement and Testing, Czestochowa, Poland, 2006.
4. Anthony J. Moses, Xiaojun Di, Philip Anderson, Philip Beckely, Hugh J. Stanbury, "*Low frequency magnetic shielding - Present and future measurement*", Przegląd Elektrotechniczny, 2007 - 4.
5. Xiaojun Di, Anthony J. Moses, Philip Anderson, "*A novel way of measuring DC magnetic shielding efficiency of grain oriented and non oriented electrical steel*", International Journal of Applied Electromagnetics and Mechanics, Volume: 25, Number: 1-4, 2007.
6. Xiaojun Di, Anthony J. Moses, Philip Anderson, "*Measured and computed effect of holes on low frequency magnetic shielding performance of electrical steel sheet*", IEEE transaction on Magnetics, Volume: 42, Issue: 10, pp: 3527-3529, 2006

